Surface Induced Effects in Hard Sphere Systems

Inaugural–Dissertation
zur
Erlangung des Doktorgrades der
Mathematisch-Naturwissenschaftlichen Fakultät
der Heinrich-Heine-Universität Düsseldorf

vorgelegt von

MARTIN HENI

aus Tübingen

Düsseldorf, 23. April 2001

Gedruckt mit Genehmigung der
Mathematisch-Naturwissenschaftlichen Fakultät
der Heinrich-Heine-Universität Düsseldorf

Referent:	Prof. Dr. H. Löwen
Koreferent:	Priv.-Doz. Dr. R. Blossey

Tag der mündlichen Prüfung: 6. Juni 2001

This thesis is based on the following original papers:

Chapter 4:

M. Heni and H. Löwen,
Interfacial free energy of hard sphere fluids and solids near a hard wall,
Physical Review E **60**, 7057 (1999).

Chapter 5:

M. Heni and H. Löwen,
Surface freezing on patterned substrates,
Physical Review Letters **85**, 3668 (2000).

M. Heni and H. Löwen,
Precrystallization of fluids induced by patterned substrates,
J. Phys. Cond. Mat. **13**, 4675 (2001).

H. Löwen, E. Allahyarov, J. Dzubiella, C. von Ferber, A. Jusufi, C. N. Likos and M. Heni,
Interactions and Phase Transitions of Colloidal Dispersions in Bulk and at Interfaces,
Phil. Trans. Roy. Soc. A **359**, 909 (2001).

Chapter 6:

M. Heni and H. Löwen,
Do liquids exhibit local five-fold symmetry at interfaces?,
(in preparation) (2001).

Zusammenfassung

Heutzutage nimmt die Bedeutung von Oberflächeneffekten bei der Entwicklung neuer Materialien und Produkte zu. Diese Effekte dominieren Systemen so divers wie biologische Zellprozesse, das Aufbringen von Farbe auf Oberflächen, anti-haftbeschichtete Töpfe, anti-reflexbeschichtete Brillen und sogar Skiwachse. In dieser Arbeit untersuchen wir die Auswirkungen einer Oberfläche auf das Benetzungsverhalten von Flüssigkeiten. Ein Schwerpunkt ist hierbei ein ungewöhnliches Benetzungsphänomen, das Benetzen einer Oberfläche durch eine kristalline Schicht bei Temperaturen oberhalb, bzw. Drücken unterhalb, dem Gefrierpunkt.

Anhand eines theoretisch einfach zu behandelnden Systems, dem Harte-Kugel System untersuchen wir systematisch welchen Einfluß sowohl glatte als auch strukturierte Oberflächen in der Nähe des Gefrierpunktes haben. Unser besonderes Augenmerk gilt dabei den Oberflächenspannungen der Flüssigkeit und des Festkörpers an einer Oberfläche, dem Benetzen von glatten und strukturierten Oberflächen durch kristalline Schichten, sowie den strukturellen Korrelationen und Symmetrien, die ein Oberflächenmuster in einer dichten Flüssigkeit hervorruft. Hierzu verwenden wir sowohl *Monte-Carlo* Computersimulationen als auch analytische Theorien.

Wir haben die Oberflächenspannungen der Harten-Kugel Flüssigkeit und des Kristalls für verschiedene Orientierung mit Computersimulationen und Zellentheorie bestimmt. Weiterhin haben wir den Einfluß eines Substratmusters mittels Computersimulationen und einer thermodynamisch-elastischen Theorie untersucht. Wir fanden, daß spezielle Oberflächenmuster, das Benetzen durch eine kristalline Schicht extrem begünstigen. Schon bei sehr niedrigen Drücken von bis zu 29% unterhalb des Gefrierdruckes setzt die vollständige Benetzung ein. Bei nicht so idealen Mustern, wie z.B. ein verzerrtes ideals Muster, kann eine teilweise Benetzung erreicht werden. In diesem Fall dominieren elastische Effekte und die komplette Benetzung durch einen Kristall wird verhindert. Werden die elastischen Energien oder Oberflächenenergien zu groß, erhält man eine inhomogene Flüssigkeit an der Oberfläche. Hier haben wir strukturelle Korrelationen und Symmetrien untersucht und stellen Daten als Vergleich für Experimente bereit.

Da sich besonders kolloidale Suspensionen nahezu identisch wie ein Harte--Kugel System verhalten lassen sich unsere Ergebnisse direkt auf ein Experiment übertragen. Unsere Ergebnisse und Theorien können dazu dienen, maßgeschneiderte Oberflächen zu erzeugen, welche ein genau definiertes Verhalten haben und so zum Beispiel Kolloidkristalle erzeugen können.

Contents

Chapter 1

Introduction

Nowadays, the bulk phenomena of many materials are well analysed and mostly understood. This understanding however, is not yet achieved for surface effects as the presence of a surface can profoundly change the behavior of a system. It induces a much richer scenario for interfacial phase transitions such as wetting [1, 2] or surface reconstruction [3] which are interesting from a fundamental point of view. However, surface and interface effects are very important and their importance is ever increasing with the development of new materials and products. They govern many technical applications, biological systems and even daily life phenomena [4, 5]. Prominent examples are the interaction of cells, the application of paint, the convenient effect of non-stick pots and pans, anti-reflecting glasses or super polished skis.

The understanding and use of surfaces even allows one to design new colloidal materials with a wide range of optical and mechanical properties. Progress in this area can lead to new materials for new lithographic techniques or photonic applications [6, 7, 8]. In particular, the three dimensional periodicity of a colloidal structure could be used to create a band structure effect for photons analogous to the electronic band structure in semiconductors. Although not yet seen in three dimensional materials such a band gap has been reported for visible light in a two dimensional structure [9]. However, fabrication of such materials which could be based on three dimensional colloidal crystals grown on patterned templates could lead to optical gates and switches necessary for optical computers. Yet another application can be imagined by creating bioactive substrates as well as biochemical sensors by using specially tailored colloid surfaces [10]. These structured substrates could be tailored as guiding systems for tiny amounts of chemical

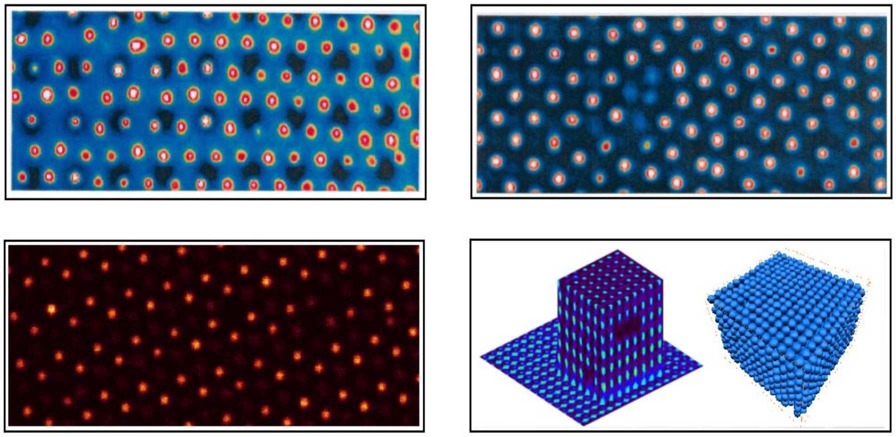

Figure 1.1: Confocal microscopy images of colloidal crystals (friendly permission by A. van Blaaderen [12]). Top left: Colloids form a fcc (111) crystal, top right: colloids form a fcc (100) crystal, bottom left: colloids form a hcp (110) crystal and bottom right: three dimensional reconstruction of a colloidal fcc crystal.

fluids or medical drugs leading to microfactories or chemical chips [11]. However, the manufacturing of such new materials requires a thorough understanding of the underlying fundamental physical principles and any progress in the development of new technologies has to be accompanied by the understanding of the phase behavior and the interaction of the liquids at the surfaces. A primary starting point for this understanding is discussed within this work.

Modern technology already allows one to create solid surfaces with stable geometrical structures. This can be done using techniques such as holographic, X-ray or chemical lithography as well as microcontact printing [13, 14, 15]. These two dimensional templates can then serve as a starting point for a more complex three dimensional structure. One important way to create arbitrary three dimensional colloidal structures is by preparing a substrate with one of the above mentioned techniques and then choosing the experimental conditions so that a three dimensional structure grows on this substrate. Depending on the exact conditions this can be a regular crystal, a quasicrystal or an irregular structure. Such experiments are currently in progress by *van Blaaderen et. al* [12]. In Figure (1.1) we show some experimental results of colloidal crystals viewed by confocal microscopy [12]. Various stable crystals can be grown like the fcc (111), fcc (100) or even a hcp (110) crystal. Layers of these crystals are depicted in Figure (1.1) together with a full three dimensional reconstruction of a colloidal crystal.

Our work will in particular analyse such situations where a system is in contact with a structured wall. By changing parameters such as the topology of the wall, its attraction or the pressure of the bulk system, we are able to show a variety of different behaviors in these systems. A particular interesting type of wetting transition is surface freezing, where a liquid surface spontaneously builds up several crystalline layers at temperatures significantly above bulk freezing. In our work we will investigate the occurrence of surface freezing in more detail. In fact, well-characterized substrates with periodic nano-sized chemical and topographic structures can now be prepared using lithographic procedures or microcontact printing [15, 16], thus allowing our results to be directly verified in experiments where the principle influence of a patterned substrate, used as a template on the nature of wetting transitions, has recently been demonstrated for chemically heterogenous surfaces [17, 18, 19, 20].

In this work we focus on a model system of spherical particles modeled as hard spheres in the neighborhood of a substrate composed also of hard spheres forming a periodic two-dimensional array. This approach has the advantage that the model is kept simple as the thermodynamics and phase diagram of the bulk hard sphere system depend only on the density or equivalently, the packing fraction of the hard-spheres. Understanding the underlying molecular principles of the system is thus possible within this “minimal” framework. In Figure (1.2) we depict the principal setup of our research system, where we present a patterned substrate to a hard-sphere system. One approach is to investigate the hard-sphere fluid in contact with the structured substrate as shown in Figure (1.2a). The substrate can induce interesting structural or symmetry effects in the fluid. Moreover, a special case arises in which only a flat wall is analysed, that is, in which no pattern appears at all. This then produces an even more simple model in which very basic fundamental properties of freezing can be studied. In particular, the calculation of surface free energies is of interest as these key quantities determine the nature of a wetting transition. The interesting case of surface freezing, that is, the wetting of the substrate by crystalline layers is depicted in Figure (1.2b). Here the focus is on the creation and analysis of the crystalline sheet forming at the substrate.

However, our theoretical model is actually applicable for index-matched sterically-stabilized colloidal suspensions on periodic patterned substrates which can be prepared by “gluing” colloidal spheres onto a periodic pattern [12, 21, 22]. Moreover, our model may also serve as a simple microscopic description of molecular systems such as liquid metals on crystalline surfaces [23].

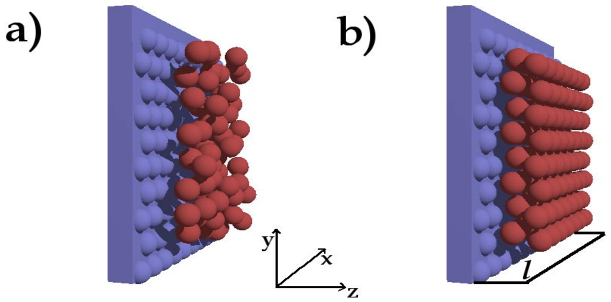

Figure 1.2: Schematic drawing of a hard sphere fluid (red) in contact with a patterned wall (blue). It can either just flow around the structure forming an inhomogeneous fluid (a) or form a crystalline layer of thickness ℓ following the structure imprinted on the surface (b).

Within chapter 2 we review the properties and phase behavior of a hard sphere system and its direct connection to experimental systems of sterically-stabilized colloids. Hard sphere systems are a very peculiar type of physical system which contain many surprising effects like an entropically driven phase transition into a fcc crystal. However, the behavior of a hard sphere system has been shown to be very generic for many real world systems which exhibit a hard core in their interaction potential. Therefore, this model can serve to make quite general predictions and it is ideally suited for a theoretical study of interfacial effects of fluids.

In chapter 3 we shall discuss the relevance of computer simulations in this field. We will describe different simulation approaches and give an extensive overview over suitable order parameters used to detect surface freezing and in particular layerwise surface freezing. At this point we also introduce a novel order parameter which is especially suited for the detection of freezing into a crystal with ambiguous stacking order such as the fcc crystal.

Applying theses tools to the actual interfacial problems leads in chapter 4 to the analysis of interfacial free energies of hard sphere fluids and solids near a flat wall. Most of the physical properties of a solid or liquid in contact with a substrate such as wetting, spreading and heterogeneous nucleation, are governed by the interfacial free energies between the substrate and the material. Therefore a microscopic theory of surface tensions is highly desirable in order to predict the wettability of a given substrate for different materials. However, this quantity depends on the microscopic interactions between the particles both of the substrate and the material and therefore is a highly complex problem. By mapping the key features of this problem onto a hard sphere model we are able to make very general predictions on the interfacial free energies. Using computer simulations and an analytical cell theory we are able to obtain the fluid-wall and solid-wall interfacial free energy over the whole range of possible densities of the hard-sphere system. Here in particular, our approach and the results for the solid-wall interfacial energies for various crystal orientations are novel. These results then allow one to make general predictions about whether a hard-sphere fluid can precrystallize at a surface or not.

The actual effects of hard sphere fluids near flat and structured walls is investigated within chapter 5. A surface pattern has a strong effect on the wetting properties of a system and its understanding is important from a fundamental point of view as well as for guiding experiments or developing new applications. Within the hard-sphere system we find a peculiar type of wetting transition where a liquid surface builds up spontaneously several crystalline layers at temperatures well above bulk freezing. Such a precrystallization has been seen in experiments for molecules such as alkanes [24, 25, 26, 27, 28] and alcohols [29, 30]. However, both of these systems have shapes and interaction potentials far more complex and more difficult to analyse than spherical particles with a radial symmetric interaction potential. However, precrystallization effects have not yet been thoroughly studied for spherical particles, which are a much more generic case and allow a fundamental understanding of the problem. Using computer simulations and introducing a new theory suitable for the calculation of the surface phase transitions of precrystallization we investigate the influence of the surface pattern on the behavior of the fluid in contact with such a pattern. Depending on the type of the surface pattern, the behavior can be tuned from complete wetting by crystal over partial wetting by crystal to no wetting at all. Moreover, we analyse the effect of elastic strains onto the prefreezing transition by offering substrate patterns which do not exactly match the ideal bulk crystal. This lattice mismatch is particularly important for experiments where the parameters of the substrate pattern can not be chosen completely freely and a natural lattice mismatch is introduced into the system. Surprisingly, we find that this mismatch can even shift the onset of prefreezing away from coexistence to lower pressures or respectively higher temperatures. However, elastic strains always prevent complete freezing.

These results can be used to make quite general predictions on the behavior of fluids in contact with structured substrates which consequently allow especially tailored surfaces to be made. It may therefore serve as a guideline in the creation of unstable phases by a surface pattern which can be used to prepare "exotic"

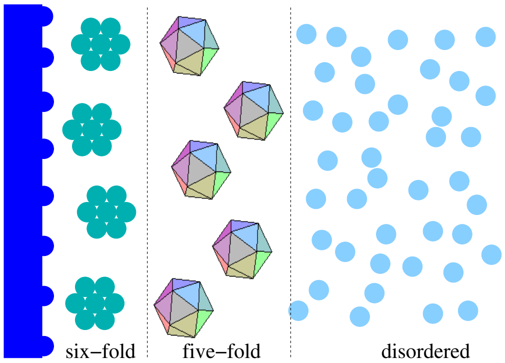

Figure 1.3: Schematic drawing of a super-cooled hard sphere fluid in contact with an strongly attractive surface. Close to the surface the structure of the surface is imprinted into the fluid. Further away from the surface the high density fluid exhibits five-fold symmetry which decays when approaching bulk fluid densities even further away from the surface.

structures such as quasicrystalline sheets on a suitably patterned template.

Finally, we investigate structural correlations in the fluid controlled by an underlying topographically patterned substrate and present them in chapter 6. In particular, we focus upon the occurrence of five-fold symmetries in liquids at interfaces. By applying an attractive potential perpendicular to the wall we were able to raise the local density of the fluid well above the bulk freezing density. This is possible as a topographically unfavorable structured wall pattern prevents the fluid from freezing. This particular setup allows one to study the cross-over of the symmetry defined by the surface pattern and induced into the fluid close to the interface to a five-fold symmetry in a high density super-cooled liquid farther away from the interface. This cross-over is depicted in Figure (1.3).

In chapter 7 we finally conclude with a summary and discussion.

Chapter 2

Hard sphere systems

At first glance a hard particle system is a very simple system. Let us consider a system of N spherical particles in a volume V at a fixed temperature T, interacting with each other only through an infinite repulsion on contact. One can best imagine this as a huge box filled with N billard balls. More formally, we can define the system using a radial symmetric interaction potential U acting between two particles i and j as

$$U(\vec{r}_i, \vec{r}_j) \equiv U(|\vec{r}_i - \vec{r}_j|) = \begin{cases} 0 & \text{if } |\vec{r}_i - \vec{r}_j| \geq \sigma \\ \infty & \text{otherwise} \end{cases} , \tag{2.1}$$

where σ is the diameter of a sphere, the center-of-mass positions of the spheres are denoted by $\vec{r}_i = (x_i, y_i, z_i)$ with $(i = 1, \ldots, N)$. This interaction scheme is depicted in Figure (2.1). The finite number density of the spheres is $\rho = N/V$ which can conveniently be expressed in terms of the dimensionless packing fraction $\eta = \pi\rho\sigma^3/6$. Using such an interaction energy yields a system without internal energy, which follows directly from the interaction potential Eqn. (2.1) as particles do not experience any potential for any valid configuration, that is a configuration where no particles overlap. All overlapping configurations are forbidden as the energy is infinite. As there is no relevant energy defined, the system is purely governed by entropy and the (irrelevant) temperature sets only the energy scale and does not affect phase transitions or structural quantities.

Besides the fact that it is very interesting to study the pure entropic effect of a system, it has been found that many effects of physical systems are dominated by entropy [31]. This includes structural properties as well as phase transitions. One particular interesting example is the freezing transition of a hard sphere system.

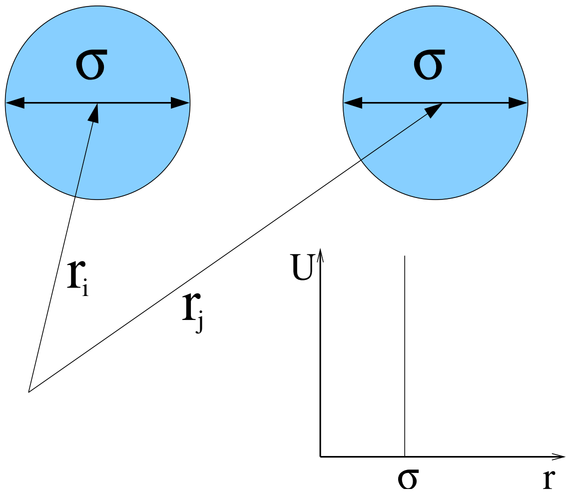

Figure 2.1: Two hard spheres with diameter σ at positions $\vec{r}_i$ and $\vec{r}_j$ interact with the interaction potential $U(r)$ from Eqn. (2.1) with $r = |\vec{r}_i - \vec{r}_j|$. The interaction potential is infinite for $r < \sigma$ and zero for $r \geq \sigma$.

It has been long debated whether or not it is possible for a system to exhibit entropy driven freezing. Intuitively one could argue that a crystal as a more ordered system has a lower entropy as a fluid at the same density. According to the second law of thermodynamics which requires a maximization of the entropy it would follow that a hard sphere crystal could never be stable. However, around 1957, *Alder*, *Wainwright et al.* [32] computationally discovered the hard sphere fluid-solid first order phase transition, where the hard sphere system freezes above a certain density into a face-centered-cubic (fcc) crystal. This, at first surprising and counter-intuitive result is nowadays well acknowledged [33, 34] and can be explained by considering the configurational entropy of a crystal. In a crystal, although particles are well ordered on a lattice, the particles have a maximum amount of free volume to move around their lattice positions. On the other hand, in a fluid of the same density many particles are so crammed together that they are immobile or have a very limited movement. As each of these configurations contributes to the entropy and a crystal has much more accessible volume, that is, more available configurations than the fluid at high density, this results in a higher entropy for the crystal. From this argument we can conclude that a crystal can form a stable state for the entropical governed hard sphere system. However, this argument does not allow to deduce at which density this phase transition occurs. In particular it could theoretically only occur at close packing. Computer simulations [32, 35] however have shown that a hard sphere crystal is stable at

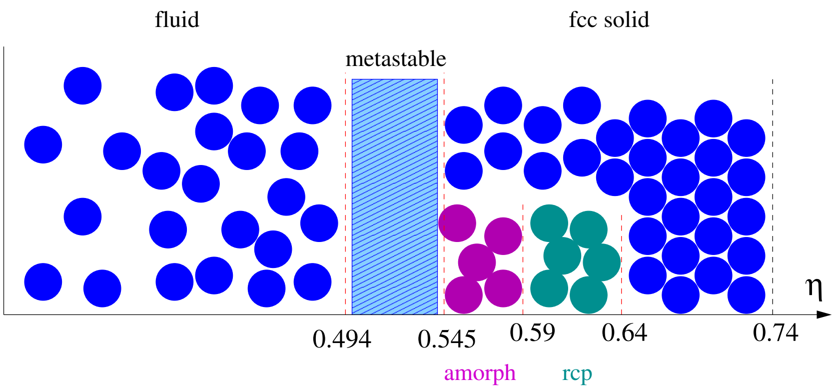

Figure 2.2: Phase diagram of a hard sphere system. The fluid state is thermodynamical stable at packing fractions $\eta < 0.494$ and the solid state is stable at packing fractions $\eta > 0.545$.

packing fractions $\eta = 0.545$ up to the maximum packing fraction for a hard sphere system of $\eta = \pi\sqrt{2}/6 = 0.741\ldots$ [36]. Crystals at this maximum packing fraction are called closed packed crystals and 1998 *T. C. Hales* [37] could prove the general *Kepler Conjecture* which states that no packing, that is also no irregular packing, of spheres in three dimensions can have a packing fraction greater than $\eta = \pi\sqrt{2}/6 = 0.741\ldots$. This packing fraction is achieved for a face-centered-cubic (fcc) or its equivalent modifications hexagonal-closed-packed (hcp) or random-closed-stacking (rcs) [38]. Nowadays, space shuttle zero-gravity experiments of colloids with nearly hard-sphere interaction potential, indeed revealed a stable solid phase of a hard-sphere crystal [39].

The hard sphere fluid on the other hand is the stable thermodynamical state at packing fractions below $\eta = 0.494$. In between these packing fractions there is a large coexistence region. The hard sphere system can also form an interesting metastable glass like state at packing fractions above $\eta = 0.545$. Up to packing fractions of $\eta = 0.59$ this state can be reached by super-cooling the fluid and numerical analysis found that it is possible to pack hard spheres in an unordered, randomly closed packed (rcp) state at packing fractions up to $\eta = 0.64$ [40, 41, 42, 43, 44] These results are summarized in a phase diagram for hard spheres in Figure (2.2).

However, hard spheres are not only a theoretical model of high abstraction. It has been found that real systems, like colloidal particles, can be prepared in very good approximation to a hard-sphere like interaction. This hard sphere interaction is actually realized in suspensions of sterically-stabilized colloids [45].

In such systems with mesoscopic particles one has the further advantage that real-space methods allow the possibility to explore the structure of the bulk and of the interfaces directly [12, 46, 47].

Colloids are extremely small particles which can form solid or liquid phases. The word *colloid* arises from the Greek words $\kappa\acute{o}\lambda\lambda\alpha$ (glue) and $\epsilon\acute{\iota}\delta o\varsigma$ (kind). Its original meaning, “sticky stuff” was introduced by *Thomas Graham* around 1831 to label substances which appeared similar to fluids but had anomalously small diffusion rates. Only much later it could be shown that colloids are not homogeneous substances but actually small particles dissolved into a solution. These colloidal particles are about $10nm$ to $1\mu m$ in diameter and larger colloids can be even viewed by light microscopy. To give some examples:

- Smoke or dust are colloidal suspensions of a solid (carbon, silica or sand) in the air.
- Fog or mist is an aerosol, a colloidal suspension of liquid (water) molecules in the air.
- Milk is an emulsion, a colloidal suspension of liquid (fats and oils) in another liquid.
- Gold-ruby glass is a colloidal suspension of one solid (gold) in another solid (glass).
- Blood is a colloidal suspension of a solid (blood cells) in a liquid.

The interaction potential of colloids in a solution can be adjusted by adding salt to the solution so that the screening effect of the ions in solution just leaves a hard sphere like potential (index matched colloids). Furthermore, colloids can be designed which are coated with polymer brushes on their surface. Entropic repulsion of these polymer brushes creates a hard sphere like repulsion (sterically stabilized colloids).

Moreover, from a more theoretical point of view, many of the atomic interactions can be approximately mapped onto an effective hard-sphere systems. However, even atomic systems, such as liquid metals often behave in leading order as hard spheres. The study of the hard-sphere interaction is therefore often useful as a reference case for these systems [48, 49]. The validity of this generic behavior results from interactions which are governed by the repulsion of the hard core of the potential which is caused by the *Born-Fermi* repulsion of the electron shells of the atoms or molecules. An attractive part of the potential does not affect many structural quantities and even thermodynamic properties. Only a liquid-gas phase transition does not exist within the hard sphere system as in this case an attractive part of the potential is needed to create such a phase transition.

Chapter 3

Computer simulations

Computer simulations have proven to be a very valuable tool for analysing problems in modern science and technology. Wherever an exact solution is impossible or tedious to obtain computer simulations can serve as an alternative to gain insight into the problem or obtain numerical or approximate solutions. This is particularly true for thermodynamical systems which have many degrees of freedom (in the order of the particle number) as is investigated in the following chapters. For some systems under consideration some analytical approximations exists but a major part of the analysis, especially when leaving the bulk regime and analysing surface effects, cannot be done analytically [50, 51, 52, 53, 54, 55]. Typically particle numbers for real systems are in the range of the *Avogadro* number of 10^{23} particles. Although these high particle numbers are even outside the scope of computer simulations, we are still able to use model systems in the order of 10^4 particles. Already this is far too complex to analyse with conventional methods. Theoretical calculations, which we also perform in our work require a massive simplification of the system. Computer simulations on the other hand give very precise access to most quantities of the systems and can be used to verify the theories as well as predict new effects or serve as benchmark data for theories.

3.1 History

The idea of computer simulations is quite old. Already in the 18th century people were beginning to think and construct calculation machines and algorithms for them. Although these early ideas resemble quite remarkably the computers of today only with the invention of modern electronics and semiconductor devices have computer simulations become feasible, affordable and a standard tool in physics and other sciences.

Going back into the history of computer simulations we first encounter *Charles Babbage*, born in 1792, who is the originator of the idea of nowadays computers. *Babbage* faced continuous difficulties in calculating logarithms and around 1812 these difficulties made him aware of the need for an automated calculation device. In the following years until 1822 he constructed a "difference" engine and by 1834 he completed the first drawings of an analytical engine, the ancestor of the modern electronic computer. Due to the lack of mechanical engineering technology *Babbage* was never able to built an operational, mechanical computer. Yet his design concepts have been shown to be correct and recently such a computer has been built following *Babbage's* own design criteria.

Around the same time as *Babbage* was designing his mechanical computer, the first programming language was derived by *Augusta Ada King Countess of Lovelace*, the daughter of the famous poet *Lord Byron*. She heard about *Babbage's* analytic engine around 1833, became interested in the subject and during the following years suggested methods on how to program such a machine. In doing so she invented the first programming language. And today in honor of her memory a programming language (*Ada*) is named after her.

At the beginning of the 20th century *Konrad Zuse* began to develop the first functional modern computer. After failures with a mechanical computer he constructed the first electronic computer in 1941. The first computers were mainly used for mathematical calculations and military applications. However, a big step forward was achieved by the invention of the *Monte-Carlo* method around 1948 by *Nicholas Metropolis* who was born in 1915 and mainly developed and implemented the *Maniac* computer system at Los Alamos Scientific Laboratory and by *Stanislaw Marcin Ulam* who was born in 1909 and who mainly worked on the hydrogen bomb at Los Alamos. They both developed the *Monte-Carlo* method as a method to solve mathematical problems using a statistical sampling method with random numbers around 1948. With this simulation technique it began to become possible to computationally tackle problems with extremely many degrees of freedom.

3.2 Monte-Carlo simulations

Monte-Carlo simulations are widely used in physics, e.g. in quantum mechanics, thermodynamics or meteorology as well as in other areas like economics, finance and risk analysis. They are a method to approximately solve mathematical equations, usually high dimensional integrals which cannot be solved by other means or without unreasonable effort. The name *Monte-Carlo* (MC) stems from the fact that the algorithm is not deterministic but relies upon random numbers to calculate the result. Despite the randomness in the calculation the method applies to problems with non probabilistic content as well as to those with inherent probabilistic structure. Compared to other numerical methods it is also quite efficient.

In our work we are confronted with the calculation of averages of thermodynamical quantities for fluid and solid systems [56, 57]. These averages are defined as integrals spanned by the whole configuration space of all particles, that is $6N$ coordinates for N particles. For a real system N is of the order of 10^{23} and even for computer simulated systems N is still of the order of 10^4. In hardly any case these integrals can be solved analytically and also standard numerical treatment fails at these high dimensional integrals. Moreover, we will consider problems at interfaces [58] which provide an additional challenge. However, *Monte-Carlo* simulations provide an efficient way of approximately calculating these quantities [59, 60, 61].

3.2.1 The definition of the Monte-Carlo method

All thermodynamical quantities can be derived from the partition function

$$Q = \frac{1}{N! h^{3N}} \int d\vec{p}^1 d\vec{r}^1 \cdots \int d\vec{p}^N d\vec{r}^N e^{-\beta H(\{\vec{r}_\nu, \vec{p}_\nu\})}, \tag{3.1}$$

where N is the particle number, $d\vec{r}^N$ and $d\vec{p}^N$ indicate the integration over coordinates $\{\vec{r}_\nu\} = (\vec{r}_1, \ldots, \vec{r}_N)$ and momenta $\{\vec{p}_\nu\} = (\vec{p}_1, \ldots, \vec{p}_N)$ of all particles. $H = U + E_k$ is the *Hamilton* function of the system with potential energy U and kinetic energy E_k, $\beta = 1/(k_B T)$ with T the temperature of the system and k_B the *Boltzmann* constant.

Thermodynamical quantities can be defined as averages of the distribution function

$$\rho(\{\vec{r}_\nu, \vec{p}_\nu\}) = \frac{e^{-\beta H(\{\vec{r}_\nu, \vec{p}_\nu\})}}{Q} \tag{3.2}$$

namely

$$\langle a \rangle = \int d\vec{p}^1 d\vec{r}^1 \cdots \int d\vec{p}^N d\vec{r}^N a(\{\vec{r}_\nu, \vec{p}_\nu\}) \rho(\{\vec{r}_\nu, \vec{p}_\nu\}) \tag{3.3}$$

where $\langle a \rangle$ is any thermodynamical average. We note that with this definition of the thermodynamical average we measure thermodynamical ensemble averages. However, according to *Boltzmann's* ergodic hypothesis any system which behaves ergodic will have the same ensemble and time averages. This assumption is justified if the physical trajectory of the system will sooner or later cover all conceivable micro-states of the system, that is access the whole phase space.

Solving thermodynamical problems leads then to the necessity of evaluating the integral in Eqn. (3.3). In all but the most trivial systems this cannot be done analytically. And even numerically it is quite tricky as it is clearly not feasible to scan the whole configuration space using normal integration methods.

However, we can make a very good approximation by using *Monte-Carlo* simulations [59, 60] which does not evaluate the whole configuration space but only a small portion of it. This part of the configuration space is sampled by moving the particles of the system around to create new configurations. As the reduction of the configuration space does not represent the true physical situation anymore it is not necessary to move particles following true physical trajectories. A representative subspace of the configuration space is scanned instead by randomly moving the system around. However, although in *Monte-Carlo* simulations the particles are moved at random it is still important to follow physical rules so that the configuration space is sampled properly and represents the original system. Only this approach guarantees a good representation of the real thermodynamical system.

There are many approaches on how to sample the configuration space but an often used and well established algorithm is the Metropolis algorithm [62, 63]. It guarantees ergodic behavior of the system and fulfills detailed balance between moves, that is the transition probability $\pi(\mathrm{I} \rightarrow \mathrm{II})$ going from system state I to system state II fulfills

$$\mathcal{N}(\mathrm{I})\pi(\mathrm{I} \rightarrow \mathrm{II}) = \mathcal{N}(\mathrm{II})\pi(\mathrm{II} \rightarrow \mathrm{I}) \tag{3.4}$$

where $\mathcal{N}(x)$ is the probability density

$$\mathcal{N}(x) = \frac{e^{-\beta U(\{\vec{r}_\nu\})}}{\int d\vec{r}^1 \cdots \int d\vec{r}^N e^{-\beta U(\{\vec{r}_\nu\})}} \tag{3.5}$$

to find the system in state x represented by the coordinates of the particles $\{\vec{r}_\nu\}$.

According to the Metropolis algorithm [62, 63] the transition probabilities are given as

$$\pi(\mathrm{I} \to \mathrm{II}) = \begin{cases} M(\mathrm{I} \to \mathrm{II}) & \text{, if } \mathcal{N}(\mathrm{II}) < \mathcal{N}(\mathrm{I}) \\ M(\mathrm{I} \to \mathrm{II})\,(\mathcal{N}(\mathrm{II})/\mathcal{N}(\mathrm{I})) & \text{, otherwise} \end{cases} \tag{3.6}$$

and

$$\pi(\mathrm{I} \to \mathrm{I}) = 1 - \sum_{\mathrm{I} \neq \mathrm{II}} \pi(\mathrm{I} \to \mathrm{II}) \tag{3.7}$$

with M being an *arbitrary* symmetric matrix left to our choice while the acceptance rate going from state I to state II is

$$\mathrm{acc}(\mathrm{I} \to \mathrm{II}) = \begin{cases} \mathcal{N}(\mathrm{I})/\mathcal{N}(\mathrm{II}) & \text{, if } \mathcal{N}(\mathrm{II}) < \mathcal{N}(\mathrm{I}) \\ 1 & \text{, otherwise} \end{cases} \tag{3.8}$$

In our work we analyse systems which consist of an ensemble of spherical particles with a radial symmetric pair interaction potential in the bulk and at the surface. A general Metropolis algorithm applied to these type of simulations, with N particles leads to the following programming scheme:

1. Choose an arbitrary particle $i \in 1, \ldots, N$
2. Calculate the energy E_{I} of the current configuration I
3. Create a new configuration II (see the section 3.2.2)
4. Calculate the energy of the new configuration E_{II}
5. Accept the move with the probability acc(I → II)
6. Calculate the average of any desired quantity $\langle a \rangle$ for all configurations, that is accepted and rejected
7. For performance reasons, all changes in the *Monte-Carlo* system variables, e.g. the displacement of the particles, should be modified so that around 40% of the moves are accepted

Using this algorithm we are able to calculate all thermodynamical properties in the form of Eqn. (3.3).

However, using standard *Monte-Carlo* algorithms it is in principle not possible to calculate free energies or the partition sum itself. This is due to the fact that we are only sampling a subspace of the full configuration space and therefore cannot make any predictions about the full configuration space. We will later on explain a method on how to overcome this limitation.

3.2.2 Monte-Carlo simulations in various ensembles

Although in the thermodynamical limit, that is in infinite systems all thermodynamical calculations converge towards the same value this does not necessarily apply to small systems. Also, it is not guaranteed that equilibrium values are approached at the same speed. Therefore, it is important to choose an thermodynamic ensemble which suits the problem under consideration best. To judge the effects of ensemble differences it is also helpful to check results in various ensemble to estimate ensembles dependent artifacts.

Although computer *Monte-Carlo* simulations are not restricted to the shape of the simulation box we choose a rectangular simulation box for all further studies. The reason for doing so is twofold. First, all crystals under consideration have rectangular shapes so that the choice of a rectangular simulation box is the most appropriate and natural one. Second, for fluids the shape of the simulation box is not of real consequence and the rectangular simulation box is a convenient choice.

In the following sections we describe different thermodynamical ensembles useful to our study.

The canonical ensemble - NVT

The canonical ensemble is the most intuitive one. The independent variables which are held constant during a simulation run are the particle number N, the volume of the simulation box $V = L^3$ and the temperature T. The partition sum is

$$Q = \frac{1}{N!\Lambda^{3N}} \int_0^L d\vec{r}^1 \cdots \int_0^L d\vec{r}^N e^{-\beta U(\{\vec{r}_\nu\})}, \tag{3.9}$$

with the irrelevant *de Broglie* wavelength $\Lambda = \sqrt{h^2/(2\pi m k_B T)}$, where h denotes the *Planck* constant and m the mass of a particle. Eqn. (3.9) yields the probability of finding a configuration

$$\mathcal{N}(\{\vec{r}_\nu\}) \propto e^{-\beta U(\{\vec{r}_\nu\})} \tag{3.10}$$

and an acceptance rate of

$$\mathrm{acc}(\mathrm{I} \to \mathrm{II}) = \min\left(1, e^{-\beta U(\mathrm{I}) - U(\mathrm{II})}\right) . \tag{3.11}$$

This leads to the following rule for the creation of a new configuration in section 3.2, algorithm step number 3:

a. Choose a random particle i ($i = 1..N$)

b. Move the particle by an arbitrary displacement vector $\Delta\vec{r}$

The canonical ensemble is easy to implement and very fast as there are just particle movements. As the box shape is not changing it is well suited for crystals forming at the walls. Its main disadvantage for crystallization studies is that inhomogeneous density distributions like adsorbtion at the surface will deplete the bulk and therefore lower the overall bulk density. Despite having the density as input parameter into a NVT simulation one nevertheless has to measure the bulk density which results in statistical errors in this variable. Furthermore, a NVT ensemble does not give very sharp phase transitions when investigating crystallization.

The isobaric-isothermal ensemble - NPT

The isobaric-isothermal ensemble [64] is defined with a constant particle number N, a constant external pressure P applied to the system and a constant temperature T. The simulation box is of volume $V = L^3$. The partition sum is

$$Q = \frac{1}{N!\Lambda^{3N}} \int_0^L d\vec{r}^1 \cdots \int_0^L d\vec{r}^N e^{-\beta U(\{\vec{r}_\nu\})}, \tag{3.12}$$

which can be rewritten using the scaled coordinates $\vec{r_i}' = \vec{r_i}/L$ as [59, 60] have shown. This is equivalent to writing the partition sum as

$$Q = \frac{\beta P}{N!\Lambda^{3N}} \int d(\ln V) V^{N+1} e^{-\beta PV} \int d\vec{r}' e^{-\beta U(\vec{r}'_\nu;L)} . \tag{3.13}$$

Eqn. (3.9) yields the probability of finding a configuration

$$\mathcal{N}(\{\vec{r}'_\nu\}) \propto V^{N+1} e^{-\beta PV} e^{-\beta U(\{\vec{r}'_\nu\};L)} \tag{3.14}$$

and an acceptance rate of

$$\mathrm{acc}(\mathrm{I} \to \mathrm{II}) = \min\left(1, e^{-\beta U(\mathrm{II}) - U(\mathrm{I})}\right) + P(V' - V) - \frac{(N+1)}{\beta} \ln\left(\frac{V'}{V}\right) . \tag{3.15}$$

This yields following rule for the creation of a new configuration in section 3.2, algorithm step number 3:

a. Choose a random particle i ($i = 1..N$)

b. Move the particle by an arbitrary displacement vector $\Delta\vec{r}$

c. Every N particle move changes the volume of the simulation box from L^3 to L'^3 by scaling the particle coordinates $\vec{r}' = \vec{r}L/L'$ and accept the change with the probability acc(I → II)

The isobaric-isothermal ensemble is in some respects more suitable for phase transition studies. A phase transition is easier driven when the system can change its density with the pressure given. The bulk density is automatically adjusted but remains as a measurement variable. Its main disadvantage is that the system volume can change in all spatial directions. This creates box shapes which do not fit the crystals under investigation well. Introduced strains will make crystal formation more difficult. Although the system will usually find the thermodynamical equilibrium, it is very inefficient and takes a long time to simulate. We do therefore not use this ensemble but a slightly modified version which is described in the next section.

The quasi isobaric-isothermal ensemble - NP_zT

More suitable for the simulation of wetting of a surface by a crystal is the quasi isobaric-isothermal ensemble. It corresponds to the isobaric-isothermal ensemble in all but one property. The simulation box is fixed in two directions x,y and only variable in size in the remaining z-direction. Its volume will be $V = L^2 L_z$ with L_z the length in z-direction. Therefore only a component of the pressure P_z in z-direction is applied to the system and the scaling of the system affects only its z coordinate. The x and y coordinates are treated as a constant volume simulation. Therefore all equations and algorithms of the NPT algorithm apply as well.

This leads to the following rule for the creation of a new configuration in section 3.2, algorithm step number 3:

a. Choose a random particle i ($i = 1..N$)

b. Move the particle by an arbitrary displacement vector $\Delta\vec{r}$

c. Every N particle move changes the length of the simulation box from L_z to L'_z by scaling the particle coordinates $z' = zL_z/L'_z$ and accept the change with the probability acc(I → II)

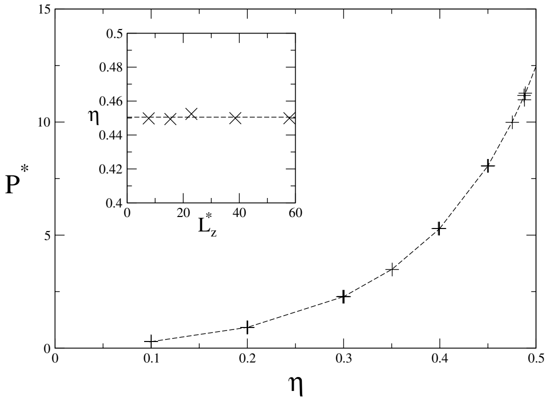

Figure 3.1: Pressure $P^* = P\sigma^3/k_BT$ versus packing fraction η of a hard sphere fluid in NP_zT simulation. The inset shows the finite size dependency of η versus the box length $L_z^* = L_z/\sigma$ for a fixed pressure $P^* = 8.1$. The dashed lines are the respective values as obtained by the *Carnahan-Starling* equation of state [65].

This ensemble inherits its advantages from the isobaric-isothermal ensemble but does not have the difficulties to fit a crystal into the simulation box as we can choose the box size a priory to fit the expected crystal. It is superior in finding phase transitions to the canonical ensemble but still has the disadvantage of longer equilibration especially with a crystal forming at the surface and it involves higher computation cost for the extra scaling moves.

In Figure (3.1) we show the equation of state for a hard sphere fluid as obtained by the NP_zT simulation as compared to the *Carnahan-Starling* equation of state [65]. We see that they agree well.

For comparison of the results we use both, the NP_zT and the NVT ensemble and generally find good agreement between both of them.

The grand canonical ensemble - μVT

Yet another ensemble used in *Monte-Carlo* studies is the grand canonical ensemble. Here the chemical potential μ, the system volume V and the temperature T are held constant. This ensemble has a key difference to the ones discussed above as the total number of particles in the system is not fixed. Thus, it is very well suited

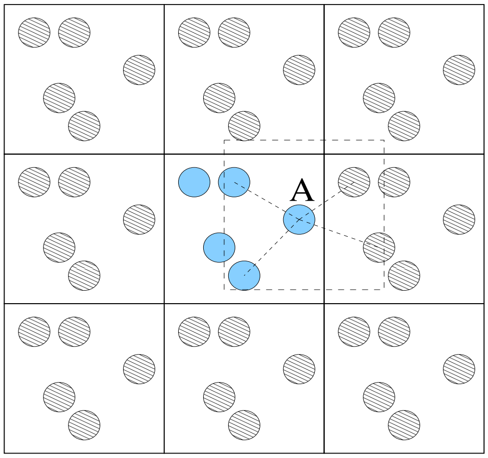

Figure 3.2: The simulation box is shown in the middle. Around this central box some virtual boxes containing mirror images of the central box are drawn. For particle A the interaction partners are indicated by dashed lines.

for investigating phase transitions or adsorption problems as the system will insert and remove particles as required to form or melt crystals which means that more or less particles are needed in the system.

Unfortunately, for our studies it is not feasible to use grand canonical *Monte-Carlo* simulations as we are investigating very high densities of a hard sphere system. With hard particles new particles can only be inserted when there is enough empty space to fully fit one hard particle in. For high densities this becomes extremely unlikely and therefore the algorithm becomes highly inefficient and will basically not equilibrate. Therefore, although this ensemble is suitable for this type of studies it cannot be applied to our work.

3.2.3 Boundary conditions

In our simulations we can only simulate a small number of particles compared to a real world system. This has the consequence that a high percentage of the particles in the system are at the surface as the surface per volume ratio scales as $N^{-1/3}$ and is therefore much larger for small systems. This means that we are either dealing with a system which is governed mostly by surface effects or we increase the number of particles into the simulation which strongly increases the simulation time.

However, there is a trick to eliminate most surface effects in simulations. If the system under consideration is a bulk system or has bulk behavior in some of its spacial directions we can use periodic boundary conditions in these directions. Using periodic boundary conditions, the simulation box is replicated throughout space to form an infinite lattice of mirrors of itself. A two-dimensional version of such a periodic system is depicted in Figure (3.2). All particles are mirrored from the central simulation box into virtual boxes in all directions. When a particle in the simulation moves in the central box, its periodic image in every one of the other boxes moves exactly the same way. If it leaves the central box, one of its images will enter through the opposite surface. There are no walls at the boundary of the central box, and therefore the system has no surface. In Figure (3.2) a particle with its neighbors is shown. It interacts with the particles inside the dashed box, which are partly the mirror images of the next boxes.

However, these periodic boundary conditions can be applied only for bulk systems. As we are interested in surface effects we loose part of the advantage of the periodic boundary conditions as we have to apply a wall in one spacial coordinate (z). However, we can still use the periodic boundary conditions in the two other spacial coordinates (x,y). In this way we obtain an infinite system in the $x-y$ directions but a finite system in z-direction. However, for technical reasons it is not possible to just introduce one wall into a computer simulation[1]. Introduction of one wall in a computer simulation will always generate a mirrored wall on the other end of the simulation box. The influence of these two walls onto each other has to be considered in the simulation as it can lead to capillary effects and other spurious influences [67].

3.3 Finite-size effects

When studying any macroscopic system with a very large number of degrees of freedom on the computer, we inevitably make an approximation and simulate a smaller model system. This introduces systematic errors so called finite size effects. These finite size effects need to be understood and we need to be able to estimate their importance so that we can either extrapolate to the correct value of the infinite system or can give an estimation on the finite size error introduced

---

[1] There exists simulation methods which try to simulate a system with just one wall by introducing a sampling method which biases particles close to the second wall in a way to simulate bulk behavior [66]. However, this method introduces other difficulties connected to the choice of this artificial bias.

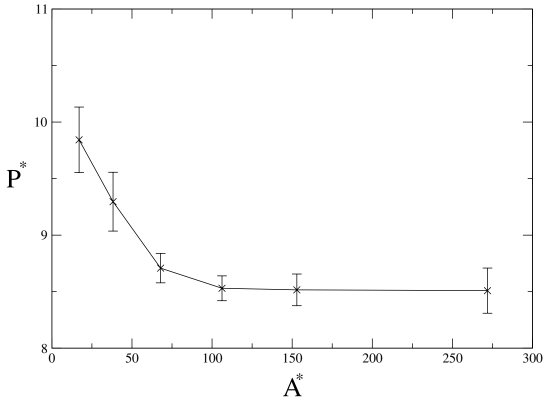

Figure 3.3: The phase transition pressure P^* versus surface area. The pressure saturates at surface areas about $A^* \approx 100$ showing that this value is beyond finite size effects.

[68, 69, 70].

Usually we do this by performing simulations on a set of equal systems where only the number of simulated particles change. Plotting the measured quantities against the system size shows the finite size dependency and allows to obtain the true value by extrapolation to an infinite system size.

For an example we show in Figure (3.3) a measured quantity versus the system size. In the example the scaled phase transition pressure $P^* = P\sigma^3/k_BT$ is plotted versus the size of the system, in this example its scaled surface area $A^* = A/\sigma^2$. We clearly see for small values of the area a strong dependency on the area whilst for larger systems the curve converges against an asymptotic value.

In all our studies we did this finite size analysis and we were able to choose systems of a size which introduced finite size errors smaller than the normal statistical fluctuations.

3.4 Thermodynamical integration

In section 3.2 we have seen that the *Monte-Carlo* method gives a very good approximation of thermodynamical quantities which are derivations of the free energy F or other equivalent thermodynamical potentials. However, it is not possible to obtain the free energies or the partition sum directly. However, it is possible to directly measure derivatives of the free energy

$$\tilde{\lambda} = \left(\frac{\partial F}{\partial \lambda} \right)_{NT} \tag{3.16}$$

like e.g. $P = -\left(\frac{\partial F}{\partial V}\right)_{NT}$. These quantities can be used to calculate the free energy by integrating its derivatives

$$F(\lambda) = F(\lambda_0) + \int_{\lambda_0}^{\lambda} \left(\frac{\partial F}{\partial \lambda'} \right) d\lambda' \tag{3.17}$$

for any suitable derivative $\left(\frac{\partial F}{\partial \lambda}\right)$ from an arbitrary starting point λ_0. The choice of the derivative is arbitrary and can be chosen to suit the problem best.

In doing so we obtain the free energy difference $F(\lambda) - F(\lambda_0)$. However to calculate the full free energy the free energy $F(\lambda_0)$ has to be known independently of the simulation. Usually one chooses a known reference system such as the ideal gas or the *Einstein* crystal. These systems then define the free energy for λ_0 and increasing λ leads to the free energy $F(\lambda)$. Of course, we have to keep in mind that every single integration step requires a full *Monte-Carlo* simulation of the system at the thermodynamical state corresponding to λ'.

Note however, that it is important not to cross any phase transition points during the integration as the derivatives of the free energy might behave there non analytical, rendering the integration scheme worthless. So either the starting point of the integration has to be chosen close enough to the system under investigation or an integration path which evades phase transitions has to be selected.

3.5 Order parameters

In the computer simulations we monitor various thermodynamical quantities like the pressure P or the density ρ. These quantities are usually well understood and also measured in real experiments. Yet they are often not suitable or precise enough to detect phase transitions, in particular surface phase transitions. To get a quantitative measure for these phase transitions an order parameter [71, 72] is introduced which changes its value ideally from 0 in one phase to 1 in the other phase. It is not always easy to find such a good order parameter and a large part of the study of a new problem is often to find a suitable order parameter. As a crystal is characterized by two distinct types of order which do not exist in an

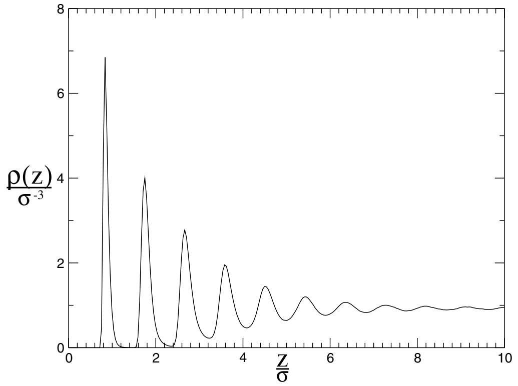

Figure 3.4: Density profile of the hard sphere fluid at a pressure of $P^* = 10.87$ near to a structured wall with a triangular pattern imprinted.

isotropic fluid there are two straightforward approaches to an order parameter. First, this is the translational order, that is shifting the system by a given amount will reproduce an identically system. Second, this is orientational order, that is, rotating the system about a given angle will reproduce the system identically. The amount of translation respective rotation are of course dependent on the exact crystal structure. Both types of order parameter will be used by us and in the following section we will describe the various order parameters used throughout our computer simulations. In general we find consistency between these different diagnostics but often one of them is much more sharp and pronounced than the others.

As we are in particular interested in a two dimensional freezing in layers parallel to the surface we first have to start by defining a *layer*. We do so by determining the position of the minima in the laterally integrated density profile $\rho(z)$ defined via

$$\rho(z) = \int_{-\infty}^{\infty} dx \int_{-\infty}^{\infty} dy \rho(x, y, z) \tag{3.18}$$

and shown in Figure (3.4) where

$$\rho(\vec{r}) \equiv \rho(x, y, z) = \left\langle \sum_{i=1}^{N} \delta(\vec{r_i} - \vec{r}) \right\rangle \tag{3.19}$$

is the full inhomogeneous one-particle density field defined for the N particles at positions $\vec{r_i}$. $\delta(\vec{r})$ denotes the *Dirac*-Delta function. The minima of $\rho(z)$ define the

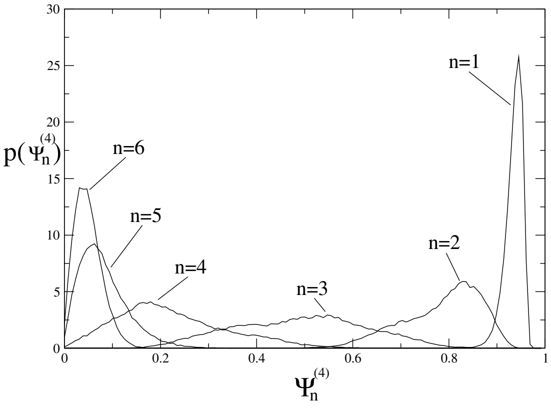

Figure 3.5: Order parameter distribution $P(\Psi_n^{(4)})$ for the first six layers of a hard sphere fluid near a square-patterned wall with four-fold symmetry at $\eta = 0.488$ respectively $P^* = 11.06$.

spacing of the nth layer in the z-direction. The analysis of an order parameter in the nth layer can be performed for each layer, that is for all particles in a chosen layer.

3.5.1 2D bond order parameter

One basic order parameter to detect a crystal at a surface is a bond-order parameter as frequently used in 2D hard disk systems [71, 72]. These bond-orientational order parameters detect the symmetry of the "bonds" between particles. Depending on the lattice symmetry different order parameters are used. A crystal with six-fold symmetry like a triangular surface pattern will be analysed with the $\Psi^{(6)}$ parameter. Quadratic patterns invoke the $\Psi^{(4)}$ parameter and linear ordered systems are analysed using the $\Psi^{(2)}$ order parameter.

In general the order parameter $\Psi_n^{(k)}$ for k-fold symmetry in the nth layer is defined as

$$\Psi_n^{(k)} = \left\langle \left| \frac{1}{N_n} \sum_{l=1}^{N_n} \sum_{j=1}^{N_l} e^{ki\theta_{lj}} \right| \right\rangle \tag{3.20}$$

where θ_{lj} is the angle between the separation vector of the particles l and j and an arbitrary but fixed reference axis. The sum l is over all N_n particles of the nth layer and the sum j is over the N_l neighbors of particle l in the same layer.

For simulation purposes particles are defined as neighbors if the distance between particle l and j is less than $1.35\dots1.40\sigma$. This somewhat arbitrary definition for neighbors can be used as the resulting $\Psi_n^{(k)}$ only weakly depends on the exact definition of a neighbor distance.

An example for the order parameter distribution in different layers for $k = 4$ is shown in Figure (3.5). The distributions clearly shows whether the layer has fluid or solid like bond orientational order: The first layer shows a very pronounced four-fold symmetry. The second layer is still well ordered but less pronounced. The third layer is just at the transition to the ordered four-fold symmetry and all other layers are fluid like.

3.5.2 3D bond order parameter

The two dimensional bond order parameters can be extended to three dimensions. Although these parameters are not well suited for the analysis of surface freezing they find their application in bulk freezing problems. However, we will use a three dimensional bond order parameter for one particular analysis. It had been reported [23] that a structured surface can be used to observe icosahedral order in a fluid below bulk freezing. The analysis of the icosahedral order can be best performed by three dimensional order parameters which are applied to a fluid sheet close to the surface.

According to [73, 74, 75, 76] we can define this order parameter by assigning a set of numbers

$$Q_{lm}(ij) = Y_{lm}\left(\theta_{ij}, \varphi_{ij}\right) \tag{3.21}$$

to every bond between neighboring particles i and j. Neighboring particles are joined by a bond if their distance $|\vec{r_i} - \vec{r_j}|$ is less than a given distance $1.35\dots1.40\sigma$. As above the order parameter only weakly depends of the exact definition of a neighbor. The set of functions $Y_{lm}(\theta, \varphi)$ are spherical harmonics and θ_{ij} and φ_{ij} are the polar angles of the bond between particles i and j with respect to an arbitrary reference axis. Eqn. (3.21) defines a local order parameter which has to be averaged over all bonds to obtain a global order parameter

$$\bar{Q}_{lm} = \frac{1}{N_b} \sum Q_{lm}(ij)\,, \tag{3.22}$$

where the sum is taken over all N_b bonds of the sample or respectively a layer.

The order parameter of Eqn. (3.22) is still dependent on the choice of the reference axis but we can obtain an invariant order parameter by considering the

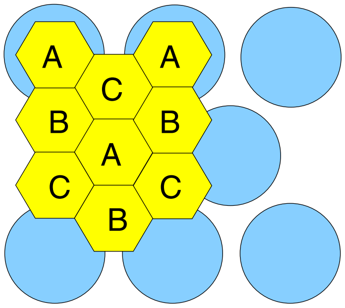

Figure 3.6: Triangular lattice with the three types of honeycomb cells A,B and C defining the stacking order parameter.

second order combination

$$Q_l = \left(\frac{4\pi}{2l+1} \sum_{m=-l}^{l} |\bar{Q}_{lm}|^2 \right)^{1/2} \tag{3.23}$$

and the third order invariant

$$W_l = \sum \begin{pmatrix} l & l & l \\ m_1 & m_2 & m_3 \end{pmatrix} \bar{Q}_{lm_1} \bar{Q}_{lm_2} \bar{Q}_{lm_3} \, , \tag{3.24}$$

where the sum goes over all m_1,m_2 and m_3 with $m_1 + m_2 + m_3 = 0$ and

$$\begin{pmatrix} l & l & l \\ m_1 & m_2 & m_3 \end{pmatrix} \tag{3.25}$$

are the Wigner 3j symbols [77]. A particular good measure [73] for different orientational symmetries can be obtained by the further invariant

$$\hat{W}_l = \frac{W_l}{\left(\sum_{l=-m}^{m} |\bar{Q}_{lm}|^2\right)^{3/2}} \, . \tag{3.26}$$

We will use Eqn. (3.23), Eqn. (3.24) and Eqn. (3.26) to analyse the inhomogeneous fluid for icosahedral order near the surface.

3.5.3 Stacking order parameter

A crystal on top of a triangular or rhombic wall pattern can have different stacking orders. If the wall has the fixed stacking A, the next layer is either packed in B or C and the following can then be either A or C respectively A or B depending on the second one. This can be exploited to define a stacking order parameter Φ_n, which probes how ideal the stacking in the nth layer is and is sensitive to layerwise precrystallization.

In what follows, we explain the definition of Φ_n for a triangular pattern, the generalization to other patterns, in particular the rhombic pattern is straightforward. However, this order parameter cannot be applied to a crystal with unique stacking order.

For each layer n the stacking properties are probed by projecting the particle positions onto the surface. Figure (3.6) depicts the honeycomb like cells A, B and C which correspond to the three stacking possibilities that the projection can fall into. Hence one obtains the averaged probabilities $\{p_n^{(A)}, p_n^{(B)}, p_n^{(C)}\}$ for a particle in the nth layer to be projected into a honeycomb of type A, B or C. The stacking order parameter Φ_n for the nth layer is now defined as the difference between the two largest numbers of the set $\{p_n^{(A)}, p_n^{(B)}, p_n^{(C)}\}$. For a fluid near a non-structured wall, all stacking probabilities are equal, hence Φ_n vanishes. For the first layer of a structured wall, an inhomogeneous liquid has $p_1^{(A)} < p_1^{(B)}$ as it is unlikely for a particle to sit on top of the fixed wall sphere. Furthermore due to symmetry, $p_1^{(B)} = p_1^{(C)}$ and therefore Φ_1 vanishes again. A freezing transition in the nth layer is indicated when $\Phi_n > 0$ corresponding to a broken *discrete* symmetry between the two stacking possibilities. Finally, in a perfect solid with close-packing density, $\Phi_n = 1$.

The order parameter Φ_n has the important property that it is zero in the inhomogeneous fluid phase but nonzero in a crystalline layer. Hence it yields precise information about precrystallization. Figure (3.7) shows an example of the order parameter of the first four layers for a triangular wall as a function of the bulk pressure proving that Φ_n provides a sharp diagnostic for precrystallization.

3.5.4 Minima of the density profile

Another possibility to check the freezing of the system is to analyse the depth of the minima of the lateral integrated density profile $\rho(z)$ as given by Eqn. (3.18) and shown in Figure (3.4). We find that the precrystallization can be detected by a rough empirical criterion. This occurs if the minimal density drops at about 5% of the corresponding bulk density. This criterion is in accordance with the diagnostics using the other order parameters and has the additional advantage that it is robust close to coexistence. In Figure (3.8) we show the direct correspondence of the $\Psi^{(6)}$ order parameter and the minima of the density profile ρ_{min} for a

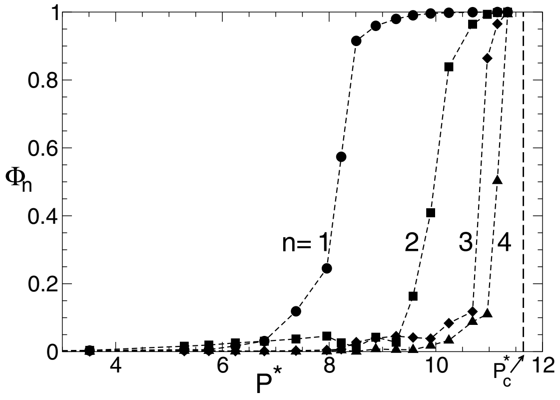

Figure 3.7: Order parameter Φ_n $(n = 1, 2, 3, 4)$ versus reduced pressure P^* for a triangular wall pattern with P_c^* indicating the coexistence pressure of the bulk system. The system size is $L_z/\sigma = 45$ and $A^* = 106$.

system showing triangular crystal layers. For a large part of the order parameter a linear dependency can be found. The data can be fit into the equation $\rho_{\min} = 0.56(0.88 - \Psi^{(6)})$ over the major part of the possible parameters. Only for a very low order parameter, that is, a very fluid like system these characteristics fail as the order parameter saturates whilst the density approaches bulk values.

In Figure (3.4) an example of a density profile is shown where the freezing of the first two layers can be clearly seen by a very small density minimum. The third layer is about to freeze consistent with the diagnostics of the Φ_n and $\Psi_n^{(6)}$ order parameters.

3.5.5 Lindemann parameter

Another order parameter which has proven to be useful in the freezing of a bulk solid is the *Lindemann* parameter [78]. The normalized root-mean-square displacement of particles around their ideal lattice positions $\vec{r_i}$

$$L := \frac{\sqrt{\left\langle (\vec{r_i} - \langle \vec{r} \rangle)^2 \right\rangle}}{\langle \vec{r} \rangle} \tag{3.27}$$

is known as this *Lindemann* parameter L of the solid [79]. It is assumed that a solid melts when the root mean square amplitude of vibration exceeds critical fraction of

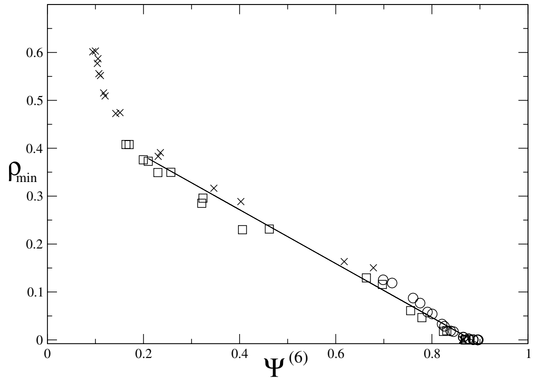

Figure 3.8: The minimum of the density profile $\rho_{\rm min}$ versus the order parameter $\Psi^{(6)}$. The different symbols correspond to different systems and the straight line is the best linear fit to all data.

lattice spacing which leads to the traditional *Lindemann* melting rule [78]. It states that a bulk solid melts if L is roughly about 10%. In our computer simulations in the following chapters we will check if this rule applies also for interfacial freezing. In order to do so, we define a layer-resolved *Lindemann* parameter L_n by applying Eqn. (3.27) to all particles in the nth layer.

Chapter 4

Surface free energy

Most of the physical properties of a solid or liquid in contact with a substrate such as wetting, spreading and heterogeneous nucleation, are governed by the interfacial free energies between the substrate and the material [80]. Thus, a microscopic theory of surface tensions is highly desirable in order to predict the wettability of a given substrate for different materials [1]. Since the surface tension clearly depends upon the microscopic interactions between the particles of both the substrate and the material, such a theoretical calculation generally represents a formidable task.

In this chapter we calculate equilibrium surface free energies for one specific type of microscopic interaction. To achieve a principal understanding of the surface free energies we model the interaction between the particles as hard spheres and describe the substrate as a hard structureless planar wall.

The hard sphere *fluid* near a hard wall is a standard situation which has been studied in numerous publications. Computer simulations for the density profiles are available and theories, in particular density functional approximations of inhomogeneous systems [2, 81], have been tested against the simulation data. However, much less investigated is the interfacial free energy γ itself which is harder to extract from the simulation data since it either requires evaluation of the pressure tensor at the wall [82] or thermodynamic integration over a set of simulation runs [59]. Only few density functional studies are available using the weighted density approximation [83] or variants of it [84] and an analytical scaled-particle expression is known [48, 85, 86]. In this chapter we revisit the surface free energies for the fluid hard sphere system and show that the scaled-particle theory and density functional theory compare well with the simulation data. However, for high densities close to freezing the published density functional calculation deviates significantly from our simulation data.

Further, we then have extended the study to encompass a hard sphere *solid* near a hard wall where knowledge remains sparse. The associated interfacial free energy γ now depends also on the orientation of the solid with respect to the wall normal. Apart from a density functional study at the melting point [83], no data for γ have been published in the literature.

4.1 The model

We consider a hard sphere model as described in chapter 2 where we consider N hard spheres with diameter σ in a large volume V at a fixed temperature T. The finite number density of the spheres is $\rho = N/V$ which can conveniently be expressed in terms of the dimensionless packing fraction $\eta = \pi\rho\sigma^3/6$. In detail, the center-of-mass positions of the spheres are denoted by $\vec{r}_i = (x_i, y_i, z_i)$ $(i = 1, \ldots, N)$. Two hard spheres i and j interact via the pair potential Eqn. (2.1). In the following we extend the model by including a surface in the hard sphere system. The presence of such a wall is described by an additional external potential

$$W(z_i) = \begin{cases} 0 & |z_i| > \sigma/2 \\ w(z_i) & \text{otherwise} \end{cases} \tag{4.1}$$

which acts on the centers of the ith hard sphere $(i = 1, \ldots, N)$. For the sake of convenience the wall position is at $z = 0$ in a plane parallel to the $x - y$ plane. The actual wall area is A. Although we have a hard impenetrable wall in mind we keep the description more general by allowing also penetrable wall potentials where the function $w(z)$ is finite. For symmetry reasons, $w(z)$ should be an even function, that is $w(-z) = w(z)$. The bulk system is recovered for a vanishing $w(z)$ while a hard wall is described by $w(z) \to \infty$ for any $|z| \leq \sigma/2$.

4.2 Computer simulations

We simulate the hard sphere fluid and the hard sphere crystal using a rectangular simulation box of size $V = L_x L_y L_z$ with periodic boundary conditions in all directions. Moreover we can add any given wall potential $W(z)$ according to Eqn. (4.1) to the system. The total surface area of the simulation box is then

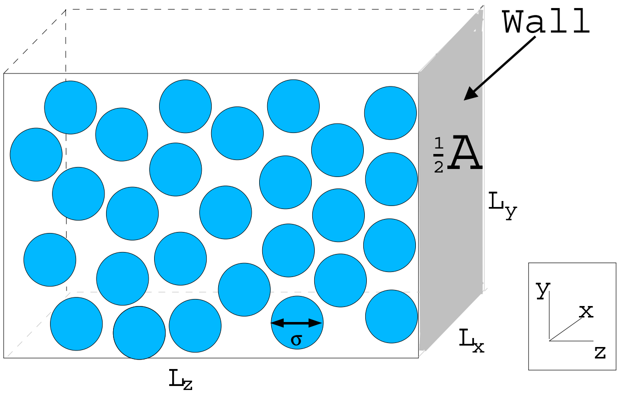

Figure 4.1: Geometry of the hard sphere system under consideration. The simulation box has a volume $V = L_x L_y L_z$ and contains N particles of diameter σ. The total hard sphere system - hard wall contact area is $A = 2L_x L_y$.

$A = 2L_x L_y$ since in our set-up any single wall applied to the system will appear doubled at both ends of the simulation cell, see Figure (4.1).

We use standard NVT *Monte-Carlo* simulation techniques as described in section 3.2.2 keeping the volume and the particle number of the system fixed. However, we apply these *Monte-Carlo* simulations to interfacial problems [87, 88]. In order to check ensemble independence we have also performed constant pressure simulations (NP_zT) as also described in section 3.2.2. The advantage of this approach is that it allows the system to compensate internal stress. Within the statistical uncertainties both set-ups yield the same interfacial tensions up to high densities of about $\eta \approx 0.66$ which shows *a posteriori* that the system size in our NVT-simulation was large enough. For even higher densities the stress introduced in the NVT simulation is responsible for the slight differences and thus the NPT simulation prove to be more suitable.

As discussed in chapter 3.3 the size of the system in the z-direction, that is perpendicular to the wall must be large enough to avoid capillary effects and other spurious mutual influences on the two walls. In addition, large surface areas are required to exclude any line effects. System sizes of about 500-2000 particles yielding surface areas $A/2$ of about $30 - 60\sigma^2$ and an extension into the z-direction of about $L_z = 30 - 40\sigma$ have been used during our simulations. In order to avoid lateral compressional strains in the crystal, the length L_x and L_y where adjusted to the given crystallographic orientation such that a laterally periodic bulk crystal fits exactly into the simulation box.

4.3 Calculating surface tensions

The total potential energy of the system is

$$U_p(\{\vec{r_k}\}) = \sum_{i=1}^{N} W(z_i) + \sum_{i,j=1;i<j}^{N} U(\vec{r}_i, \vec{r}_j) \tag{4.2}$$

resulting in the canonical partition function

$$Q(N,V,A,T) = \frac{1}{\Lambda^{3N} N!} \int d^3r_1 \ldots \int d^3r_N \, e^{-\beta U_p(\{\vec{r_k}\})} \tag{4.3}$$

where $\{\vec{r_k}\} = (\vec{r}_1, \ldots, \vec{r}_N)$, $\beta = 1/(k_B T)$ and Λ being the (irrelevant) thermal wavelength. The canonical free energy is finally gained as

$$F(N,V,A,T) = -k_B T \, \ln Q(N,V,A,T)\,. \tag{4.4}$$

In the bulk case ($w(z) \equiv 0$), the density is not dependent of area A. Hence we can simply write $F(N,V,A,T) = k_B T F^*{}_{Bulk}(\eta)$ where $F^*{}_{Bulk}$ is a dimensionless quantity. Introducing a wall of area A adds A as an additional thermodynamical variable. In leading order, the full free energy splits into a bulk and a surface contribution [2]

$$F(N,V,A,T) = k_B T F^*_{Bulk}(\eta) + \gamma(\eta,T)A + O(L) \tag{4.5}$$

where $\gamma(\eta,T)$ is the interfacial free energy of the system and L is a typical edge length of the system. In other words, the interfacial free energy is the excess free energy per area

$$\gamma(\eta,T) = \frac{F(N,V,T,A) - k_B T F^*_{Bulk}(\eta)}{A} \tag{4.6}$$

and can be equivalently defined via

$$\gamma = \frac{\partial F(N,V,T,A)}{\partial A}\Big|_{N,V,T}\,. \tag{4.7}$$

We finally note that for a hard wall $\gamma(\eta,T) = k_B T \tilde{\gamma}(\eta)$ such that the only non-trivial dependence is on the bulk packing fraction. A suitably reduced quantity is $\gamma^*(\eta) = \tilde{\gamma}(\eta)\sigma^2$. It is this target quantity which we calculate and discuss in the sequel over the whole range of packing fractions both in the fluid and crystalline

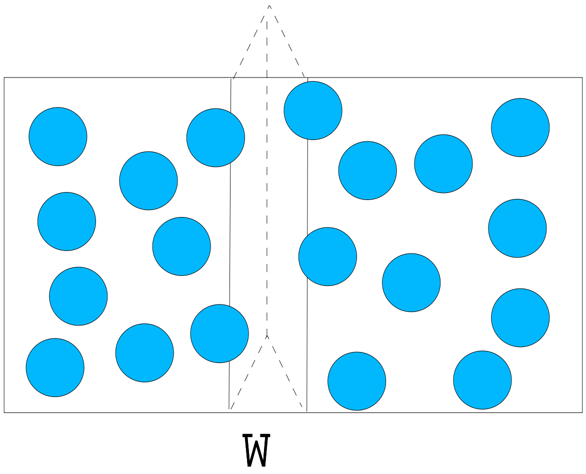

Figure 4.2: Schematic drawing of the insertion of a wall with triangular wall potential into the hard sphere system.

bulk phase. In the non-homogeneous crystalline phase, the interfacial free energy γ^* will additionally depend on the orientation of the solid with respect to the wall. Of course, due to thermodynamic stability, γ^* has to be positive.

To gain access to the interfacial free energy, there are basically two routes one can follow. One can use microscopic relations relating the pressure tensor to the interfacial free energy [82]. This has the advantage of needing less computer runs but requires exact knowledge of the density and the one-particle correlation functions at contact. Extrapolating these quantities with high precision is extremely difficult, as they change rapidly near contact for high densities. We therefore choose another method namely *thermodynamic integration* as discussed in chapter 3.4, which gives the free energy of the simulated system with respect to that of a known reference system. From the free energy difference of the system with wall compared to the bulk system we can calculate the surface energy directly from Eqn. (4.6). To compute γ^*, this method requires a whole set of simulations but is still applicable for high densities.

Applying the technique of thermodynamic integration from section 3.4, we start from the known bulk hard sphere system and insert a gradually increasing wall potential, that is we simulate a less and less penetrable wall. The wall potential $W(z) \equiv W(z;\lambda)$ is parameterized with a parameter λ which is chosen to give no wall for $\lambda = 0$, a less and less penetrable wall for increasing λ and finally a hard wall for $\lambda \to \infty$. Different wall potentials $w(z;\lambda)$ or the details of the switching on procedure do not change the final result for the free energy and interfacial free energy as long as a reversible integration path is followed. The details of the parameterization, however, will influence the equilibration time and the accuracy of the numerical integration. For the fluid we found the square potential $w(z;\lambda) = \lambda$ sufficient for the thermodynamical integrations. A better choice of the parameterization is a triangular potential $w(z;\lambda) = 2\lambda(1 - 2|z|/\sigma)$ which leads to a quicker equilibration and a smoother integrand especially for a bulk solid. A schematics of this process is shown in Figure (4.2).

For consistency, we have checked that both parameterizations lead to the same final result.

To integrate the free energy we need its derivative with respect to the integration parameter λ. This quantity can be written as a statistical average and is thus directly accessible by computer simulations. Consequently,

$$\begin{aligned}
\left.\frac{\partial F}{\partial \lambda}\right|_{NVAT} &= -k_B T \frac{1}{Q} \left.\frac{\partial Q}{\partial \lambda}\right|_{NVAT} \\
&= \frac{1}{Q} \frac{1}{\Lambda^{3N} N!} \int d^3 r_1 \ldots \\
&\qquad \int d^3 r_N \left(\sum_{i=1}^{N} \frac{\partial W(z_i;\lambda)}{\partial \lambda} \right) \exp^{-\beta U(\{\vec{r}\};\lambda)} \\
&= \left\langle \sum_{i=1}^{N} \frac{\partial W(z_i;\lambda)}{\partial \lambda} \right\rangle_{\lambda} && (4.8) \\
&=: \Phi(\lambda) && (4.9)
\end{aligned}$$

where $< \ldots >_\lambda$ denotes a canonical average with a penetrable wall. A typical example of the integrand $\Phi(\lambda)$ of the thermodynamical integration is shown in Figure (4.3) for a triangular potential. One sees that typically 10-20 integration points are necessary. For large λ, the integrand could be well fitted by an algebraic decay $\propto \lambda^{-2}$ which was used to estimate the tail of the integrand. The integrand $\Phi(\lambda)$ is positive which implies that the interfacial tension for a penetrable wall is smaller than that for a hard wall.

Using Eqn. (4.6) the interfacial free energy γ of the system with a hard wall can be written as

$$\gamma = \frac{\int_0^\infty d\lambda\, \Phi(\lambda)}{A}. \tag{4.10}$$

We used different system sizes and surface areas to estimate the statistical and finite size errors in the calculation. Within the different system sizes used in our

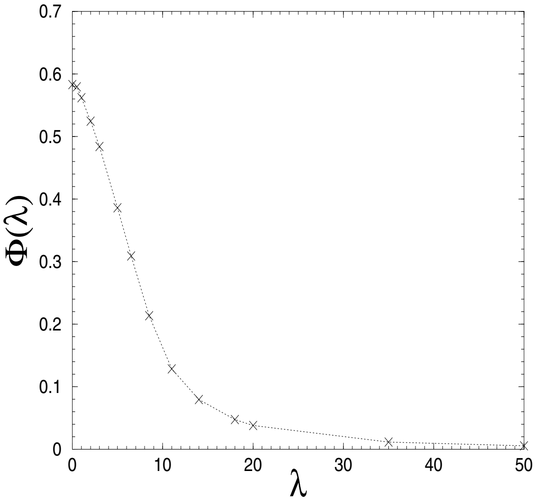

Figure 4.3: Integrand $\Phi(\lambda)$ as dimensionless quantity versus λ for a hard sphere FCC crystal at $\eta = 0.63$ in (111) orientation using a triangular wall potential.

simulations, we do not find any systematic corrections. This indicates that our systems are large enough.

4.4 Hard sphere fluid near a hard wall

The interfacial tension of a hard sphere fluid (that is $\eta < \eta_f$) at a hard wall can be analytically calculated within scaled-particle theory (SPT) [48, 85]. The key quantity of SPT is $\overline{\gamma} \equiv \gamma - P\sigma/2$ (with P being the bulk pressure) which is in general negative. SPT yields

$$\overline{\gamma}_{\mathrm{SPT}} = -k_B T \frac{9}{2\pi\sigma^2} \eta^2 \frac{1+\eta}{(1-\eta)^3} \,. \tag{4.11}$$

In SPT the bulk pressure is equivalent to the bulk pressure obtained by the Percus-Yevick compressibility equation of state [48]. Therefore remaining inside SPT one has to add

$$P_{\mathrm{PY}}\sigma/2 = k_B T \frac{6}{\pi} \eta \frac{1+\eta+\eta^2}{(1-\eta)^3} \tag{4.12}$$

η	γ^*	N	$A/2\sigma^2$
0.100	0.124 ±0.05	684	59.22
0.200	0.325 ±0.02	504-1008	49.74
0.300	0.656 ±0.03	480-1024	50.61
0.400	1.195 ±0.11	1024	41.78
0.436	1.543 ±0.08	1024	39.42
0.472	1.726 ±0.07	1008	28.10
0.490	1.890 ±0.09	1008-2500	57.02

Table 4.1: Simulation results for the fluid: Given are the packing fraction η, the interfacial free energy γ^* with its statistical error and number N of particles in the simulation box as well as the maximal surface area $A/2$ used in the simulation.

as bulk pressure in order to get γ_{SPT}. Yet a more accurate alternative is to use the *Carnahan-Starling* equation of state [65] to obtain the bulk pressure

$$P_{\mathrm{CS}}\sigma/2 = k_B T \frac{6}{\pi}\eta \frac{1+\eta+\eta^2-\eta^3}{(1-\eta)^3}. \tag{4.13}$$

In the following we will use bulk pressure Eqn. (4.13) to obtain the interfacial free energy $\gamma_{\mathrm{SPT}} = \overline{\gamma}_{\mathrm{SPT}} + P_{\mathrm{CS}}\sigma/2$.

Another theoretical approach to obtain γ is via the classical density functional theory (DFT) of inhomogeneous systems. Using different variants of the weighted-density-approximation, the interfacial free energy was calculated by *Götzelmann et al.* [84] for moderate densities and by *Ohnesorge et al.* [83] near freezing.

Data for γ from *Molecular-Dynamics* (MD) simulations were known already for four different densities in Ref. [82]. Moreover [86] uses simulation results to fit the interfacial free energy to an empirical formula for γ.

We have applied our scheme of thermodynamic integration to this problem and obtained further data for γ on a finer density grid and up to higher densities which are given in Table 4.1.

All data available are summarized in Figure (4.4). The scaled-particle theory is in good agreement with the simulation if the bulk pressure is taken from the *Carnahan-Starling* equation. DFT provides good data for moderate densities but fails near freezing. We remark here that the discrepancies at freezing might be due to the actual approximation used for the density functional.

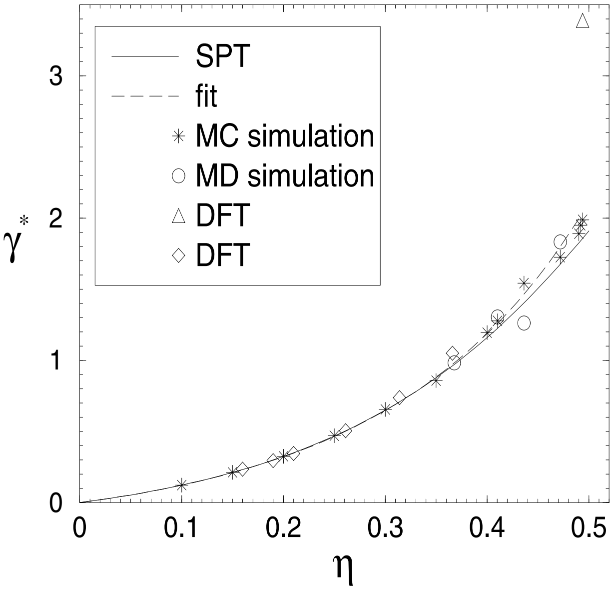

Figure 4.4: Reduced interfacial free energy γ^* of the hard sphere fluid in contact with a hard wall versus packing fraction η. Solid line: scaled-particle theory with *Carnahan-Starling* equation of state; dashed line: empirical fit from Ref. [86]; $*$: our simulation data; open circle: MD simulation from Ref. [82]; diamonds: DFT from Ref. [84]; triangles: DFT from Ref. [83].

We finally remark that precrystallization on the hard wall occurs very close to the bulk freezing transition [89]. The thermodynamic integration method, however, is not applicable if a phase transition is crossed along the integration. As is common in any wetting problem, we have consequently *extrapolated* the data from lower densities $\eta \approx 0.49$ to the freezing density $\eta_f = 0.494$ to extract the metastable wall-fluid surface tension at freezing. We obtained $\gamma^* = 1.99 \pm 0.18$ which is about 7% above the theoretical value predicted by scaled-particle theory combined with the *Carnahan-Starling* equation of state.

4.5 Cell theory of the hard sphere crystal

4.5.1 General idea

The cell theory (CT) provides a simple analytical estimate of the bulk free energy of the hard sphere crystal [90, 91, 92]. It was also applied to compute the elastic

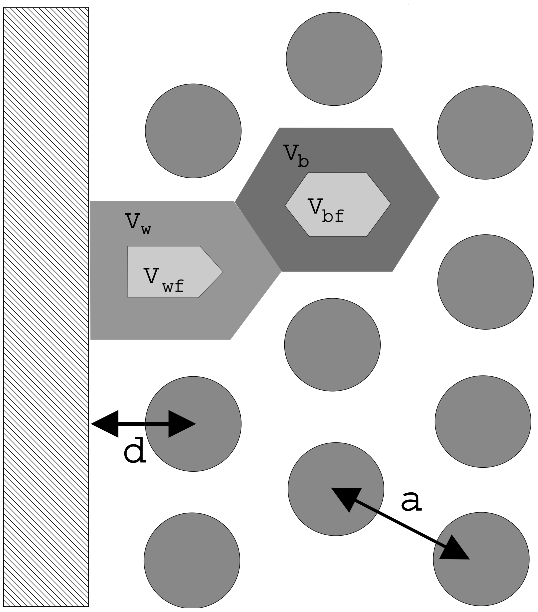

Figure 4.5: Two-dimensional hard disk crystal in (11) orientation near the hard wall. The Wigner-Seitz cell volume (respectively area) for a bulk particle, V_{b}, and for a wall particle, V_{w}, is shown. Inside these cells the free volume cell is indicated as V_{wf} and V_{bf}. The distance of the first layer of particles to the wall is d and the bulk mean particle distance is a.

constants of the hard sphere solid [93] and the location of solid-solid transitions in confining geometry [94]. In the following we shall generalize this concept to extract the interfacial free energy of a hard sphere solid near a hard wall for different orientations. The situation is schematically shown for a two-dimensional hard disk crystal along (11) orientation in Figure (4.5).

As there are no major differences between the two- and three-dimensional analysis, we calculate in the general spatial dimension D and apply the parameter for the dimensions ($D = 2, 3$) later on. Let us first recapitulate on the bulk theory: In a given solid lattice, the particles have a bulk mean particle distance a which is the distance between nearest neighbors of the lattice. We consider the particles to be confined in independent Wigner-Seitz (or Voronoi) cells of the solid. This cell has a volume $V_{\mathrm{b}} = g_b a^D$ where g_b is a geometrical prefactor that depends on the lattice type and on dimensionality D. Each center-of-mass coordinate of the hard spheres can move within a free volume [36] of

$$V_{\mathrm{bf}} = g_b (a - \sigma)^D \tag{4.14}$$

without touching the neighboring spheres. Hence one obtains a lower bound for the bulk partition function, $Q \geq \left(\frac{V_{\mathrm{bf}}}{\Lambda^D}\right)^N$, which provides an upper bound to the bulk free energy:

$$F \leq -Nk_BT \ln\left(\frac{g_b(a-\sigma)^D}{\Lambda^D}\right) . \tag{4.15}$$

This upper bound becomes asymptotically exact for close-packing occurring for $\eta \to \eta_{CP} = \pi\sqrt{2}/6 = 0.741...$ (3D) [36].

We now include a hard wall which induces an inhomogeneity in the problem. We assume that the wall will only influence the first layer of the crystal. This introduces the distance of the center of-mass coordinates in the first layer to the wall as new parameter d, see again Figure (4.5). All other layers of the crystal are treated within the bulk-approach. To be specific let us first consider a closed packed orientation, the (111) orientation in 3D respectively the (11) orientation in 2D. The form of the Wigner-Seitz cell of the wall particles is different from the bulk. It has a volume

$$V_{\mathrm{w}} = \frac{V_{\mathrm{b}}}{2} + g_w d a^{D-1} \tag{4.16}$$

where g_w is a further geometric prefactor depending on the lattice type, the orientation and on D. The free volume accessible for the wall particles is

$$V_{\mathrm{wf}} = \frac{V_{\mathrm{bf}}}{2} + g_w(d - \frac{\sigma}{2})(a-\sigma)^{D-1} . \tag{4.17}$$

Again we get an upper bound for the free energy within this approach. If one optimizes this bound one gets $V_{\mathrm{bf}} = V_{\mathrm{wf}}$ which yields

$$d = \frac{g_b}{2g_w}(a-\sigma) + \frac{\sigma}{2} \tag{4.18}$$

resulting in the same free energy per particle as in the bulk case. Equivalently this can be deduced from the principle of maximization of entropy. The principal difference now is that the mean distance $a = a(N, V, A)$ depends implicitly on the particle number N, the physical total volume V and on the area A. The dependence is explicitly obtained by splitting the total volume into a bulk and a surface part

$$\begin{aligned} V &= (N - N_w)V_{\mathrm{b}} + N_w V_{\mathrm{w}} \\ &= N g_b a^D - \frac{A}{g_w a^{D-1}}\left(\frac{g_b}{2}a^D - g_w d a^{D-1}\right) \\ &= N g_b a^D + \sigma A\left(\frac{g_w - g_b}{2g_w}\right) \end{aligned} \tag{4.19}$$

where $N_w = A/(g_w a^{D-1})$ is the number of particles touching the wall. Eqn. (4.19) gives the desired relation $a = a(N, V, A)$. Finally, the interfacial tension is analytically obtained by combining Eqn. (4.15) to Eqn. (4.7) as

$$\gamma \equiv \gamma_{CT} = k_B T \frac{\sigma}{(a-\sigma)a^{D-1}} \frac{1}{2 g_w g_b} (g_w - g_b) \tag{4.20}$$

where a now is the bulk mean particle distance. Differently to the bulk theory, γ_{CT} does not provide an upper bound for the exact interfacial tension. Before inserting the appropriate geometric factors for the different crystal orientations we note that this model applies well for fairly close packed surfaces, that is crystal orientations in 3D along (111) or even (100) orientation and in 2D along the (11) orientation. For looser packed orientations as the (110) orientation in 3D and the (10) orientation in 2D the calculation becomes more complicated as the free cells and Wigner-Seitz cells of the second layer cannot be neglected anymore. Nevertheless the principles of the cell theory can be applied as well but the calculations become more tedious. We therefore refer to the Appendix for details of the calculations.

Explicitly, for $D = 2$ in (11) orientation, $g_b = \sqrt{3}/2$ and $g_w = 1$. Hence Eqn. (4.20) reduces to

$$\gamma_{CT} \equiv \gamma_{CT}^{(11)} = k_B T \frac{1}{\sqrt{3}} \frac{\sigma}{(a-\sigma)a} \left(1 - \frac{\sqrt{3}}{2}\right) \tag{4.21}$$

with the bulk mean particle distance $a = \sigma\sqrt{\frac{\pi}{2\sqrt{3}\eta}}$, η denotes the area fraction. In (10) orientation, we can expand the exact solution given in the Appendix to first order and obtain $g_b = \sqrt{3}/2$ and $g_w \approx \sqrt{3}$.

For $D = 3$ in (111) orientation, on the other hand, $g_b = 1/\sqrt{2}$ and $g_w = \sqrt{3}/2$ and Eqn. (4.20) yields

$$\gamma_{CT} \equiv \gamma_{CT}^{(111)} = k_B T \frac{\sqrt{3} - \sqrt{2}}{\sqrt{3}\sqrt{2}} \frac{\sigma}{(a-\sigma)a^2} \tag{4.22}$$

with the bulk mean particle distance $a = \sigma \left(\frac{\sqrt{2}\pi}{6\eta}\right)^{1/3}$. In (100) orientation, we obtain $g_b = 1/\sqrt{2}$ and $g_w = 1$ and in (110) orientation the first order expansion of the exact solution as calculated in the Appendix gives the geometric factor $g_b = 1/\sqrt{2}$ and $g_w \approx \sqrt{2}$.

4.5.2 Cell theory with fixed neighbors

The cell theory neglects configurations of collective movements of neighboring particles from their lattice position. These can be approximately included by keeping all neighbors fixed on their lattice positions. This yields a better free energy for densities away from close-packing and also locates the melting point better than the original CT. Then, of course, the bulk theory is no longer an upper bound to the exact free energy. This assumption can be directly transferred to the interfacial situation by assuming larger free volume cells. The final result in this cell theory with fixed neighbors (CTFN) is

$$\gamma_{CTFN} = k_B T \frac{\sigma}{(a-\sigma)a^{D-1}} \frac{1}{g_w g_b} \left(\frac{g_w}{2} - g_b + \frac{g_b}{2} \frac{a}{\sigma} \right) \tag{4.23}$$

which gives for $D = 2$ in (11) orientation

$$\gamma^{(11)}_{CTFN} = k_B T \frac{2}{\sqrt{3}} \frac{\sigma}{(a-\sigma)a} \left(\frac{1}{2} - \frac{\sqrt{3}}{2} + \frac{\sqrt{3}}{4} \frac{a}{\sigma} \right) \tag{4.24}$$

and for $D = 3$ in (111) orientation

$$\gamma^{(111)}_{CTFN} = k_B T \frac{\sigma}{(a-\sigma)a^2} \left(\frac{1}{\sqrt{2}} - \frac{2}{\sqrt{3}} + \frac{1}{\sqrt{3}} \frac{a}{\sigma} \right) . \tag{4.25}$$

The results for the 2D (10) orientation and the (100) and (110) orientations in 3D can be readily calculated by inserting the geometric factors from above into Eqn. (4.23).

Intuitively, it is expected that the true interfacial free energy will be bounded by the CT and the CTFN theory and that the CTFN theory will work better than the CT theory.

4.5.3 Results in two dimensions

Results within the CT and CTFN theory are displayed for $D = 2$ in Figure (4.6) for (11) and (10) orientation. A crystal is stable for area fractions between freezing at $\eta_s = 0.71$ [95] and close-packing occurring at $\eta_{cp} = \pi/(2\sqrt{3}) = 0.907...$. The whole stability region of the 2D-crystal is shown in Figure (4.6). The CTFN produces higher interfacial free energies than the simple CT. Furthermore, the (11) orientation has a significantly lower interfacial free energy than the (10) orientation since a linear chain of disks is better packed along a hard line than a zig-zig

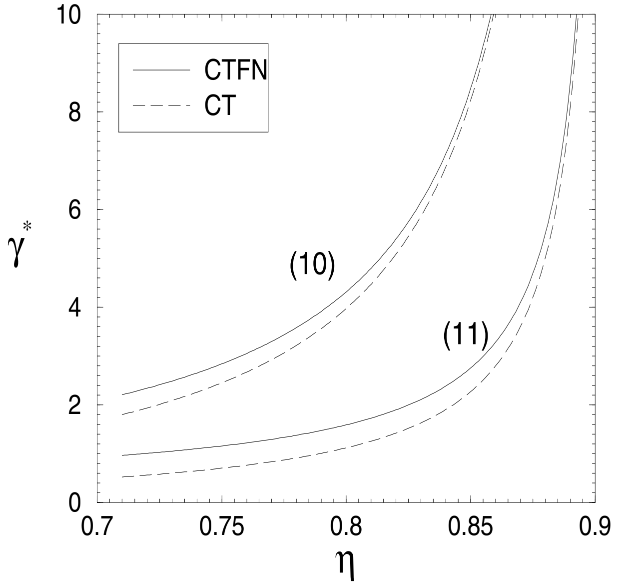

Figure 4.6: Reduced interfacial free energy $\gamma^* = \gamma\sigma/(k_B T)$ of a two-dimensional hard disk crystal in contact with a hard line versus bulk area fraction η. Both (11) and (10) orientations are shown for the CT (dashed lines) and the CTFN (solid lines).

structure as realized for the (10) orientation which is rotated about an angle of 30^o with respect to the (11) orientation. Clearly, in both cases, γ diverges as close-packing is approached.

4.6 Simulation results for the hard sphere crystal

4.6.1 The interfacial free energy in 3D

Results for γ^* for different orientations and bulk densities are shown in Figure (4.7) and collected in Table 4.2. The statistical errors results from averaging over a set of identical simulations. However, with our choice of the integration parameters we are not able to fully equilibrate the systems for densities larger than $\eta \approx 0.70$. This is due to the fact that inserting a wall will shift particles away from the wall. At these high densities this leads to longer and longer equilibration times. Therefore, a more sophisticated wall insertion and longer computer runs would be needed to extend the simulations beyond these densities. We did not pursue this

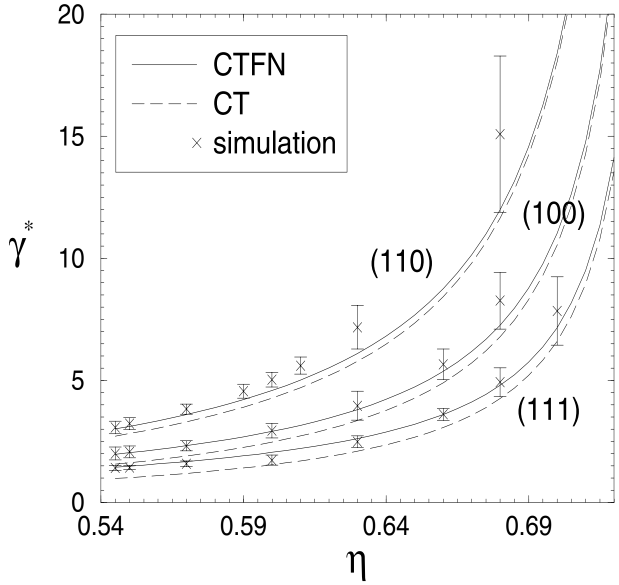

Figure 4.7: Reduced interfacial free energy γ^* of a hard sphere crystal in contact with a hard wall versus bulk packing fraction η. The dashed lines are from CT and the solid lines from CTFN. The crosses are the simulation results. From top to bottom: (110), (100) and (111) orientation.

further as the asymptotic results are known from the CT and CTFN.

As becomes evident from Figure (4.7) there is good agreement of the simulation data with the simple cell theory over the whole range of packing fractions η. In particular, the CTFN almost perfectly reproduces the simulation data for (111) and (100) orientation. The relative differences between the CTFN theory and simulation at freezing ($\eta = 0.545$) is less than two percent.

Moreover it is interesting to compare the ratio of the surface tension for different orientations. Simulation data yields a ratio of $\gamma^*_{110} : \gamma^*_{100} : \gamma^*_{111} = 2.2 : 1.4 : 1.0$ near bulk freezing ($\eta = 0.545$) and a ratio of $\gamma^*_{110} : \gamma^*_{100} : \gamma^*_{111} = 2.8 : 1.5 : 1.0$ for higher bulk densities of $\eta = 0.63$. It is appealing to compare these ratios with a picture of broken bonds to the nearest neighbors where one gets $\gamma^*_{110} : \gamma^*_{100} : \gamma^*_{111} = 2.0 : 1.3 : 1.0$ for all densities. Indeed these ratios are very similar for the hard sphere system although there are actually no bonds generated by our interaction potential.

Finally, the interfacial tensions for (110) and (100) orientations are larger than that for the (111) orientation. This implies that a solid will pick the (111) orien-

η	$\gamma^*(111)$	$\gamma^*(100)$	$\gamma^*(110)$	N	$A/2\sigma^2$
0.545	1.42 ± 0.10	2.01 ± 0.26	3.08 ± 0.26	504-1500	53.12
0.550	1.43 ± 0.09	2.08 ± 0.24	3.24 ± 0.24	504-1408	33.79
0.570	1.59 ± 0.12	2.32 ± 0.21	3.83 ± 0.21	1024-1408	32.99
0.600	1.74 ± 0.21	2.95 ± 0.30	5.03 ± 0.30	1500	49.82
0.630	2.49 ± 0.24	3.97 ± 0.59	7.18 ± 0.89	504-1408	30.86
0.680	4.93 ± 0.58	8.26 ± 1.16	15.08 ± 3.20	1024	29.33
0.700	7.85 ± 1.40			1024	28.77

Table 4.2: Simulation results for the crystal. Shown are the packing fractions η, the interfacial free energy γ^* for different orientations of the crystal with their statistical error and number N of particles in the simulation box as well as the maximal surface area $A/2$ used in the simulation.

tation which provides the most efficient packing near a planar hard wall.

4.6.2 Cumulants of the density profile in the first layer

Another important quantity which is the output of any density functional calculation is the inhomogeneous equilibrium one-particle density $\rho(\vec{r})$. Our simple cell theory assumes a homogeneous density distribution within the free cells. We have tested this against computer simulation data. To be specific we introduce cumulants of the density profile within the first adjacent crystalline layer by defining the moments

$$\overline{z^m} = \frac{\int_{-\infty}^{\infty} dx \int_{-\infty}^{\infty} dy \int_0^{z_0} dz\, z^m \rho(x,y,z)}{\int_{-\infty}^{\infty} dx \int_{-\infty}^{\infty} dy \int_0^{z_0} dz\, \rho(x,y,z)} \,. \tag{4.26}$$

where z_0 denotes the position of the first minimum in the laterally averaged density profile. From this sequence of moments one can deduce several important quantities. First the averaged distance of the first layer from the wall can be gained by $\overline{z}$. We normalize this quantity appropriately by considering $d^* = \overline{z}/\sigma$. The second moment $\overline{z^2}$ is related to the width of the density profiles in z-direction. We define the reduced second cumulant by

$$w^* := \frac{\sqrt{\overline{z^2} - \overline{z}^2}}{a} \,. \tag{4.27}$$

In the bulk system this quantity is proportional to the Lindemann parameter L of the solid describing the root-mean-square displacement around the lattice positions normalized by a. In fact, $w^* = L/\sqrt{3}$. Finally we define the third cumulant (or the reduced skewness) s^* via

$$s^* := \frac{\left(\overline{(z-\overline{z})^3}\right)^{1/3}}{\sqrt{\overline{z^2}-\overline{z}^2}} = \frac{\left(\overline{z^3} - 3\overline{z^2}\,\overline{z} + 2\overline{z}^3\right)^{1/3}}{\sqrt{\overline{z^2}-\overline{z}^2}} \,. \tag{4.28}$$

The skewness s^* characterizes the degree of asymmetry of a distribution around its mean. Positive skewness indicates a distribution with an asymmetric tail extending towards more positive values. Negative skewness indicates a distribution with an asymmetric tail extending towards more negative values. The skewness for a normal distribution is zero, and any symmetric data should have a skewness near zero. Obviously, $s^* = 0$ in the bulk system due to inflection symmetry.

In the cell theory the density $\rho(x, y, z)$ is assumed to be uniformly distributed over the free cell. Hence the moments are directly obtained by integrating over the free cell. In the simulation the density $\rho(x, y, z)$ is readily calculated and used as input into Eqn. (4.26).

Results for the distance d^* of the first layer from the wall are presented in Figure (4.8). d^* varies almost linearly with the bulk packing fraction η. The cell theory yields reasonable values in comparison with the simulation. As close-packing is approached, the first layer sticks to the wall, hence $d^* \to 0.5$ in this limit.

In Figure (4.9) we present the reduced width w^* of the first layer versus packing fraction η. The presence of the wall significantly restricts the motion of the particles in the first layer into z-direction. This becomes evident by comparing the simulation data with the bulk Lindemann parameter at bulk freezing [79]: The bulk width is 0.074 while the wall results in a strongly reduced width of $w^* = 0.043 \pm 0.001$. Again the cell theories yield reasonable values and correct trends when compared with the simulation data. The η-dependence is again almost linear.

Finally, in Figure (4.10), the skewness s^* of the first layer is shown. It is of the order of unity indicating a significant asymmetric density distribution distorted by the wall. The reduced skewness is practically independent of η. The cell theories both underestimate s^* by a factor of one half but also do not exhibit any η-dependence. The increasing deviations between cell theory and simulation as the order of the cumulants grows is due to the fact that the higher moments are more sensitive to the tail of the distribution. This tail is not correctly described by a sharp-kink density profile as assumed in cell theory. We remark that a better

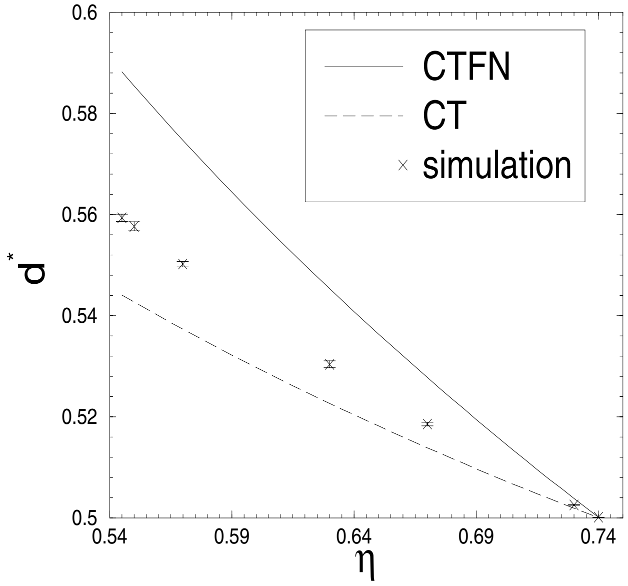

Figure 4.8: Reduced distance d^* of the first layer from the wall for FCC (111) orientation versus bulk packing fraction η. The dashed lines are from CT and the solid lines from CTFN. The crosses are the simulation results.

theoretical description of the cumulants can be obtained by density functional calculations. A detailed comparison with our simulation result should provide a stringent test of the current density functional approximations.

4.7 Conclusions

We have calculated the interfacial free energy of a hard sphere fluid and a hard sphere solid near a hard wall over the whole range of bulk densities for the fluid and for the solid at (111), (110) and (100) orientation. Furthermore, we proposed a simple solid cell model for this interface resulting in a simple analytical expression for γ and we found good agreement between the computer simulations and the analytical cell theory. Our work demonstrates that the thermodynamic integration method can be applied to surface problems and provides benchmark data to test the ability of more elaborate theories as the recently developed Rosenfeld density functional theory [96, 97, 98].

Recently, the equilibrium interfacial free energy between a fluid and a solid [99] at coexistence have been calculated for different orientations by *Davidchack*

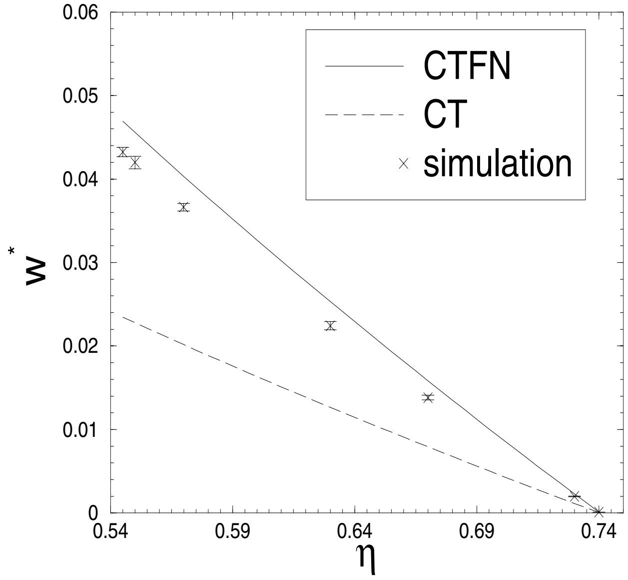

Figure 4.9: Same as Figure (4.8) but now for the reduced width w^*.

et al. [100]. Their results are for the (111) orientation $\gamma_{sf} = 0.58 \pm 0.01 k_B T/\sigma^2$, for the (100) orientation $\gamma_{sf} = 0.62 \pm 0.01 k_B T/\sigma^2$ and for the (110) orientation $\gamma_{sf} = 0.64 \pm 0.01 k_B T/\sigma^2$. Combining these results with our data for the surface free energies does in principle allow a definite answer to the long discussed question whether a hard sphere fluid prefreezes close to a flat hard wall. If the surface free energies fulfill $\gamma_{ws} + \gamma_{sf} < \gamma_{wf}$, it will be favorable for the system to form a crystalline layer inbetween the wall and the fluid. However, if we add the surface free energies from our work and [100] we obtain from the above equation for the (111) direction $\gamma_{ws} + \gamma_{sf} = 2.00 \pm 0.19 k_B T/\sigma^2$ and $\gamma_{wf} = 1.99 \pm 0.18 k_B T/\sigma^2$ which shows that the energies are nearly equal and cannot be distinguished inside the range of the error bars. Therefore we are unable to make a definite prediction using these results. However, we can conclude that this small energy difference will in any case produce a very strong metastable state of either a crystalline layer that is only slowly melting or a fluid layer only slowly crystallizing in the thermodynamic limit. For computer simulations this problem remains a challenge. On the other hand, if we compare the data for the (100) and (110) orientation we find quite clearly that they will not form a crystalline layer as we obtain from the surface tension $\gamma_{ws} + \gamma_{sf} = 2.63 \pm 0.27 k_B T/\sigma^2$ for the (100) orientation and $\gamma_{ws} + \gamma_{sf} = 3.08 \pm 0.27 k_B T/\sigma^2$ for the (110) orientation. Both values are much

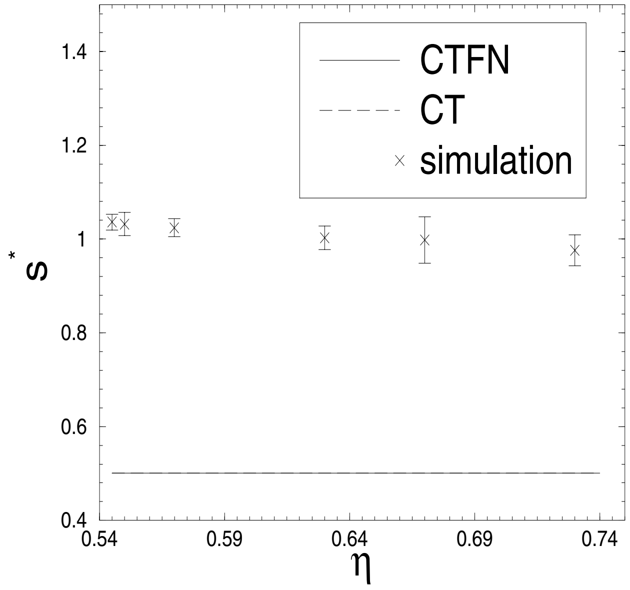

Figure 4.10: Same as Figure (4.8) but now for the reduced skewness s^*. We note that the CT (dashed line) and CTFN (solid line) fall onto the same curve.

larger than $\gamma_{wf} = 1.99 \pm 0.18 k_B T/\sigma^2$ and well outside the error bars. We therefore conclude that these orientations do not exhibit surface freezing.

Let us finally discuss some interesting open questions: It would be of interest to simulate the hard disk crystal near a hard line which we did not discuss in our present work. The problem here is that even the nature of the bulk melting transition is controversial [95, 101]. Also, for very loosely packed orientations, a facetting transition towards stable vicinal orientations [102] is expected. This should be verified for hard sphere crystals. Moreover, it would be of interest to calculate the surface free energies for the hard sphere fluid in contact with a structured wall as this is expected to lower the surface free energies. Finally the method of thermodynamic integration is also applicable to calculate surface free energies of solid-solid interfaces such as twin boundaries [103] and interfaces between different stacking sequences [104].

Chapter 5

Surface freezing of hard spheres

Freezing at interfaces or in confined geometries is an interesting phenomenon which can modify the phase bulk phase diagram or even introduce new phases [105, 106, 107, 108] which have been observed in computer simulations as well as in real experiments [109]. For the flat hard wall [89, 110, 111] have found a prefreezing transition just before the onset of the bulk freezing transition, that is a crystalline sheet forms at the wall at pressures lower than the bulk freezing pressure. In this chapter we focus on a hard sphere fluid in contact with a hard flat and structured wall. We will briefly verify the prefreezing transition of the hard sphere fluid at a flat hard wall but then focus the study on structured substrates [112]. It is expected that the structure of a substrate pattern drastically influences the nature of surface freezing. Using phenomenological theory and computer simulations of a hard sphere fluid next to a substrate formed by a periodic array of fixed spheres, we expect to find a whole range of interesting phenomena.

5.1 The model

As before we consider N hard spheres with diameter σ in a large volume V at a fixed temperature T. The number density of the spheres is $\rho = N/V$ which can be conveniently expressed in terms of the dimensionless packing fraction is $\eta = \pi\rho\sigma^3/6$. In detail, the center-of-mass positions of the spheres are denoted by $\vec{r}_i = (x_i, y_i, z_i)$ $(i = 1, \ldots, N)$. Two hard spheres i and j interact via the pair potential of Eqn. (2.1) In the following we include a surface in the hard sphere system. The presence of such a surface is described by an additional external potential which in general can model any wall pattern. In order to simplify the

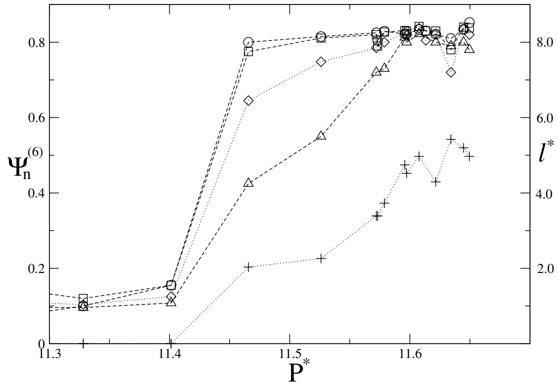

Figure 5.1: Order parameter $\Psi_n^{(6)}$ for the first four layers (from top to bottom) and the thickness of the wetting layer $\ell^* = \ell/\sigma$ (crosses) versus reduced pressure P^* for a flat wall. The system size is $L_z = 92\sigma$ and $A = 112\sigma^2$.

model this interaction is modeled as N_w fixed hard spheres interacting with the mobile ones with the potential from Eqn. (2.1) which acts on the centers of the ith hard sphere ($i = 1, \ldots, N$) and the jth wall particle $j = 1, \ldots, N_w$. The actual wall area is A and the positions of the fixed spheres on the given lattice are denoted with $\vec{r}_j^{\,w}$.

5.2 Surface freezing at flat walls

In chapter 4 we have discussed the surface free energies of a hard sphere fluid and solid in contact with a hard flat wall. We showed that for a hard sphere system it is possible to form a crystalline sheet inbetween the wall and the fluid to lower the free energy. However, the calculation of the surface free energies was unable to make a definite prediction because of the large error bars.

However, the authors of [89, 110] have performed computer simulations of a hard sphere fluid in contact with a hard wall and they could observe crystalline layers forming below the bulk freezing pressure. As finite size effects and equilibration times are particularly important for the surface freezing of hard sphere systems we will analyse this configuration again.

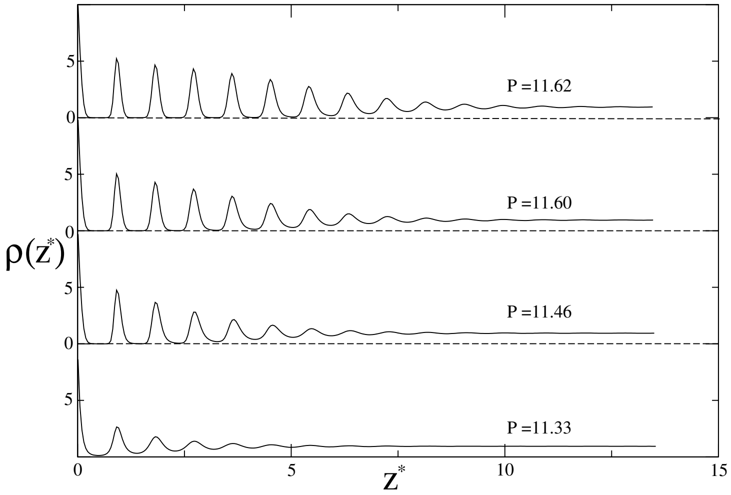

Figure 5.2: Density profile $\rho(z^*)$ versus $z^* = z/\sigma$ for four different pressures P^*. The arising of crystalline layers can be seen (bottom to top) by the low density minima. The system size is $L_z = 92\sigma$ and $A = 112\sigma^2$.

In particular we study a hard sphere system with a very large extension into the z-direction of $L_z = 92\sigma$ which is more than twice the size used by [89, 110] and corresponds to $N \approx 10000$ particles. Long equilibration times of several million *Monte-Carlo* cycles have been performed to improve equilibration.

Resulting from these simulations we indeed find a surface freezing of a hard sphere fluid at a hard flat wall. Pinpointing the exact onset of this transition is difficult because of high hysteresis effects in the simulations but in various simulations we found the onset of freezing to occur between $\eta = 0.489 \ldots 0.492$ respective at pressures $P^* = 11.15 \ldots 11.44$ which is slightly higher than the values found by [89, 110]. In Figure (5.1) we show the order parameter $\Psi_n^{(6)}$ for the first four layers. Its rise gives the onset of the surface crystallization for each layer. Moreover, in Figure (5.2) we present the density profile $\rho(z)$ for four different pressures. A frozen layer can be identified by a nearly zero minimum of the density profile.

5.3 Surface freezing at structured walls

While a flat wall induces prefreezing just before the onset of the bulk freezing transition, a much richer and more pronounced scenario of surface wetting is expected when we present a patterned surface to the hard sphere fluid system [113, 114, 115, 116, 117, 118]. In this section we therefore focus on the wall-induced surface freezing of hard sphere fluids in contact with a structured wall. However, we limit our study to periodic patterns which are commensurable or incommensurable with respect to the bulk crystal at coexistence. We do not investigate the effects of random patterns or roughness [119, 120, 121, 122] although our theory can be applied to these cases as well [123]. We show that a surface pattern plays a decisive role in determining the details of the wetting scenario by presenting different surface patterns to the system [124, 125]. In particular we choose a triangular wall pattern, a square pattern and two wall patterns forming linear rows. These different scenarios are also motivated by recent lithographic techniques [4, 8] by which chemical and topological wall patterns can be imprinted onto a substrate [12, 21, 116, 126, 127]. A profound influence on the wetting behavior of fluids on patterned substrates, similar to those reported in other recent studies [17, 18, 19, 20] was found. Furthermore, our model is actually applicable for index-matched sterically-stabilized colloidal suspensions on periodic patterned substrates which can be prepared by “glueing” colloidal spheres onto a periodic pattern [12, 21, 128, 129]. Such colloidal model systems [22] bear the further advantage that real-space experiments can be performed, as the relevant length scale is shifted from the microscopic to the mesoscopic regime.

In the following we will concentrate on a few selected wall structures which are either interesting for experiments [21, 126] or which show a generic behavior. We choose the triangular wall pattern, resulting from a cut along the (111) plane of a fcc crystal as it is intuitively the most favorable surface we can offer for a solid. This substrate pattern is shown in Figure (5.5a). It corresponds to a triangular crystal whose lattice constant $a_\triangle = 1.1075\sigma$ matches the coexisting bulk crystal. With this example we investigate in detail the effects of a strained crystal by distorting this pattern to form a rhombic crystal as well as growing and shrinking the wall pattern lattice spacing to create a lattice constant mismatch compared to the ideal bulk system.

This rhombic pattern can be derived from the ideal triangular one by squeezing the particles in x-direction and stretching them in y-direction as depicted in Figure (5.3). $a_\triangle$ is the ideal lattice spacing from the triangular pattern, $h_\triangle = \sqrt{3}/2$ and

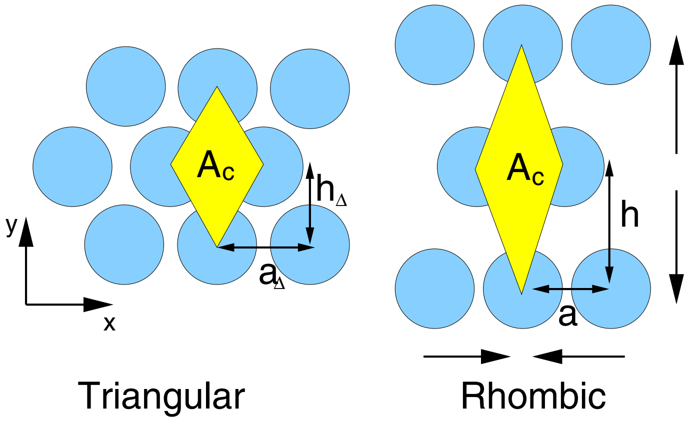

Figure 5.3: Geometry of the triangular and rhombic substrate pattern. The rhombic pattern results from the triangular one by distorting the lattice as indicated by the arrows such that the area A_c of the unit cell remains constant.

a and h are the lattice spacing of the distorted wall pattern in x respectively y-direction. This leads to strain tensor components $\epsilon_x = (a - a_\triangle)/a_\triangle$ and $\epsilon_y = (h - h_\triangle)/h_\triangle$ with all other components being zero. For our analysis we restrict ourselves to systems where the surface area $A_c = A_\triangle$ of the original and the distorted unit cell at the wall is constant. The advantage of doing so is that this strain leads to a simplified form of the elastic energy as we obtain

$$A_\triangle \equiv a_\triangle h_\triangle = a_\triangle(1+\epsilon_x)h_\triangle(1+\epsilon_y) \equiv A_c \,. \tag{5.1}$$

Eqn. (5.1) gives a relationship between the two strain tensor components ϵ_x and ϵ_y which allows one to define the distortion with only one dimensionless strain parameter

$$\epsilon = \sqrt{\left(\frac{a-a_\triangle}{a_\triangle}\right)^2 + \left(\frac{h-h_\triangle}{h_\triangle}\right)^2} \,. \tag{5.2}$$

Furthermore we study the effects of a lattice constant mismatch within this example. This is done by assuming an unit cell which is shrunken or grown in comparison to the ideal one by a relative distortion which is equal in x and y-direction, see Figure (5.4). Although not keeping the surface area constant, we can again define the distortion by just one dimensionless strain parameter

$$\epsilon = \sqrt{2}\frac{a-a_\triangle}{a_\triangle} = \sqrt{2}\frac{h-h_\triangle}{h_\triangle} \,. \tag{5.3}$$

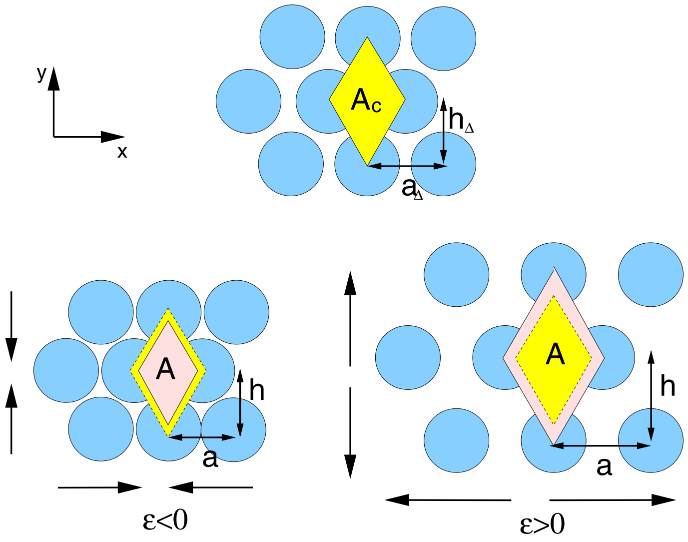

Figure 5.4: Geometry of the triangular substrate pattern which is shrunken ($\epsilon < 0$) or grown ($\epsilon > 0$) compared to the lattice defined by the coexisting bulk crystal.

Another type of wall pattern which we investigate is a square wall pattern which is generated by cutting a fcc crystal along the (100) plane as depicted in Figure (5.5b). This results in a square lattice of fixed spheres. We consider that the lattice constant $a_\square = 1.1075\sigma$ exactly matches the coexisting bulk crystal but again include the effects of a slight lattice constant mismatch within this example, as this is of particular experimental interest. In the same way as in Eqn. (5.3) we define the relative distortion which shall be equal in x and y-direction as

$$\epsilon = \sqrt{2}\frac{a - a_\square}{a_\square} = \sqrt{2}\frac{h - h_\square}{h_\square} . \tag{5.4}$$

Furthermore, we investigate a pattern made out of linear rows by cutting a hexagonal-close-packed (hcp) as well as a fcc crystal along the (110) plane as shown in Figure (5.5c) and Figure (5.5d). We again exactly match the lattice constants to the coexisting bulk crystal. This leads to wall patterns which are quite tightly packed particles in one direction with a separation of $h = 1.1075\sigma$ forming one dimensional rows. These rows represent a zig-zag structure relative to each other, the spacing in the other direction is $a = \sqrt{3}a_\triangle$ for the hcp (110) and $a = \sqrt{2}a_\triangle$ for the fcc (110) pattern, see Figure (5.5c) and Figure (5.5d). These substrate patterns are interesting from an experimental point of view [130].

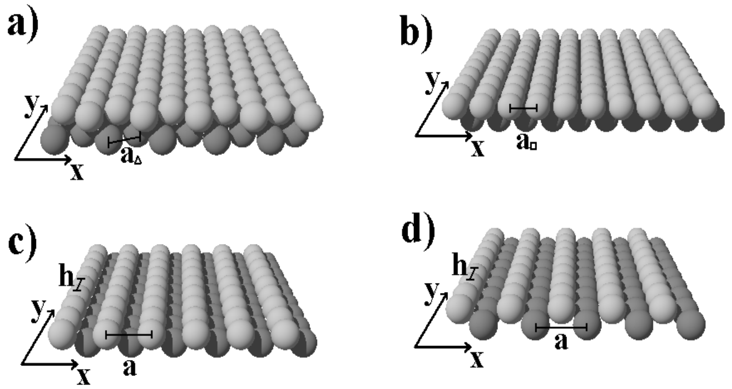

Figure 5.5: Sketch of different wall patterns: a) fcc (111) (triangular) wall pattern with lattice constant $a_\triangle = 1.1075\sigma$. b) fcc (100) (square) wall pattern with lattice constant $a_\square = 1.1075\sigma$. c) fcc (110) wall pattern with lattice constants $h = 1.1075\sigma$ and $a = \sqrt{3}h$. d) hcp (110) zig-zag wall pattern with lattice constants $h = 1.1075\sigma$ and $a = \sqrt{2}h$.

5.4 Phenomenological theory

Let us now describe a phenomenological theory for wetting by a crystalline layer. The key quantity of any wetting theory [1] is the difference Σ of the grand canonical free energies per unit area for a wetting and a non-wetting situation. This quantity is discussed as a function of the thermodynamic and system parameters and the width ℓ of the adjacent solid sheet. Minimizing Σ with respect to ℓ yields the equilibrium profile provided the quantity Σ evaluated at its minimum is negative. There are several contributions to the total free energy Σ resulting from bulk and surface thermodynamics as well as effective interface interactions and additional free energy contributions resulting from elastic distortions of the solid [131]. Therefore Σ splits into three terms,

$$\Sigma = \Sigma_1 + \Sigma_2 + \Sigma_3 \tag{5.5}$$

which we will subsequently discuss.

5.4.1 Bulk thermodynamics and elastic free energy

Near bulk fluid-solid coexistence, an expansion of the energy around coexistence yields both the bulk thermodynamics and the elastic energy. We assume that the adjacent crystalline layers pick up exactly the structure of the wall pattern and exhibit no spontaneous shearing. This causes a strain ϵ if the wall pattern is incommensurate with the coexisting bulk crystal [132], which in turn gives rise to a free energy penalty due to the wall-induced elastic distortion of the solid. Harmonic elasticity theory [133] can be used to calculate the penalty Σ_1 by an expansion of the grand potential per area around the coexisting bulk crystal:

$$\begin{aligned}\Sigma_1/\ell &= f_s(\rho_s) + f_s'(\rho_s)(\rho-\rho_s) + \frac{C_{11}}{2}(\epsilon_x^2+\epsilon_y^2+\epsilon_z^2)\\ &+ C_{12}(\epsilon_x\epsilon_y+\epsilon_y\epsilon_z+\epsilon_z\epsilon_x) - \mu\rho + P \qquad (5.6)\end{aligned}$$

where ρ is the mean density of the solid which has to be minimized, μ is the given chemical potential, P is the bulk equilibrium fluid pressure, $f_s(\rho)$ is the *Helmholtz* free energy per volume of the solid, ϵ_x,ϵ_y,ϵ_z are the relative strains in direction x, y, z, and C_{ij} are the bulk elastic constants of the fcc solid at coexistence. For a hard sphere fcc crystal these elastic constants have been determined by computer simulation [134]. As the density is directly dependent on the elastic distortions we can write $\rho = \rho_s(1-\epsilon_x-\epsilon_y-\epsilon_z)$ and take ϵ_z rather than ρ as the variation parameter with ϵ_x and ϵ_y fixed by the wall pattern. Furthermore we use the relations

$$\mu_c = \left.\frac{\partial f_s(\rho)}{\partial\rho}\right|_{\rho=\rho_s} = f_s'(\rho_s) \quad\text{and}\quad P_c = -f_s(\rho_s) + \mu_c\rho_s \qquad (5.7)$$

with μ_c, P_c denoting the chemical potential and the bulk pressure at coexistence. Defining $\Delta P = P_c - P > 0$ and $\Delta\mu = \mu_c - \mu$ we obtain

$$\begin{aligned}\Sigma_1/\ell &= -\Delta P + \Delta\mu\rho_s - \Delta\mu\rho_s(\epsilon_x+\epsilon_y+\epsilon_z)\\ &+ \frac{C_{11}}{2}(\epsilon_x^2+\epsilon_y^2+\epsilon_z^2) + C_{12}(\epsilon_x\epsilon_y+\epsilon_y\epsilon_z+\epsilon_z\epsilon_x)\,. \qquad (5.8)\end{aligned}$$

Minimizing with respect to ϵ_z yields $\epsilon_z = \Delta\mu\rho_s/C_{11} - (\epsilon_x+\epsilon_y)C_{12}/C_{11}$. Inserting this into Eqn. (5.8), the bulk thermodynamics and elastic energy contribution becomes

$$\begin{aligned}\Sigma_1/\ell &= -\Delta P + \mu\rho_s - (\epsilon_x+\epsilon_y)\Delta\mu\rho_s\frac{C_{11}-C_{12}}{C_{11}}\\ &+ (\epsilon_x^2+\epsilon_y^2)\frac{C_{11}^2-C_{12}^2}{2C_{11}} + \epsilon_x\epsilon_y\frac{C_{12}C_{11}-C_{12}^2}{C_{11}} - \frac{(\Delta\mu\rho_s)^2}{2C_{11}}\,. \qquad (5.9)\end{aligned}$$

Using thermodynamical relations and the hard sphere equation of state we can approximate Eqn. (5.9) to second order in ϵ_x^2,ϵ_y^2 and $(\Delta P)^2$. We introduce the density ratio $\tilde{\alpha} = \rho_s/\rho_f = 1.103$ and $\alpha = 1-\tilde{\alpha} = 0.103$ the relative density jump across bulk freezing. From the *Carnahan-Starling* hard sphere equation of state [65], we obtain

$$\kappa = \rho_f^{-1} / \left. \frac{\partial P}{\partial \rho} \right|_{\rho=\rho_f} = 0.020\sigma^3/(k_B T) \,. \tag{5.10}$$

Using these abbreviations, we can substitute $\Delta\mu$ via ΔP near the coexistence via

$$\frac{\Delta\mu}{\Delta P} \approx \frac{\partial\mu}{\partial P} \approx \frac{1}{\rho_f}\left(1 - \frac{\Delta\rho}{\rho_f}\right) , \tag{5.11}$$

with $\Delta\rho$ being the density difference of the fluid phase to coexistence. As near coexistence we can also write

$$\frac{\Delta\rho}{\Delta P} \approx \frac{1}{\frac{\partial P}{\partial\rho}} = \kappa\rho_f \tag{5.12}$$

we obtain combining Eqn. (5.11) and Eqn. (5.12) an approximate relationship for $\Delta\mu$ as

$$\Delta\mu = \frac{\Delta P\tilde{\alpha}}{\rho_s} + \frac{(\Delta P)^2\tilde{\alpha}\kappa}{\rho_s} \,. \tag{5.13}$$

This can be inserted into Eqn. (5.9) and yields terms of second order.

For the rhombic case, with $\epsilon_x = \epsilon/\sqrt{2}$, $\epsilon_y = -\epsilon/\sqrt{2}$ we obtain using this procedure

$$\begin{aligned} \Sigma_1 &= \alpha\Delta P\ell + \left(\kappa - \frac{\tilde{\alpha}^2}{2C_{11}}\right)(\Delta P)^2\ell \\ &+ \beta_r\epsilon^2\ell + O\left(\epsilon^3, \epsilon^2\Delta P, \epsilon(\Delta P)^2, (\Delta P)^3\right) \end{aligned} \tag{5.14}$$

where $\beta_r = (C_{11} - C_{12})/2 = 24.43k_BT/\sigma^3$.

For the lattice constant mismatch case, on the other hand, we use $\epsilon_x = \epsilon/\sqrt{2}$, $\epsilon_y = \epsilon/\sqrt{2}$ and insert it into Eqn. (5.9). This yields

$$\begin{aligned} \Sigma_1 &= \alpha\Delta P\ell + \left(\kappa - \frac{\tilde{\alpha}^2}{2C_{11}}\right)(\Delta P)^2\ell \\ &+ \beta_m\epsilon^2\ell - \tilde{\alpha}\beta^*\Delta P\epsilon\ell + O\left(\epsilon^3, \epsilon^2\Delta P, \epsilon(\Delta P)^2, (\Delta P)^3\right) \end{aligned} \tag{5.15}$$

with the coefficients $\beta_m = \left(C_{11} + C_{12} - 2C_{12}^2/C_{11}\right)/2 = 38.23k_BT/\sigma^3$ and $\beta^* = \sqrt{2}\left(C_{11} - C_{12}\right)/C_{11} = 1.03$. Note that there is a mixed term proportional to $\Delta P\epsilon$ which vanishes for the rhombic case due to area conservation.

5.4.2 Surface thermodynamics

The next leading thermodynamic term in an expansion for large ℓ involves interfacial free energies

$$\Sigma_2 = \gamma_{ws} + \gamma_{sf} - \gamma_{wf} \, . \tag{5.16}$$

Here, three interfacial free energies extrapolated to coexistence occur: these are tensions between the patterned wall and the solid (γ_{ws}), between the patterned wall and the fluid (γ_{wf}) and between the bulk solid and fluid (γ_{sf}). A necessary condition for complete wetting to occur is

$$\gamma_{ws} + \gamma_{sf} \geq \gamma_{wf} \, . \tag{5.17}$$

Note that in our calculation we use *extrapolated* interfacial free energies and therefore Eqn. (5.17) is an extension of *Antonow's* rule to an inequality. We remark that γ_{ws} and γ_{wf} depend on the wall pattern [131] while γ_{sf} only depends on the relative orientation of the planar solid surface with respect to the fluid. However, in contrast to the author of [131] in our scenario the wall pattern is fixed and immobile. A possible dependency of the interfacial energies does not enter the minimization of the free energy. Although γ_{ws} and γ_{wf} can in principle be calculated using the methods of chapter 4 we need not do so as they only enter as constant terms into Eqn. (5.5) and drop out after the minimization of the energy. We remark that γ_{sf} has recently been calculated for hard spheres by computer simulation for different orientations [135].

5.4.3 Effective interface potential

The next leading contribution is the effective interface interaction Σ_3 between the wall-solid and the solid-fluid interface as a function of their average distance ℓ. This quantity can be derived from microscopic density functional theory by minimizing the functional with respect to a constraint of fixed width ℓ [83].

For large widths ℓ, as we are dealing with short-ranged interparticle interactions, the asymptotic behavior of $\Sigma_3(\ell)$ is

$$\Sigma_3 = \gamma_0 e^{-\ell/\ell_0} \tag{5.18}$$

where γ_0 is a positive prefactor implying that the interaction is repulsive and ℓ_0 is a correlation length in the bulk solid at fluid coexistence.

More subtle information is contained in $\Sigma_3(\ell)$ for smaller ℓ. First, if $\Sigma_3(\ell)$ is monotonically decreasing with ℓ there is complete wetting provided the relation

(5.17) is fulfilled. Second, non-monotonic behavior with a minimum of $\Sigma_3(\ell)$ at $\ell = \ell^*$ leads to incomplete wetting with a finite width of ℓ^* at coexistence. Finally, if $\Sigma_3(\ell)$ exhibits oscillations on the scale of the molecular layer widths, wetting may proceed via a finite or infinite cascade of layering transitions [136, 137].

5.4.4 Prediction of scaling laws

In summary, our theory works for small ΔP, small ϵ and large ℓ. We further assume that the parameters γ_0 and ℓ_0 characterizing the asymptotic form of the effective interface potential $\Sigma_3(\ell)$ are not affected by the small distortion ϵ. We further note that the phenomenological approach does not predict whether complete wetting occurs as it does not fix the sign of $\gamma_{ws} + \gamma_{sf} - \gamma_{wf}$. This requires a full microscopic calculation. However, putting Eqn. (5.5) to Eqn. (5.18) together and minimizing Σ with respect to ℓ one finds the following quite general scaling relations which no longer depend on the interfacial free energies γ_{ws}, γ_{sf} and γ_{wf}. The asymptotic relations are valid close to coexistence:

i) For vanishing ϵ, the thickness ℓ diverges logarithmically with ΔP,

$$\ell = -\ell_0 \ln\left(\frac{\ell_0 \alpha \Delta P}{\gamma_0}\right) \tag{5.19}$$

provided there is complete wetting.

ii) Again assuming that there is complete wetting for $\epsilon = 0$. Then, for $\epsilon \neq 0$, there is incomplete wetting and the *maximal* thickness which is achieved at $\Delta P = 0$ varies logarithmically with ϵ:

$$\ell = -\ell_0 \ln\left(\frac{\beta \ell_0 \epsilon^2}{\gamma_0}\right), \tag{5.20}$$

with $\beta = \beta_r$ or respectively $\beta = \beta_m$.

iii) For an area conserving, for example the rhombic case: If there are layering transition, these transitions occur when

$$\alpha \Delta P = \frac{\gamma_0}{\ell_0} e^{-n a_z/\ell_0} - \beta_r \epsilon^2, \tag{5.21}$$

where a_z is the layer spacing in z-direction. In detail, $a_z = \sqrt{2/3}a_\triangle$ for a triangular wall pattern and $a_z = \sqrt{2}/2a_\triangle$ for a square wall pattern. Eqn. (5.21) shows that in the plane spanned by ΔP and ϵ^2, the transition lines are linear. The slope is predicted to be the very general ratio α/β_r which can be tested against simulations. Note that a linear relation with a slope α/β_r is valid both for wetting and incomplete wetting at $\epsilon = 0$.

iv) For a stretched or shrunken lattice the surface freezing of the nth layer at fixed ΔP at a distortion ϵ is determined by the quadratic form

$$\alpha \Delta P - \tilde{\alpha} \Delta P \epsilon = \frac{\gamma_0}{\ell_0} e^{-n a_z / \ell_0} - \beta_m \epsilon^2 \,. \tag{5.22}$$

Eqn. (5.22) shows that in the plane spanned by ΔP and ϵ, the transition lines are parabolic with their apices laying on the straight line $\epsilon(\Delta P) = \beta^*/(2\beta_m)\Delta P$. The lowest possible prefreezing pressure is

$$\Delta P_{\min} = \frac{2\beta_m \alpha - 2\sqrt{\beta_m^2 \alpha^2 + (\beta^*)^2 \beta_m \alpha \Delta P_n}}{(\beta^*)^2} \,, \tag{5.23}$$

with ΔP_n being the prefreezing pressure of the undistorted nth layer as obtained by inverting Eqn. (5.19) or by computer simulations. Note the interesting fact that a slightly expanded lattice will have a *lower* prefreezing pressure than the ideal matching lattice. However, it will not show complete wetting.

5.5 Simulation technique

We simulate the hard sphere fluid using a rectangular simulation box of size $V = L_x L_y L_z$ with periodic boundary conditions in x and y-direction. In z-direction the system is confined by two patterned walls at distance L_z. The surface area of the simulation box under consideration is $A = L_x L_y$. Onto these walls any pattern can be imprinted as described in section 5.1. We use standard *NVT Monte-Carlo* simulation techniques as described in section 3.2. with system sizes of about $N = 640$ to $N = 10400$ particles yielding surface areas of about $A = 16\sigma^2$ to $A = 271\sigma^2$ and an extension into the z-direction of about $L_z = 40\sigma$ to $L_z = 100\sigma$ have been used during our simulations. In order to avoid lateral compressional strains in the crystal, the length L_x and L_y were adjusted to the given crystallographic orientation such that a laterally periodic bulk crystal fits exactly into the simulation box.

In Figure (5.6) we show a typical snapshot of a computer simulation, where a hard sphere fluid is in contact with a triangular wall pattern. The system shows the prefreezing of the first few layers and inherits the structure of the triangular wall pattern.

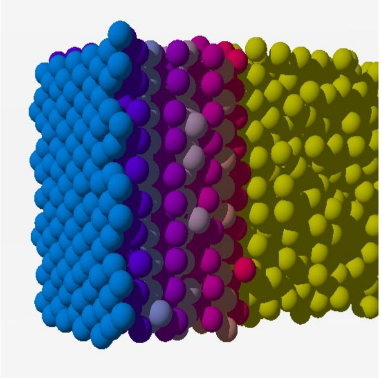

Figure 5.6: Snapshot at $\eta = 0.490$ respectively $P^* = 11.25$ for a triangular wall. The first few layers are marked with different colors to show their frozen nature (left) while toward the bulk (right) the system becomes fully fluid. On the front area of the first layer the system mimics the triangular wall pattern which is not shown for the sake of clarity.

5.6 Analysis of finite system size

As described in section 3.3 particular attention has to be paid to finite size effects in the system under consideration. In both, the length in z-direction as well as in the area $A = L_x L_y$ finite size effects could affect the results. We use the system with the commensurate triangular wall pattern to investigate these finite size effects in more detail.

We mentioned the importance of finite size effects in section 3.3 to avoid finite size effects such as capillary condensation. Therefore we check our simulations results with box lengths ranging from $L_z = 40\sigma$ to $L_z = 100\sigma$ and can confirm no finite size dependency above the statistical uncertainties. Especially, we conclude that we are no affected by capillary effects which have been shown by [138] to occur in the system close to bulk freezing for box length below $30 - 40\sigma$ but become negligible for greater box length as well as for being farther away from the bulk freezing point.

Yet more important is the finite size effect of the surface area A. Hence we made a careful analysis of surface areas between $A = L_x L_y = 16\sigma^2$ and $A = L_x L_y = 271\sigma^2$. As depicted in Figure (5.7) we find a size dependency for small surface areas. Only around $100\sigma^2$ the curves begin to approach asymptotic values. Explicit data for this are collected in Table 5.1. We also extract the average value for the freezing densities for the triangular wall from the data of Figure (5.7)

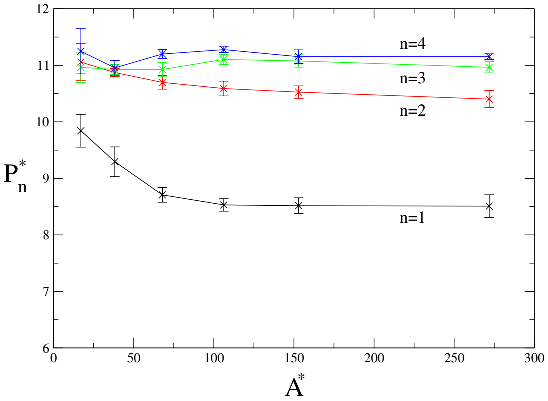

Figure 5.7: The transition pressure P_n^* in different layers $n = 1, 2, 3, 4$ versus surface area for a triangular wall pattern. The pressure saturates for all layers at about $A \approx 100\sigma^2$.

respectively Table 5.1 for values of $A > 100\sigma^2$. This gives rise to the statistical errors which are also presented in this table.

From the finite size analysis in z-direction and A area we find that systems of around $L_z = 45\sigma$ and areas of $A = 106\sigma^2$ are sufficient. Our further studies are based on systems with such a size.

5.7 Results

5.7.1 Triangular (fcc (111)) and rhombic wall pattern

The most favorable wall pattern which we can offer the system is a triangular pattern with a lattice spacing which exactly matches the bulk crystal at bulk melting [139, 140]. We use this configuration as a reference point for the investigation of wall patterns.

Performing simulations on such systems yields complete wetting by crystalline layers starting at very low bulk pressures of $P^* = 8.53$ (corresponding to a packing fraction of $\eta = 0.457$) well below bulk freezing. From this pressure onwards we find a cascade of layered freezing transitions whose pressures are summarized in Table 5.1.

A/σ^2	layer 1	layer 2	layer 3	layer 4
17.0	9.84	11.06	10.96	11.25
38.2	9.30	10.87	10.93	10.96
67.9	8.71	10.70	10.93	11.20
106.2	8.53	10.60	11.10	11.28
152.9	8.52	10.53	11.08	11.15
271.9	8.51	10.40	10.97	11.15
average	8.53 ± 0.13	10.51 ± 0.12	11.05 ± 0.11	11.20 ± 0.05

Table 5.1: Freezing pressures P^* for the first four layers of a triangular wall pattern for various surface areas A. The average is formed from the data $A > 100\sigma^2$ which does not exhibit finite size effects anymore.

The fact that the wetting proceeds layer-by-layer is a subtle effect. For instance, in sedimentation profiles [141] the contrary, namely a continuous growth, as a function of the gravitational constant was found. The layerwise freezing transitions in our system can be understood intuitively as follows: when the first layer freezes at the pressure P_1^*, the spheres become much more localized reflecting the triangular pattern. These frozen layers then act as template for freezing of the second layer at P_2^*. P_2^* is larger than P_1^* as the spheres in the first layer are still mobile. This is repeated for the third layer and so on forming a whole cascade of layering transitions.

As predicted by asymptotic theory, complete wetting is achieved by a logarithmic growth of the wetting layer $\ell \propto -\ln \Delta P^*$ as shown in Figure (5.8). Here we show the prefreezing as found with the order parameter Φ_n. Except for the first layer, which is not expected to follow a logarithmic growth law as the theory is only valid for large ℓ, we find a good agreement with a logarithmic growth of the wetting layer. Although we only have data for a limited range of layer thicknesses as shown in Figure (5.8) the fact that the logarithmic growth law is fulfilled very well gives strong evidence that the wetting is really complete, that is every layer is frozen for $P \to P_c$.

From a fit of the data from Figure (5.8) we can extract the two parameters γ_0 and ℓ_0 which we used in the phenomenological theory, see Eqn. (5.18). The actual numbers for the correlation length is $\ell_0 = 2.50\sigma$ and the amplitude is $\gamma_0 = 0.47 k_B T/\sigma^2$.

Moreover, we verify the *Lindemann* melting rule for surface freezing. The traditional *Lindemann* melting rule [78] states that a bulk solid melts if the *Lin-*

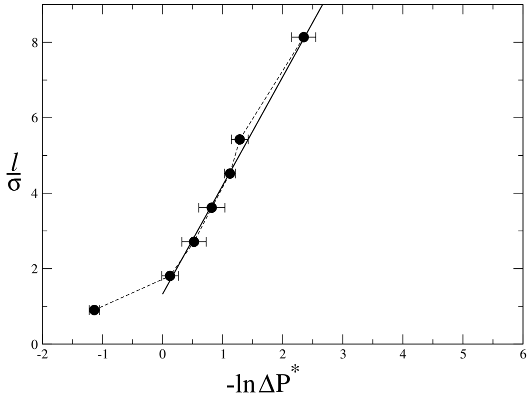

Figure 5.8: The thickness of the crystalline wetting layer ℓ versus $-\ln \Delta P^*$ as measured by the order parameters Φ_n. The straight line is the best linear fit to the data excluding the first layer.

demann parameter L as given by Eqn. (3.27) is roughly about 10%. For the analysis of surface freezing we define this parameter now layer per layer, that is we apply Eqn. (3.27) to the nth layer yielding the layerwise *Lindemann* parameter L_n.

In Figure (5.9) we present simulation data for L_n for the first four layers of the triangular wall pattern. First, it can be seen that L_n varies very slowly with the pressure thus providing not a sharp diagnostics for interfacial freezing. If the interfacial freezing is fixed by the clearcut diagnostics of Φ_n, however, then one can check how large L_n is at interfacial melting. Indeed L_n at melting varies from 0.18 for the first layer to 0.14 for the fourth layer but is close to the bulk value of 0.13 [78] as presented by a dashed line in Figure (5.9). This implies that the rough *Lindemann* melting rule does also apply for interfacial freezing.

We now distort the triangular wall pattern to create a rhombic pattern with $\epsilon > 0$, see Eqn. (5.2). The maximal distortion is given for two spheres touching and occurs at $\epsilon^2 \to \epsilon_m^2 \equiv 0.021$. At this point the cost in free energy due to the lateral distortion diverges. As the theory considers only harmonic distortions, any higher order effects and especially this divergence are not accounted for. Computer simulations prove this behavior. We obtain for a rhombic distortion again a wetting by a cascade of crystalline layers but at shifted freezing pressure. The actual data are collected in Table 5.2.

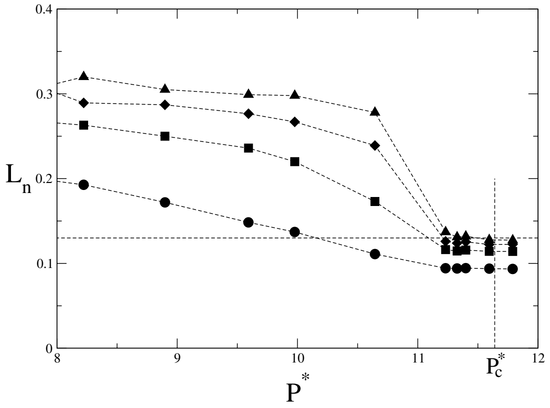

Figure 5.9: The *Lindemann* parameter L_n for the first four layers (from bottom to top) for a triangular wall pattern. The horizontal dashed line indicating the bulk freezing *Lindemann* parameter and the vertical dashed line indicating the bulk freezing pressure P_c^*.

Putting the parameters γ_0 and ℓ_0 into Eqn. (5.20) and Eqn. (5.21) we can verify the two other theoretical predictions. We show the results in Figure (5.10). The inset of Figure (5.10) shows our simulation data using a log-linear plot for Eqn. (5.20) where indeed we find qualitative agreement. However the uncertainty of the data is large since the measured thickness of the layer is actually a multiple of the layer spacing $a_z = \sqrt{2/3}a_\triangle$ in the z-direction. Note that the solid line in the inset of Figure (5.10) involves no fit parameters as these are fixed by the fit as shown in Figure (5.8).

Furthermore, the layering transition of the nth layer can be estimated by the theory to occur according to Eqn. (5.21). In the plane spanned by ΔP and ϵ^2, these transition lines are predicted to be linear. In fact, as shown in Figure (5.10), most of our computer simulation data for the layering transitions fall upon straight lines. We emphasize that the slope does not involve any fit parameter, therefore quantitative agreement between theory and simulation is obtained within the error bars of the simulation data.

However, there are deviations for large strains which we attribute to anharmonic elasticity. In fact, when $\epsilon^2 \to \epsilon_m^2 \equiv 0.021$, the divergence in free energy is not accounted for in the theory. Furthermore the logarithmic growth law does not hold for the very first layer as it is derived asymptotically only for large ℓ.

ϵ^2	a/σ	layer 1	layer 2	layer 3	layer 4	layer 5
0.0	1.108	8.53	10.51	11.05	11.20	11.32
0.0009	1.063	8.65	10.73	11.20	11.38	11.52
0.0022	1.072	9.26	11.19	11.64	—	—
0.0036	1.085	9.53	11.23	—	—	—
0.0050	1.054	9.96	11.64	—	—	—
0.0079	1.040	10.89	—	—	—	—
0.0092	1.035	11.15	—	—	—	—
0.0115	1.027	—	—	—	—	—
0.0143	1.018	—	—	—	—	—
0.0190	1.005	—	—	—	—	—

Table 5.2: Prefreezing pressures P^* of the first five layers for a triangular wall pattern which is distorted to a rhombic one by a distortion ϵ^2.

As we did not include the data for the first layer into the linear fit, this leads us to adjust the offset of the theoretical lines in Figure (5.10) for the first two layers to the actual measured data from the computer simulation. However the slope of these lines is still in agreement with the theory as the theory is quite robust to the exact form of the effective interface potential $\Sigma_3(\ell)$. We emphasize that all other layers do not need any additional fit parameter. Slope and offset are given by the theoretical prediction of the phenomenological theory.

A further notable fact drawn from Figure (5.10) is that there is no surface freezing at all if ϵ exceeds a critical value ϵ_c. The theory predicts $\epsilon_c^2 = 0.014$ while the simulations yield a smaller value, $\epsilon_c^2 = 0.011 \pm 0.001$ due to the anharmonic elastic free energy. For $\epsilon_c^2 < \epsilon^2 < \epsilon_m^2 = 0.021$ the large free energy cost of elastic distortion prevents the system from surface freezing. The actual situation is a strongly inhomogeneous fluid reflecting the surface pattern which remains stable up to the bulk freezing point. However, it is possible that in real systems the system can still freeze but introduce crystal defects to reduce the high stress applied to it. We have not included any effects of defects in our work [142].

As discussed within the framework of the phenomenological wetting theory we investigated the effect of a lattice constant mismatch for the triangular lattice. This results in a growing or shrinking of the wall pattern compared to the ideal one. In Figure (5.11) we plot the theoretical prediction of the resulting prefreezing pressures versus the distortion ϵ, see Eqn. (5.3) and Eqn. (5.15) and compare it with the computer simulation data as summarized in Table 5.3. There is a good

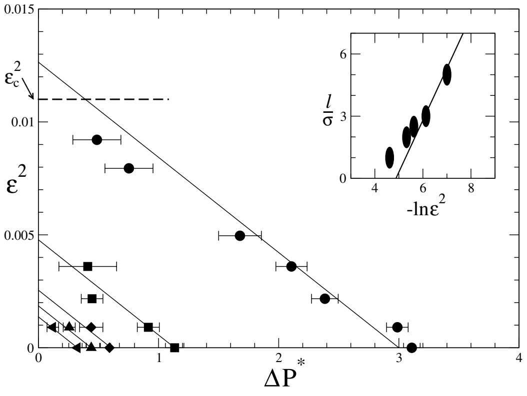

Figure 5.10: Location of the first five layering transitions in the plane spanned by ΔP^* and ϵ^2. The symbols represent simulation data with their statistical error. The straight lines are the theoretical predictions. The simulation result for ϵ_c^2 is indicated by the dashed line. The inset shows the maximal thickness ℓ versus $-\ln\epsilon^2$. The straight line is the theoretical prediction, see Eqn. (5.21). Symbols represent simulation data with the size of the symbols marking the error.

agreement between the computer simulation data and the theoretical prediction. For the first layer, there are deviations which we attribute to the non-quadratic corrections in the thermodynamical part of the theory.

For $\epsilon = 0$ there is complete wetting by crystal. When increasing or decreasing ϵ a crystalline sheet of prefrozen layers still exists. However, the shrinking or growing of the pattern leads to a shift in the onset of the freezing density as well as to a reduction of the maximal achieved thickness of the wetting layer. No complete wetting is possible anymore. Comparing this situation with the rhombic distortion we find that the onset of prefreezing no longer follows a pure quadratic ϵ^2 behavior. The additional expansion or shrinking of the crystal leads to a linear term in $\epsilon\Delta P$ which shifts the wetting curves. For a slightly stretched crystal with $\epsilon > 0$, the pressure for which there still exists surface freezing is now shifted to *lower* values compared to the ideal matching substrate pattern with $\epsilon = 0$. We note though that there is no complete wetting anymore if $\epsilon \neq 0$. The theoretical critical distortion above which there is no surface freezing at all is $\epsilon_c = 0.10$. There is no maximal distortion for a grown lattice and a maximal distortion of

ϵ	layer 1	layer 2	layer 3	layer 4
-0.061	10.80 ± 0.4	—	—	—
-0.044	10.25 ± 0.4	11.63 ± 0.03	—	—
-0.030	9.70 ± 0.12	11.10 ± 0.05	11.63 ± 0.03	—
-0.022	9.65 ± 0.15	10.96 ± 0.05	11.52 ± 0.02	11.57 ± 0.01
0.000	8.53 ± 0.12	10.51 ± 0.07	11.05 ± 0.05	11.20 ± 0.04
0.012	8.45 ± 0.08	10.53 ± 0.08	11.13 ± 0.01	11.59 ± 0.04
0.025	8.28 ± 0.21	10.46 ± 0.16	11.42 ± 0.025	—
0.045	8.46 ± 0.22	10.81 ± 0.09	—	—
0.054	9.09 ± 0.35	11.62 ± 0.08	—	—
0.067	8.95 ± 0.33	—	—	—
0.080	10.14 ± 0.27	—	—	—
0.093	11.57 ± 0.07	—	—	—

Table 5.3: Freezing pressures P^* for the first four layers of a triangular wall pattern with lattice constant mismatch ϵ.

$|\epsilon_m| = 0.14$ for a shrunken lattice. The lowest possible prefreezing pressure is $P^* = 8.16$ as predicted by the theory and $P^* = 8.28 \pm 0.21$ as found in the computer simulations.

5.7.2 Hard sphere fluid near a fcc (100) wall

We continue the analysis with a square wall pattern which is a cut through a (100) plane of a fcc crystal as shown in Figure (5.5)b. In contrast to the results of the triangular wall we do not find complete wetting in this case not even for the ideal lattice spacing. This can be concluded from Figure (5.12) where the growth of the wetting layer seems to saturate at around $\ell_m = 3.9\sigma$ leading to incomplete wetting by the crystal. However, approaching coexistence further possesses enormous equilibration problems in the simulations. However, the decreasing slope in the ℓ/σ versus $-\ln \Delta P^*$ plot seems to indicate incomplete wetting.

As discussed within the framework of the phenomenological wetting theory we also investigated the effect of a lattice constant mismatch for the square lattice. This results in a growing or shrinking of the wall pattern compared to the ideal one.

In Figure (5.13), the theoretical prediction and computer simulation data of the resulting prefreezing pressures versus the distortion ϵ are plotted, see Eqn.

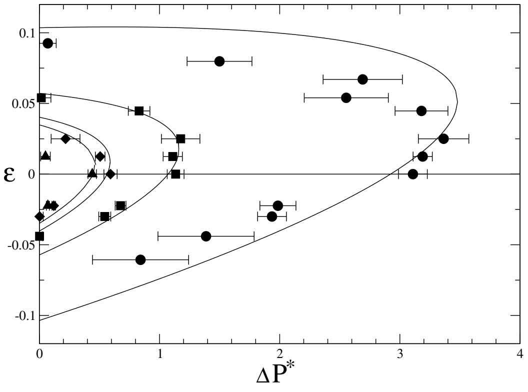

Figure 5.11: Location of the first four layering transitions in the plane spanned by ΔP^* and ϵ. The curves are the theoretical predictions for a crystal lattice constant which is shrunk ($\epsilon < 0$) or grown ($\epsilon > 0$) compared to the coexisting bulk crystal. The different symbols show computer simulation results for the crystallization transitions in the different layers with their error bars.

(5.4) and Eqn. (5.15). We start at $\epsilon = 0$ with the prefreezing pressures as found in the computer simulation and shown in Figure (5.12) and extend these points by the data as obtained by Eqn. (5.21).

For $\epsilon = 0$ we have incomplete wetting by a few prefrozen layers. When increasing ϵ a crystalline sheet of prefrozen layers still exists. However, the shrinking or growing of the pattern leads to a shift in the onset of the freezing density as well as to a reduction of the maximal achieved thickness of the wetting layer similar to the one detected for the triangular lattice. In fact, the theoretical critical distortion is $\epsilon_c = 0.09$ while there is no maximal distortion for a grown lattice and a maximal distortion of $|\epsilon_m| = 0.14$ for a shrunken lattice. The theoretical value for the lowest prefreezing pressure is $P^* = 8.92$ which is higher than that for the corresponding (111) case but lower than the prefreezing pressure of the undistorted (100) crystal.

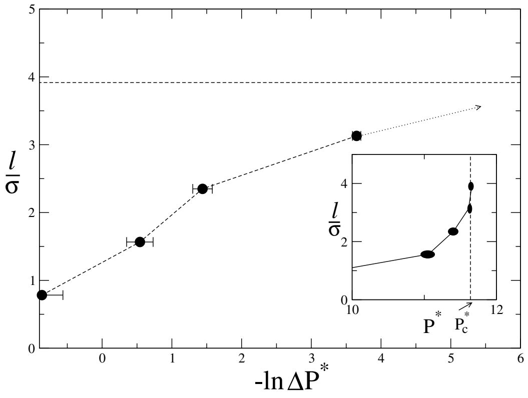

Figure 5.12: Thickness ℓ of the wetting layer versus $-\ln \Delta P^*$. as measured with the order parameters $\Psi_n^{(4)}$. The thickness seems to converge toward 3.9σ as shown in the inset where the thickness ℓ is plotted versus P^*.

5.7.3 Hard sphere fluid near a fcc (110) wall

We now focus our analysis on a wall pattern which is a cut through the (110) plane of a fcc crystal as shown in Figure (5.5)c. To analyse this system we mainly apply the $\Psi_n^{(2)}$ order parameter. As this order parameter only indicates a one dimensional ordered system which is not necessarily two dimensional ordered we compare the data with the order parameter as obtained by the minima of the density profile. We find good agreement in locating surface freezing by the two different order parameters.

Similar to the square lattice we find incomplete wetting by the crystal. The crystallization proceeds via discrete layering but stops at $P^* \to P_c^*$. The width of the wetting layer converges toward a maximum thickness of about $\ell_m = 5.5\sigma$ when approaching the bulk freezing point. Again, the deviation from a logarithmic growth law is small so that there is still some uncertainty in this prediction.

5.7.4 Hard sphere fluid near a hcp (110) wall

Using the $\Psi_n^{(2)}$ order parameter for the hcp (110) wall, we find surface freezing starting at very low values of $P^* = 9.5$ leading to complete wetting by the crystal. This wetting behavior is summarized in Figure (5.15) where we show the thickness

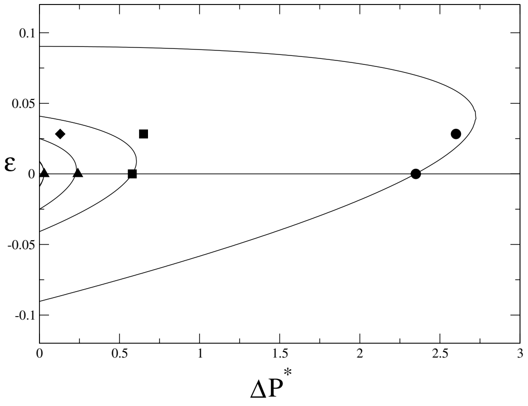

Figure 5.13: Location of the first four layering transitions in the plane spanned by ΔP^* and ϵ. The curves are the theoretical predictions for a crystal lattice constant which is shrunk ($\epsilon < 0$) or grown ($\epsilon > 0$) compared to the coexisting bulk crystal. The different symbols show computer simulation results for the crystallization transitions in the different layers.

of the wetting layer ℓ versus $-\ln \Delta P^*$. Although we were not able to resolve the order parameter to a very high layer thickness the measured thickness from the minima of the density profile clearly indicates a logarithmic growth of the wetting layer.

Again, complete wetting proceeds via a cascade of discrete layering transitions. From a fit of the data of Figure (5.15) we extract the correlation length of $\ell_0 = 1.01\sigma$ and the amplitude of $\gamma_0 = 0.56 k_B T/\sigma^2$. ℓ_0 is remarkably lower than for a triangular pattern. Clearly, ℓ_0 depends on the surface pattern as described in more detail in a different context of surface melting [143, 144].

5.8 Conclusions

In this chapter we have discussed the influence of the structure of a substrate pattern. We found that it influences profoundly the wetting scenario by crystalline phases. The most intriguing fact is that the onset of surface freezing can be significantly shifted away from coexistence when the system is in contact with a wall pattern that favors the crystal. Here we have investigated different patterns like

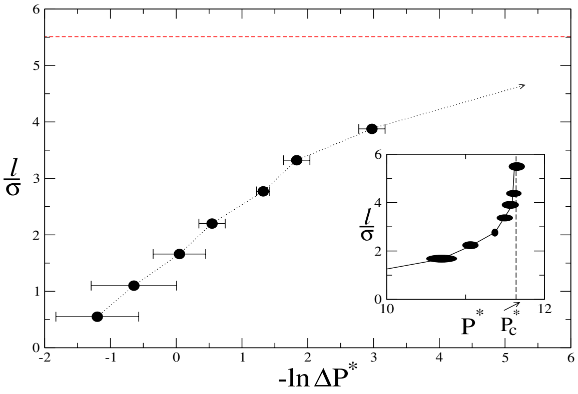

Figure 5.14: Thickness ℓ of the crystalline wetting layer versus $-\ln \Delta P^*$ as measured with the order parameters $\Psi_n^{(2)}$. The thickness seems to converge toward 5.5σ as shown in the inset where the thickness ℓ is plotted versus P^*.

the triangular and the hcp (110) one which lead to complete wetting by crystalline sheets.

However, by applying patterns which are distorted from the ideal form as the rhombic pattern or an ideal pattern which has lattice constant mismatch we find incomplete wetting by a crystal. There is only a finite number of crystalline sheets as bulk coexistence is approached from below. This number depends crucially on the lattice distortion with respect to an ideal one which is commensurate to a coexisting bulk crystal. Furthermore, even commensurate wall patterns can lead to incomplete wetting as demonstrated for the square wall and the fcc (110) pattern. In the case of very unfavorable structures such as the highly distorted rhombic pattern, surface freezing is completely prevented.

Our theoretical predictions also set a scenario for modern experimental techniques using sterically stabilized colloidal suspensions near a patterned wall [12, 46], where it should be possible to observe our predictions in real-space or scattering experiments.

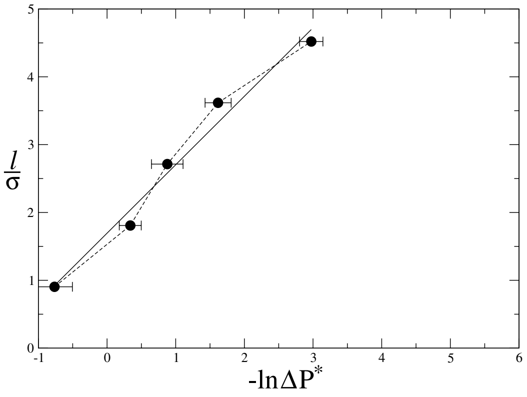

Figure 5.15: Thickness ℓ of the wetting layer versus $-\ln \Delta P^*$ as measured with the order parameters $\Psi_n^{(2)}$. The straight line is the best linear fit for the simulation data.

Chapter 6

Surface induced structural correlations

In this chapter we focus on structural correlations as found by the authors of [23]. These correlations are induced by the influence of a patterned substrate on a fluid system. In particular structural correlations expressed by the structure factor and symmetry parameters are of interest and shall be discussed here.

Again we will use a hard sphere system as described in chapter 2 to gain a better understanding of the fundamental concepts. We will focus on two main approaches: First, we will adjust the hard sphere system to fit the experiments [23] and we will investigate the properties of the structure factor of the fluid exposed to the structure surface. To be in correlation with the experiments we simulate a measurement done with evanescent wave scattering. The data obtained by our computer simulations can then serve as benchmark for real X-ray experiments, especially to detect any deviation in the behavior from a pure hard sphere system [145].

In the second part of this chapter we will focus upon the recently found five-fold symmetry of liquids at interfaces. The authors of [23] were able to use a patterned surface to measure a five-fold symmetry in the liquid. The occurrence of five-fold symmetry in bulk liquids has often been discussed [146] and has even been reported for some systems like glasses [147, 148]. However, most of the systems exhibiting five-fold symmetry have either a high density and form glass-like states or they have non radial symmetric potentials which favor a five-fold symmetry. However, by bringing the liquid into contact with a surface it might be possible to enhance, measure or create this five-fold symmetry.

6.1 The model

The hard sphere system in contact with a structured surface serves as a theoretical model. This is justified as we are interested only in the structural and symmetrical properties of the system and not in the exact details governed by the interaction potential and chemical bonding. Certainly, we cannot make any prognosis on these properties but structural and entropic properties are reflected well by a hard sphere system and it serves as an ideal test case for real experiments. In particular, it can be used to elucidate which effects seen in the experimental structure factor are due to the hard core interaction of the real particles and which are due to energetic interactions or spurious effects not considered in the hard sphere theory.

As before we simulate a system of N hard spheres of diameter σ at positions $\vec{r_i} = (x_i, y_i, z_i)$ at temperature T confined in a rectangular box of fixed volume $V = L_x L_y L_z$. The hard spheres interact with the interaction potential as given in Eqn. (2.1) and again temperature only sets the energy scale and does not affect structural correlations. We therefore effectively describe the system with one parameter, the packing fraction η.

For computational purposes we apply periodic boundary conditions in the x- and y-directions while in the z-direction two surfaces at $z = 0$ and $z = L_z$ are modeled. Although the real system has only one surface the simulation requires the second surface at $z = L_z$. However, from chapters 4 and 5 we know that the lateral distance L_z between the two surfaces needs to be large enough so that no surface-surface interactions will occur.

To study the interaction of the fluid with the structured surface the surfaces have an imprinted pattern which consists, for the sake of simplicity, also out of hard spheres positioned on a predefined lattice $\{\vec{r_i^w}\}$. This procedure has the advantage that we avoid the introduction of another energy scale which would correspond to considering a temperature scale. The surface-fluid interaction is therefore also hard sphere like as given by Eqn. (2.1).

However, to take a varying strength of the surface potential into account we change the penetration depth $l = s\sigma$ of the surface particles entering the fluid. Maximal interaction is achieved for $s = 1/2$, where exactly half a sphere is penetrating the fluid creating a very strong surface-fluid interaction. Reducing the interaction by lowering the penetration depth yields in the limit of $s = 0$, a hard flat wall, where no structural quantities in the $x - y$ plane are left. These surface spheres are designed so that they are either fixed spherical caps protruding from a flat surface by a given height l, representing a very rigid wall or they are al-

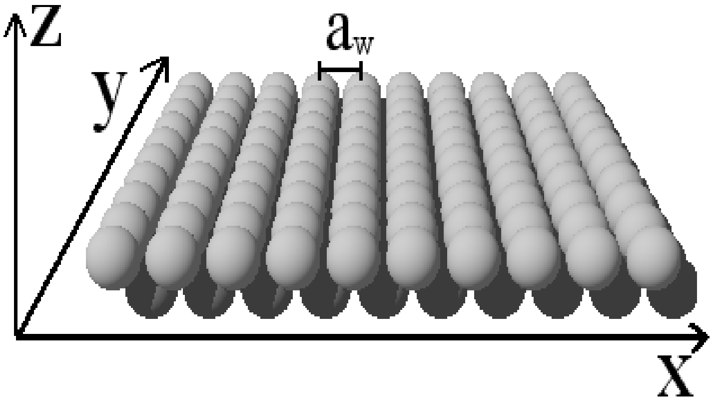

Figure 6.1: Structured surface made out of fixed hard spheres forming a (100) plane of an fcc crystal.

lowed to move statistical around their ideal lattice positions $\vec{r}_i^w$ to model thermal fluctuations. We will investigate both situations to find out the role of thermal fluctuations.

6.2 Structure factor of inhomogeneous hard sphere fluids

To differentiate between various spurious effects seen in the experiments [23] when measuring the structure factor, we analyse in a simple hard sphere computer simulation also the structure factor. In the experiments evanescent waves are used to probe the vicinity of the surface. We mimic this measurement in the computer simulation be a special algorithm to calculate the structure factor at the interface. We will then focus on various experimental effects and disturbances and evaluate their importance on the measured data. In particular, we are interested in the effects of a thermal motion of the particles at the surface, in varying penetration depths of the evanescent wave and in the comparison of commensurable and incommensurable surface patterns.

6.2.1 Evanescent wave measurements

Evanescent wave measurements are used to analyse the microscopic structure of a surface. In contrast to normal scattering experiments an evanescent wave probes only a very small portion of the material around the surface, that is its penetration depth into the material is very small. Analysing the scattering information obtained from these experiments yields information about the structure of the material near or at the surface.

Experiments are usually performed by shining a beam, often an X-ray beam at a grazing angle onto the material. If this angle is small enough, that is flatter than the angle of total reflection the beam will be totally reflected. Despite this total reflection parts of the electromagnetic wave will penetrate the material and travel inside the probed material. Although this part of the wave decays exponentially with the penetration depth it can be used for obtaining information about the structure of the surface in scattering experiments [149].

The model system should be used to compare characteristic structural data with real evanescent wave X-ray experiments. Therefore the analysis will be focused on measuring the structure factor of the fluid gained by evanescent wave scattering at the surface. In particular, the dependency of the structure factor on the $\vec{k}$-vector and on the direction of the crystal relative to the incoming beam will be investigated.

Evanescent waves [149, 150, 151] are produced by an incoming electromagnetic wave with wave vector $\vec{k}_i$ as depicted in Figure (6.2). The wave hits a surface at an angle θ_i less than the angle of total reflection θ_c. Although the wave is totally reflected, leaving the surface with an outgoing wave vector $\vec{k}_f$, part of the wave penetrates the surface material with a depth of a few wavelengths. The intensity of the wave in the medium is given as

$$I_{ev} = I_0 e^{-2*z/\zeta} \tag{6.1}$$

where ζ is the penetration depth given by

$$\zeta = \frac{\lambda_0}{2\pi/n} \sqrt{\sin^2\theta_i - \sin^2\theta_c}\,, \tag{6.2}$$

where λ_0 is the wavelength of the electromagnetic wave, n the refraction index, z the distance from the interface and I_0 the initial intensity at the interface. This exponentially damped wave can be described by a wave vector which has an additional imaginary part into the z-direction and real parts in all other directions

$$\vec{k} = k_x \vec{e}_x + k_y \vec{e}_y + (k_z + i/\zeta)\vec{e}_z \tag{6.3}$$

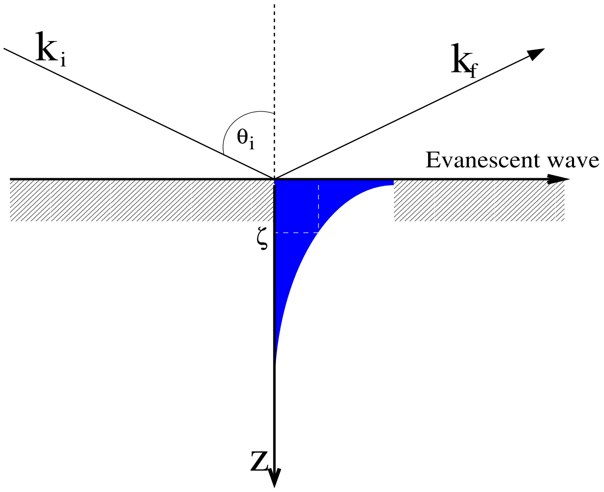

Figure 6.2: Geometry of evanescent wave scattering. An incoming beam $\vec{k}_i$ hits the surface at an angle θ_i flatter than the angle of total reflection. It is therefore totally reflected but an evanescent wave penetrates the surface up to a penetration depth ζ. This evanescent wave travels parallel to the surface and the incoming beam.

where $\vec{e}_x$,$\vec{e}_y$,$\vec{e}_z$ denotes the unit vectors into the x, y, z-direction. The imaginary component in the exponent leads to the description of the damping. In the medium the evanescent wave travels parallel to the surface in the same direction as the incoming beam and it can be used to probe the structure of the interface as the interference pattern will bear resemblance to the interference of the evanescent wave with the surface structure.

In the computer model, the measurement of the interference pattern of the evanescent wave is equivalent to analyzing the structure factor of the fluid using an imaginary wave vector in the z-direction respectively the Laplace transform of the bulk structure factor. The bulk structure factor is derived from the Fourier transform [2, 49, 84]

$$\hat{\rho}_{\vec{k}} = \sum_{j=1}^{N} e^{-i\vec{k}\vec{r_j}} \tag{6.4}$$

of the number density $\rho(\vec{r})$, that is

$$S(\vec{k}) = \frac{1}{N} \left\langle \rho_{\vec{k}} \rho_{\vec{k}^*} \right\rangle \ . \tag{6.5}$$

To analyze the angular dependency of the surface pattern the incoming beam $\vec{k}_i$ is rotated in the real X-ray experiments. This is taken into account by writing the k vector in polar coordinates

$$\vec{k} = k_{||} \cos(\phi) \vec{e}_x + k_{||} \sin(\phi) \vec{e}_y + (k_\perp + i/\zeta) \vec{e}_z \tag{6.6}$$

where ϕ is the angle to the [010]-direction and varying the angle ϕ. Inserting the complex $\vec{k}$-vector into the structure factor we obtain

$$\begin{aligned} S(\vec{k}) \quad &= \quad \frac{1}{N} \left\langle \sum_{j=1}^{N} e^{-2/\zeta \vec{e}_z \vec{r}_j} \right\rangle + \qquad (6.7) \\ & \quad\ \ \frac{1}{N} \left\langle \sum_{l=1}^{N} \sum_{j=1}^{N} e^{-i \Re \vec{k} (\vec{r}_l - \vec{r}_j)} e^{-1/\zeta \vec{e}_z (\vec{r}_l + \vec{r}_j)} \right\rangle \ . \end{aligned}$$

Eqn. (6.7) is now used for further analysis in particular in the computer *Monte-Carlo* simulations. These simulations are standard *Monte-Carlo* simulations in a constant volume (NVT) ensemble as described in section 3.2. In these simulations we can directly measure thermodynamical averages and therefore obtain the structure factor of Eqn. (6.7).

6.2.2 Adjustment to the experimental data

The experiments from the authors of [23] are done for a silicon Si(100) solid surface in contact with liquid lead (Pb) at a temperature of $T \approx 645K$ slightly above the melting temperature $T_{\text{melt}} = 600K$ of lead. The critical angle of reflection for this system is $\theta_c = 0.043\,^\circ$ at a wavelength of $\lambda = 0.177$ Å.

Moreover from the experimental details [23] we obtain a penetration depth of $\zeta \approx 50 \ldots 60$Å while the real part of the z component of the wave vector $k_\perp \approx 0$ can be neglected.

To compare the hard sphere model with the experimental data of lead on a silicon surface we need to adjust the free parameters of the hard sphere model namely the packing fraction η and the diameter σ and the surface structure $\{\vec{r}_i^w\}$ to fit the given experimental parameters best.

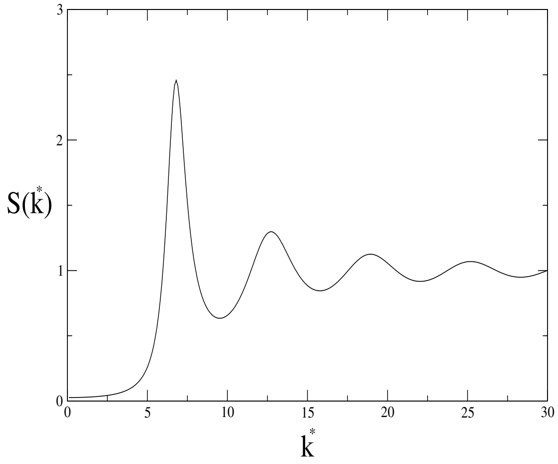

Figure 6.3: Bulk structure factor $S(k^*)$ versus $k^* = |\vec{k}|/\sigma^{-1}$ of a hard sphere fluid of packing fraction $\eta = 0.445$ in PY approximation.

First, it has to be verified that that structure factor of liquid lead is mainly dominated by a hard sphere core. By comparing the bulk structure factor of liquid lead as given in [152] with the structure factor measured in hard sphere simulations or directly calculated by the Percus-Yevick (PY) analysis

$$\begin{aligned} S_{\mathrm{PY}}^{-1}(\vec{k}) &= 1 - \frac{3}{2}\eta \left\{ -3\eta(1 + 4\eta + 4\eta^2 + 4k^2 + 4\eta k^2 + \eta^2 k^2) \right. \\ &+ [4k^4 - 12\eta^2(k^2 - 1) + \eta(3 + 6k^2 - 6k^4) \\ &\quad + \eta^3(12 - 21k^2 + 2k^4)] \cos 2k \\ &- \left. 2k(-3\eta - 12\eta^2 - 12\eta^3 + k^2 - 6\eta k^2 + 5\eta^3 k^2) \sin 2k \right\} \\ &/ \left\{ (-1 + \eta)^4 k^6 \right\} \end{aligned} \tag{6.8}$$

we find a very good agreement of both structure factors. Figure (6.3) shows the structure factor as obtained by PY analysis. It is almost identical to the one measured and shown in [152]. From this good agreement we assume that the surface structure factor measured with evanescent waves will also compare well with the hard sphere model.

In the following we use the data of [152] for the temperature of $T = 613K$ $k_{\mathrm{max}} = 2.21$ Å and $S(k_{\mathrm{max}}) = 2.64$ and compare it with the PY results for $\eta = 0.46$ which gives $k_{\mathrm{max}} = 3.426\sigma^{-1}$ and $S(k_{\mathrm{max}}) = 2.63$. For the temperature of

$T = 873K$ we obtain on the other hand $k_{\text{max}} = 2.21$ Å and $S(k_{\text{max}}) = 2.12$ and compare it with the PY results for $\eta = 0.41$ which gives $k_{\text{max}} = 3.34\sigma^{-1}$ and $S(k_{\text{max}}) = 2.13$. The third comparison to fit is for the approximate experimental temperature of $T = 645K$ used in [23] which has a measured $S(k_{\text{max}}) \approx 2.42 \ldots 2.5$. The best fit packing fraction for these experiments from [23] is therefore $\eta = 0.445$ with a mean particle distance $a = \rho^{-1/3} = 1.185\sigma$ with the PY results for $\eta = 0.445$ which gives $k_{\text{max}} = 3.40\sigma^{-1}$ and $S(k_{\text{max}}) = 2.46$. Using the lead mean particle distance of 4.9505 Å [23] and solving for σ we obtain $\sigma = 4.1776$ Å . We measure all theoretical lengths in units of this hard sphere diameter σ. From the experimental penetration depth of $50 \ldots 60$ Å we further obtain $\zeta = 11.97 \ldots 14.36$ or respectively $1/\zeta = 0.0835 \ldots 0.0696$.

In the experiments [23] liquid lead is in contact with the (100) surface of the silicon crystal, therefore we have to model the surface in the computer simulation as representation of the (100) plane of a hard sphere crystal. This is done by cutting an fcc crystal along its (100) plane and imprinting it onto the surface. The lattice constant a_w of this crystal can be still adjusted to study commensurate ($a_w = a_c = a$) and incommensurate ($a_w = a_i \neq a$) surface patterns as depicted in Figure (6.1).

6.2.3 Results

Analysis of large $k_{||}$

The first question posed in the experiments [23] had been the dependences of the structure factor as defined in Eqn. (6.7) for large wave vectors $k_{||}$. In particular, for the described experiments [23] a deviation for incommensurate substrates of these values from the bulk values could be seen.

Analysing Eqn. (6.7) for $|k_{||}| \to \infty$ while keeping the imaginary part ζ non infinite yields a structure factor

$$S_\infty := S_\infty(\zeta) = \frac{1}{N} \left\langle \sum_{j=1}^{N} e^{-2/\zeta \vec{e} \vec{r}_j} \right\rangle . \tag{6.9}$$

However, this expression no longer depends on the structure of the surface pattern or the $x - y$ arrangement of the particles. With given penetration depth ζ it is solely determined by the z-position of the particles. This z-position generally does not depend on the surface pattern or the orientation of the surface to the incoming beam but only on the properties of the fluid itself.

We can approximately write Eqn. (6.9) as

$$S_\infty(\zeta) \approx \int_0^\infty dz\, \rho(z) e^{-2z/\zeta} \tag{6.10}$$

where $\rho(z)$ is the lateral integrated density

$$\rho(z) = \int_{-\infty}^{\infty} \int_{-\infty}^{\infty} dx dy\, \rho(x, y, z). \tag{6.11}$$

To compare the measured structure factors for different penetration depths ζ with each other and especially with bulk measurements it is actually recommended using the quantity S_∞ as normalization constant, that is we define

$$S^*(\vec{k}) := \frac{S(\vec{k})}{S_\infty} \tag{6.12}$$

yielding structure factors which are all commonly normalized onto 1 for large wave vectors.

Structure factor for mobile surface spheres

First we use the computer simulations to analyse the effects of thermal fluctuations of the surface particles on the structure factor. We mimic these fluctuations by allowing the surface particles to fluctuate around their ideal lattice position. This is done by choosing random *Monte-Carlo* moves of a radial distribution as provided by the *Lindemann* parameter L defined in section 3.5.5, ranging from $L = 0$, that is completely fixed surface particles, to $L = 0.15$ which is very mobile and fluid like surface particles. The more fluctuations the surface particles experience the less they behave as a rigid surface forcing its structure onto the fluid. The surface itself becomes more and more fluid like. However, a certain mobility of the surface particles models more closely to reality, in which particles of a solid fluctuate around $10-15\%$ around their ideal lattice positions. This effect has to be taken into account when comparing computer simulations with the experimental situation.

In Figure (6.4) we present the resulting structure factor for the mobile surface particles for an incident beam along the [010] respective $\vec{e}_y$ direction of the crystal. The surface particles interact strongly with the fluid given by a surface-fluid interaction parameter of $s = 0.5$ but the fluctuations of the spheres is changed from $L = 0 \ldots 0.15$.

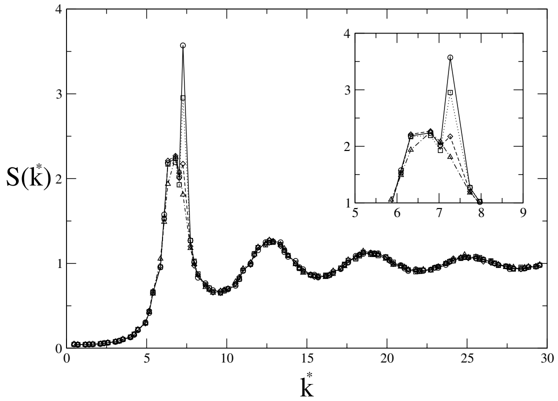

Figure 6.4: Structure factor $S(k^*)$ versus $k^* = k/\sigma^{-1}$ of the hard sphere fluid at $\eta = 0.445$ with strong interaction potential $s = 0.5$ and mobile surface spheres forming a square surface pattern. Different curves show increased mobility (from top to bottom: $L = 0.0, 0.05, 0.1, 0.15$) of the surface particles. The transition from a strongly crystalline peak in the structure factor to a fluid structure factor can be seen clearly. The inset is a enlarged portion of the curve around the first maximum.

In the simulations we find that for very mobile fluctuating surface particles there is hardly any effect of the surface on the structure factor. We find almost the exact the bulk fluid structure factor. Yet for reduced fluctuations a crystal peak at the first maximum emerges from the bulk structure factor. This clearly shows how the surface pattern forces its structure more and more onto the fluid which has to form around the given pattern for a rigid structure.

From this analysis we obtain that a chosen fluctuation of $L = 0.10$ fits the experimental data [23] best.

Structure factor for fixed surface spheres

As a second step we analyze the effect of the strength of the surface-fluid potential on the structure factor. As the hard sphere model does not include any energy effects but all interactions are entropical governed by the excluded volume interaction we do not introduce an attraction of the surface but model the surface interaction by hard spherical caps which extend a given distance $l = s\sigma$ into the

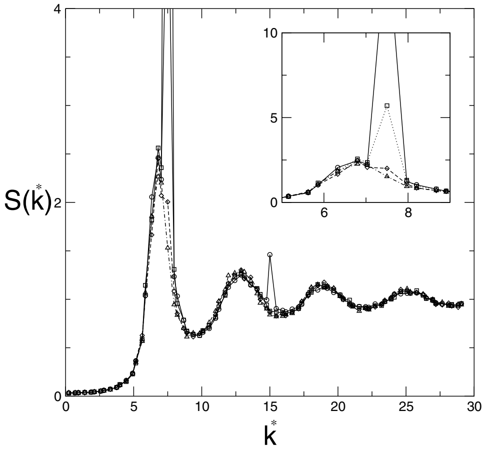

Figure 6.5: Structure factor $S(k^*)$ versus $k^* = \vec{k}\vec{e}_y/\sigma^{-1}$ of the hard sphere fluid at $\eta = 0.445$ with varying interaction potential strength $s = 0.5, 0.3, 0.2, 0.0$ (top to bottom) and fixed surface spheres forming a (100) plane of a fcc crystal. The transition from a strongly crystalline peak in the structure factor to a fluid structure factor can be clearly seen. The inset enlarges the first maximum.

fluid. For large s, the fluid will be forced to flow around the surface particles adopting the surface structure. In the limit $s \to 0$ the surface reduces to a hard flat surface which gives the rotational invariant bulk structure factor.

In Figure (6.5) the effect of increased surface potential is depicted for an incoming beam along the [010] respective $\vec{e}_y$ direction. For increased surface-fluid interaction we find the formation of crystal peaks at the position of the ideal Bragg crystal peaks. For small surface-fluid interactions we are left with a bulk-like structure factor.

We note that the effect of the reduced surface potential is similar to that of the moving surface spheres. We choose a potential of $s = 0.25$ to represent the experimental data [23] well.

Variation of the penetration depth

As already seen in section 6.2.3 the penetration depth of the evanescent wave does not affect the properties of the structure factor for large $\vec{k}$. However, the properties for small $\vec{k}$ and especially of the first maximum are changed. A smaller

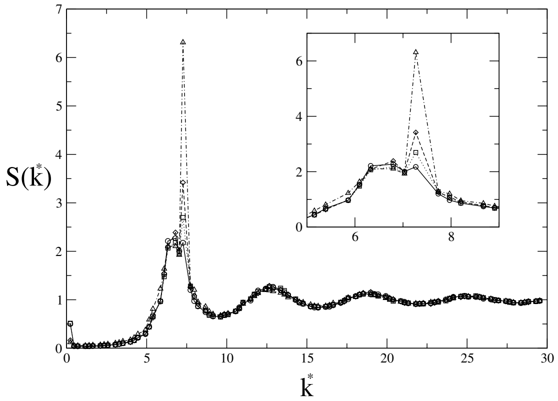

Figure 6.6: Structure factor $S(k^*)$ versus $k^* = \vec{k}\vec{e}_y/\sigma^{-1}$ of the hard sphere fluid at $\eta = 0.445$ for a commensurate surface pattern. Different curves show the effect of reduced penetration depth ζ (bottom to top: $1/\zeta = 0.0, 0.07, 0.14, 1.0$). Larger $1/\zeta$ pronounces the effects of the surface structure while a smaller $1/\zeta$ superimposes a larger bulk part onto the structure factor. The inset shows the enlarged first maximum of the structure factor.

penetration depth pronounces the effect of the surface as it mainly measures layers close to the surface. A larger penetration depth superimposes more of the bulk behavior to the structure factor.

In Figure (6.6) we show the effect of varying penetration depths. It can be clearly seen that for smaller penetration depths the crystal structure in the first maximum is becoming more pronounced while for larger penetration depth this information is lost. We point out that it is important for experiments to reduce the penetration depth, that is the angle of the incident beam in order to analyse the surface structure effects.

However to comply with the experimental situation we choose the penetration depth of $1/\zeta = 0.070$ as given in the experiments [23].

Effects of an incommensurate surface pattern

In Figures (6.7), (6.8) and (6.9) we investigate the effects of an incommensurate surface pattern for an incoming beam along the [010] direction. The other parameters are held constant to fit the experiments best, that is $s = 0.25$ and $L = 0.1$.

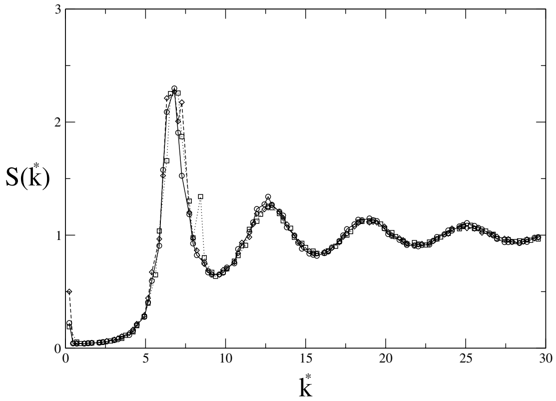

Figure 6.7: Structure factor $S(k^*)$ versus $k^* = \vec{k}\vec{e}_y/\sigma^{-1}$ of the hard sphere fluid at $\eta = 0.445$ for a flat surface (straight line), a commensurate surface (dotted line) and an incommensurate surface (dashed line) for an incident beam along the [010]-direction. The high penetration depth $1/\zeta = 0.0$ does not allow one to resolve any details of the surface structure.

We compare the structure factor of the bulk fluid with the commensurate surface pattern and the incommensurate pattern. We find that while the bulk structure factor does not naturally show any effects of a crystal structure the commensurate pattern superimposes a clearly visible crystal peak at the position $2\pi/a_c$. Choosing an incommensurate surface pattern does in principle yield the same effect but the peak is shifted to the lattice spacing of the incommensurate surface pattern $2\pi/a_i$.

However, we do not find any general changed quantities of the incommensurate surface pattern. This is in contrast to the results as seen in the experiments [23]. These experimental effects must be attributed to the fact that the surface fluid interaction in the experiment is more complicated than a pure hard-sphere hard-surface interaction and the energetic effects such as electromagnetic attraction and repulsion between the electron shells takes place and has a significant effect on the fluid surface interaction.

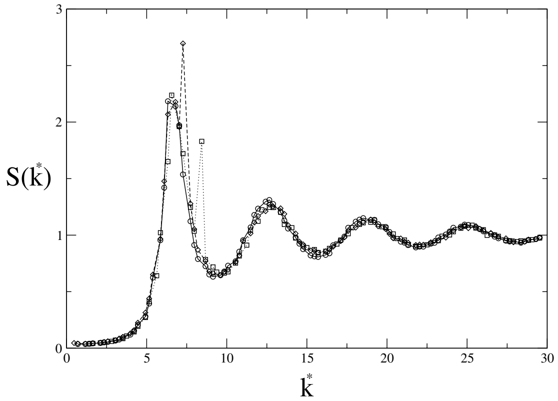

Figure 6.8: Same as Figure (6.7) but for a shorter penetration depth $\zeta = 1/0.070$. The surface pattern of the commensurate produces a clearly visible crystal peak at $2\pi/a_c$. The incommensurate pattern does the same though shifted and with reduced intensity.

Rotation of the crystal surface

Another measurement done in the experiments is the rotation of the surface of the silicon crystal relative to the incoming beam, that is varying angle ϕ. This allows the evanescent wave which travels parallel to the surface and the incoming beam to probe different directions of the liquid lead. In a crystal this would correspond to probing different lattice planes. In an ideal fluid we would expect no dependency on the angle of rotation ϕ.

In our simulation system it is very difficult to analyze this angular dependency in detail as we are restricted to very small surface areas due to restriction in the available computer power. It is only possible to simulate systems of a few thousand upto ten thousand particles. Yet these particles have to be used to simulate a bulk system large enough to guarantee that the two surfaces do not influence one another. The surface area will only be $A \propto N^{2/3}\sigma^2$ and therefore only a few hundred σ^2 in size. Probing higher order lattice planes is virtually impossible as there are not enough interfering wave vectors to produce a proper signal. So only a probing in the main lattice directions like [100], [110] or [111] is feasible.

Due to these restrictions it is not possible to gain simulation data to verify the

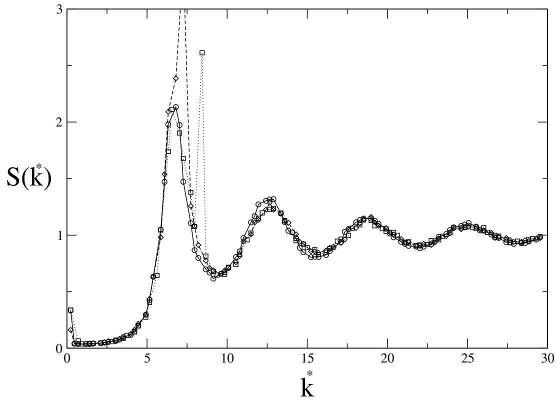

Figure 6.9: Same as Figure (6.8) but for a even shorter penetration depth $\zeta = 1/0.140$. The effect of the surface pattern is further pronounced and the surface structure can be clearly identified.

experimentally found rotational symmetries. Yet it is possible to make a theoretical prediction as we found that the structure factor is only a superposition of the bulk structure factor and damped crystal peaks. As the bulk fluid structure factor is rotational invariant, it provides only a common background to the structure factor and therefore no additional components arise which depend upon the angle of rotation ϕ.

The remaining crystal parts should yield a normal crystal structure factor representing the scattering Bragg planes of the crystal [153, 154]. For the experimental evaluation it is recommended to subtract the bulk fluid structure factor from the measured structure factor to obtain the crystal part of the structure factor and then to analyze this further for rotational symmetries respective crystal lattice peaks.

6.3 Surface induced five-fold symmetry in hard-sphere fluids

The authors of [23] revived an old question in whether a bulk liquid is a completely unordered substance or exhibits five-fold symmetry corresponding to the local occurrence of icosahedral or dodecahedral clusters [146]. Such a symmetry has been found in computer simulations for hard spheres and other systems with a simple radial symmetric potential and experiments with colloidal particles [155]. when the liquid was strongly super-cooled or glass like. Yet it is still debated whether or not *non* super-cooled bulk liquids exhibit this symmetry.

This question arises from the difference between a fluid and a crystal and the possibility to strongly super-cool many liquids. On one hand a crystal is a regular structure which fills the whole space. This is only possible for certain rotational symmetries like $2, 3, 4, 6$ fold. Other rotational symmetries such as the above discussed five-fold symmetry lead to icosahedral or dodecahedral building blocks which do not allow space to be filled completely with a regular structure. Due to this fact it is a long debated issue [146, 156, 157, 158, 159, 160] whether a liquid is completely unstructured or built by local five-fold symmetric clusters. Such a structure would explain the possibility to super-cool a liquid. Super-cooling occurs if a liquid remains liquid below its freezing point and could be due to the fact that only after rearranging the five-fold symmetric clusters in a crystalline symmetry would the system freeze.

However, experimental studies are difficult because techniques such as scattering experiments average over all orientations of the molecular clusters and therefore cannot detect local order. Computer simulations on the other hand have been performed for a variety of bulk liquids [73, 74, 75, 161]. However, for simple potentials such as the hard-sphere potential or a *Lennard-Jones* potential five-fold symmetry was not found for a bulk liquid. In both systems, five-fold symmetry only occurred for high density, super-cooled liquids or glasses or by directly applying potentials which inherently favor a five-fold symmetry [146].

In the following we take a different approach to analyze the experiments described in the first part of this chapter. We focus on the creation of a fluid at the surface which exhibits the five-fold symmetry by locally increasing the density.

6.3.1 The model

To focus on the analysis of the five-fold symmetry we modify the model described in section 6.1 in two ways. First, we increase the incommensurability by making the lattice constant of the surface pattern very large. We analyse a triangular pattern as cut through the fcc (111) crystal[1] with a lattice constant of $a = 1.37\sigma$.

---

[1] We have also performed these simulations for a fcc (100) pattern but could not raise the fluid densities high enough. Crystallization always set in before reaching packing fractions $\eta \geq 0.6$. As the surface pattern serves only as means to prevent crystallization we focus in the following

structure	Q_4	Q_6	$\hat{W}_4$	$\hat{W}_6$
fcc	0.191	0.575	−0.159	−0.013
hcp	0.097	0.485	0.134	−0.012
bcc	0.036	0.511	0.159	0.013
sc	0.764	0.354	0.159	0.013
icosahedral	0.0	0.663	0.0	−0.169
dodecahedral	0.0	0.369	0.0	0.169
liquid	0.0	0.0	0.0	0.0

Table 6.1: Three dimensional bond orientational parameter for various cluster geometries.

This spacing is large enough so that we expect to prevent any surface freezing even for very high densities as discussed in chapter 5 where we analysed the dependence of the surface freezing from the surface pattern.

Second, we apply an attractive potential perpendicular to the surface. This does not correspond to the experiments [23] but allows to increase the local density while keeping the bulk system at fluid densities. By doing so we investigate a possible effect of the interface in the experiments, namely that it creates a inhomogeneous fluid of high density. As our investigation does not strongly depend on the exact choice of the potential we choose the interface-fluid potential to be the attractive tail of a $9-3$ *van der Waals* potential

$$V(z)=\begin{cases} V_{\min} & \text{if } z<z_{\min} \\ -\frac{3\sqrt{3}}{8}V_{\min}\left(\left(\frac{l_0}{z-z_0}\right)^9-\left(\frac{l_0}{z-z_0}\right)^3\right) & \text{otherwise}\end{cases} \tag{6.13}$$

with $V_{\min}$ being the minimum of the potential occuring at $z_{\min}=3^{1/6}l_0$, l_0 its range and with the offset z_0 of the potential chosen so that the minimum of the potential is close to the surface ($z=0$). Our choice for z_0 is $z_0=-z_{\min}+\sigma$. Note that Eqn. (6.13) relates to the usual *van der Waals* equation for the attraction of a surface by $\epsilon_{\mathrm{vdW}}=-\frac{3\sqrt{3}}{8}V_{\min}$ and $V_{\min}$ being the depth of the minimum of the potential. Applying the potential Eqn. (6.13) to a hard sphere system will create a very inhomogeneous hard-sphere fluid with a strongly enhanced density close to the surface.

In contrast to the structure factor investigated in the first part of this chapter, the detection of the symmetry of the fluid is done by analysing a specially tailored

---

on the fcc (111) pattern.

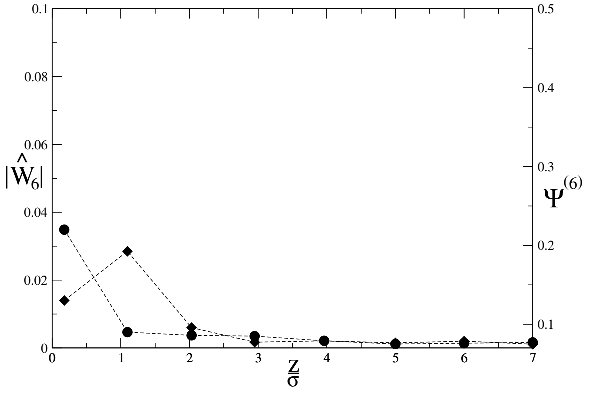

Figure 6.10: Analysis of the symmetry of the hard-sphere liquid for $V(z) = 0$. The $\hat{W}_6$ (diamonds) and $\Psi^{(6)}$ (circles) parameters are shown. Close to the interface the influence of the interface can be seen in a slight raise of the six-fold symmetry in $\Psi^{(6)}$. However, there is no noticeable five-fold symmetry.

order parameter which is sensitive to rotational symmetries and therefore better suited to locating five-fold symmetries than the structure factor. As an order parameter we take the layer resolved order parameters as defined in section 3.5. In order to detect how the structure of the surface is transferred into the fluid, we measure the layer resolved order parameter $\Psi^{(k)}$. Therefore, for a triangular pattern we expect an increase of $\Psi^{(6)}$. The five-fold symmetry is measured using the layer resolved three dimensional bond order parameter Q_4, Q_6 and $\hat{W}_4$, $\hat{W}_6$. According to [146] a high value of $|\hat{W}_6|$ is a clear indication for five-fold symmetry as it shows icosahedral or dodecahedral bond statistics in the system. Q_4, Q_6 and $\hat{W}_4$ are used as additional control parameters. In Table 6.1 we summarize all values of these bond-order parameters for the ideal crystals. Note however, that for the icosaderon and dodecahedron it is geometrically not possible to form a crystal as it is not possible to flawlessly fill a three dimensional space with them. The values of the order parameters are therefore calculated for a single ideal icosaderon and dodecahedron centered around the origin. Naturally, it is not possible in a real system to come even close to the ideal values. The authors of [146] suggest that values of $|\hat{W}_6| < 0.02$ indicate crystal ordering and values of around $|\hat{W}_6| > 0.05$ show the occurrence of five-fold symmetries in the system. For evaluation we take the absolute value $|\hat{W}_6|$ as the sign of $|\hat{W}_6|$ only differentiates

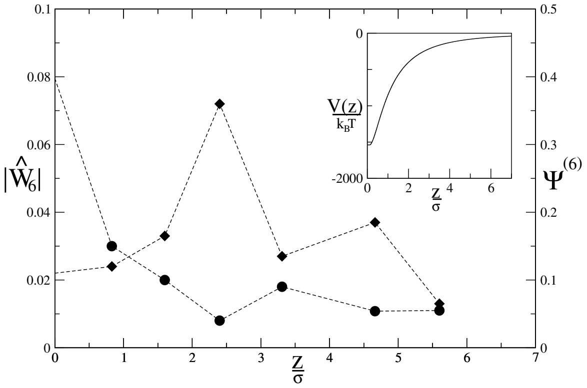

Figure 6.11: Analysis of the symmetry of the hard-sphere liquid for $V_{\text{min}} = 1000$. The $\hat{W}_6$ (diamonds) and the $\Psi^{(6)}$ (circles) parameters are shown. The inset depicts the external potential. The interface induces a six-fold symmetry as seen in $\Psi^{(6)}$ close to the interface. Further apart the occurrence of a fluid sheet with five-fold symmetry can be detected.

between icosahedral and dodecahedral order and has no real meaning in a bulk system [146]. Furthermore, experimental measurements within real hard-sphere-like colloidal systems of high densities find values of $|\hat{W}_6| \approx 0.045$ sufficient for at least moderate five-fold symmetries in the system.

6.3.2 Results

We prepare a hard-sphere fluid system of packing fractions of about $\eta = 0.49$ which is still well into the fluid regime. This system is equilibrated and then put into contact with a structured surface where the imprinted pattern is a cut through a fcc (111) crystal with lattice spacing of $a = 1.37\sigma$. However, the exact spacing does not profoundly influence the results as long as it is chosen large enough to prevent crystallization.

We then apply an attractive potential of Eqn. (6.13) with $l_0 = 2.0\sigma$ at the surface. This will attract particles to the surface and thereby increase the density of the fluid in proximity of the surface. Starting from no potential, that is $V(z) \equiv 0$ we increase the potential until we achieve fluid densities high enough to show five-fold symmetry. This is reported by the authors of [155] to happen at $\eta \geq 0.6$.

For vanishing potential we find a weak transfer of the surface structure onto the fluid recognized by a value of $\Psi^{(6)} = 0.22$ in the first layer. Close to the surface we also find a very weak indication of five-fold symmetry. This is shown by a value of $|\hat{W}_6| = 0.014$. However, both rotational symmetries decay very fast when approaching the bulk fluid with densities of $\eta = 0.49$. These results are summarized in Figure (6.10).

To increase the density of the fluid to packing fractions of $\eta \geq 0.6$ we increase the potential to several hundred $k_B T$ and find increasing values of $|\hat{W}_6|$. We present our results for a value of $V_{\text{min}} = 1000 k_B T$. Due to the high attraction the surface pattern transfers more profoundly into the fluid than before. We find a value of $\Psi^{(6)} = 0.4$ for the first layer indicating a high degree of order in the first layer. However, as depicted in Figure (6.11) this order decays fast farther away from the surface and is replaced by a well pronounced five-fold order indicated by $|\hat{W}_6| = 0.069$ at densities of about $\eta \approx 0.62$. With reducing density this five-fold symmetry is lost farther away from the surface.

Summarizing we find an interesting behavior for a very strongly attractive surface. Close to the surface the surface pattern is transferred into the fluid. This leads to an inhomogeneous fluid exhibiting the symmetry of the surface. In the case of the fcc (111) surface we obtain a six-fold symmetry in the fluid. Further away from the surface the symmetry of the surface pattern is lost and the high density fluid shows a moderate five-fold symmetry. To exhibit this behavior the packing fraction of the fluid needs to be about $\eta \geq 0.60$. Even further away from the surface, the weakening attraction of the surface leads to a reduction of the density of the fluid and consequently to a loss of the five-fold symmetry. This behavior is summarized in Figure (6.12). However, if the attraction of the surface is not strong enough to increase the packing fraction of the fluid above $\eta \geq 0.60$ no five-fold symmetry is found.

6.4 Conclusions

From our analysis we find that a surface pattern in contact with a hard sphere liquid at densities well below bulk freezing induces a structure factor which mainly corresponds with the bulk fluid structure factor but superimposed onto it we find crystal peaks corresponding to the usual Bragg peaks of a crystal. However, this structure stems from an inhomogeneous fluid induced by the surface pattern. Depending on the strength of the surface interaction and on the fluctuations of the

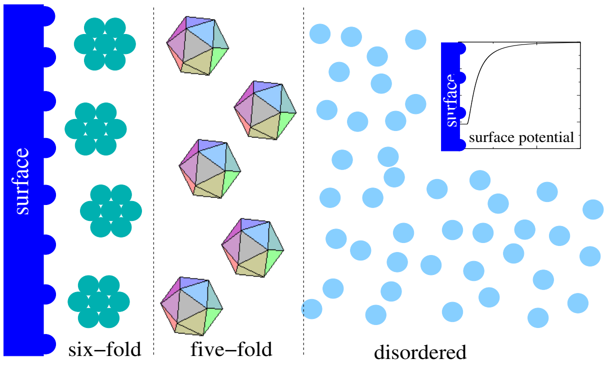

Figure 6.12: Schematic drawing of a dense hard sphere fluid in contact with an strongly attractive surface. Close to the surface the structure of the surface is imprinted into the fluid yielding a six-fold or four-fold symmetry depending on the pattern. Further away from the surface the high density fluid exhibits five-fold symmetry which decays when approaching bulk fluid densities even further away from the surface. The inset shows the attractive surface potential Eqn. (6.13).

surface particles around their ideal lattice positions the crystal peaks in the structure factor can be more or less pronounced. Clearly, a weak surface potential or highly fluctuating surface particles smear out any crystal peaks and yield a structure factor which converges toward the bulk fluid structure factor. However, by changing the penetration depth ζ to very small values this effect can be compensated and details of the surface structure can be resolved. A high penetration depth ζ on the other hand gives only a superposition with the bulk structure factor where all effects of the surface pattern are lost.

In the scope of the hard sphere model incommensurate substrates do not generally alter the structure factor. Again crystal peaks superimposed onto the bulk structure factor are found but they are shifted in position and their intensity is lowered compared to the commensurate case. However, these peaks correspond directly in position to ideal crystal lattice peaks.

Moreover from Eqn. (6.10) it follows that the surface structure cannot have any influence on the structure factor for large $k_{||}$. Therefore a commensurate and an incommensurate surface have the same limiting $S(k_{||})$ for $k_{||} \to \infty$. Proper normalization using Eqn. (6.12) takes this into account and guarantees a value of $S(k_{||} \to \infty) = 1$.

As previous studies [155] indicate that five-fold symmetry of a hard sphere liquid can be seen if the density reaches about $\eta \geq 0.60$ we furthermore investigated the effects of a high density liquid near the interface. We can increase the local density of the hard sphere fluid by applying an attractive potential perpendicular to the surface. However, as the necessary density is much higher then the bulk freezing density of $\eta = 0.545$ we need the interface to prevent the adjacent fluid from freezing. This can be done by offering a substrate pattern which is extremely unfavorable for the crystal as we demonstrated in chapter 5. Evaluating suitable order parameters, which can detect local rotational symmetry, we find that contrary to the intuitive belief, the surface structure is only weekly projected into the fluid. Only very close to the surface does the fluid exhibit the offered symmetry of the surface. After the first layers of inhomogeneous fluid, the system forms a high density glass like state which shows moderate five-fold symmetry. Farther away from the surface the decreasing potential leads to reduced density of the fluid which in turn results in a loss of the five-fold symmetry when a critical density of about $\eta = 0.60$ is reached. Overall we are able to see a five-fold symmetry in a hard sphere liquid at an interface. The effect of the interface is twofold: First, the attractive potential serves to increase the local density and second the topological structure of the pattern prevents the high density fluid from freezing.

Chapter 7

Summary

Over the past several years research on hard sphere systems has uncovered numerous surprising features with just one example, the entropical driven fluid-solid phase transition. However, there has been little research concerning hard sphere systems at interfaces and many problems and subtle effects concerning interfaces are still unsolved. Research in this direction is necessary and the hard sphere system is a good example as many basic properties of real physical systems can often be understood by assuming the interaction potential contains a hard core part. Moreover, colloidal suspensions can be prepared in such a manner that they interact in an extremely good approximation with a pure hard sphere potential. These systems can then serve as a prototype for analytical theories. Besides the theoretical understanding of interfaces, surface effects play an important role in many physical and biological phenomena and the development of new materials. This makes their study a state of the art topic.

We used *Monte-Carlo* computer simulations, analytic cell theory, as well as a phenomenological elasticity theory to investigate hard sphere systems at interfaces. Overall, we were able to find a very good correlation between the theoretical descriptions and the computer simulations. The advantage of this procedure is twofold: First, the development of a theory which is easy to use and can be very generally applied helps to understand the basic properties of a system and can point experiments using similar systems into the right direction. Second, our quantitatively correct computer simulation data can be compared directly with experiments of, for example, colloidal suspensions and can furthermore serve as benchmark test to other theories such as density functional theories.

The key results of our work have been: First, we were able to calculate the interfacial free energies of hard sphere fluids and solids in contact with a flat hard wall over the whole range of bulk densities for the fluid and for the solid at the (111), (110) and (100) orientations. We could determine these quantities using thermodynamic integration techniques in *Monte-Carlo* computer simulations as well as applying an analytical cell theory to surface problems. Using our results we prognose that a hard sphere system will not show surface freezing in contact with a flat hard wall in its (100) or (110) direction or any other loosely packed surface orientation. However, with closed packed surfaces such as the (111) direction, surface freezing is possible.

Second, we studied the influence of a substrate pattern on the surface and found that a substrate pattern profoundly influences the wetting scenario. We achieved our results using computer *Monte-Carlo* simulations as well as a new phenomenological theory which combines elastic energies of the crystal arising from elastic strains with thermodynamical bulk and surface energies. In all cases we found a close agreement between the theoretical predictions and the computer simulation results.

Choosing an appropriate surface pattern like a triangular pattern, which is commensurable with the (111) surface of the bulk solid at coexistence, can create complete wetting by crystal well below the bulk freezing pressure. Surprisingly, the minimum achieved freezing pressure can be even further lowered by making the pattern in an appropriate way non-commensurable. However, in this case the surface cannot be completely wetted by a crystal anymore.

Incomplete wetting is found by offering a substrate pattern which is not as favorable as the triangular one. We can distinguish two cases here. First, the substrate pattern is derived from a pattern which is commensurable with the bulk crystal at coexistence but the fluid-wall interfacial energy is too high to give complete wetting. This applies to the (100) and (110) orientation of the fcc crystal. Second, we can distort a pattern which actually exhibits complete wetting. This also leads to incomplete wetting due to the elastic strain energies. We have studied a rhombic distortion and a shrinking or enlarging of the surface pattern.

No wetting at all is found if the surface pattern is so unfavorable so that either the interfacial free energies or the elastic strain become too large. In this case a strongly inhomogeneous fluid will be found at the interface.

The above results can be used to make predictions on the behavior of fluids in contact with structured substrates which consequently allow especially tailored surfaces to be made. This would allow one to investigate surface freezing phenomena in future experiments with, for example, colloidal suspensions or can serve as guideline in the creation of unstable phases by a surface pattern which can be used to prepare "exotic" structures such as quasicrystalline sheets on a suitably patterned template.

Furthermore, our results can also serve as benchmark data for other theories as the recently developed density functional theories of hard-sphere freezing in inhomogeneous situations [96, 97, 98].

As a future outlook we remark that we did not address the more subtle question on what effect the roughness [162] of the solid-fluid interfaces and the formation of crystal defects at the interface have. This will be important if the wall pattern is very different from the bulk crystal structure. Both effects are neither encaptured by our simple theory nor by our finite-size simulations.

In chapter 6 we analysed the effects of a surface pattern onto a hard sphere fluid. We investigated the structure factor of this system as measured by evanescent wave measurements and consequently have provided benchmark data for experiments. In particular, we focused upon experimental effects on the structure factor, as thermal motion of the surface particles, varying penetration depths of the evanescent waves and the effects of commensurable and incommensurable surface patterns. The interesting results from the authors of [23] concerning an observed five-fold symmetry were investigated in more detail by creating a high density fluid near to a structured substrate pattern. By applying an attractive potential perpendicular to the wall we were able to raise the local density of the system which was prevented from freezing by choosing a topologically unfavorable wall pattern. We found that in this high density case the structure of the pattern is only weekly projected into the fluid. After the first few layers this effect decays and indeed a five-fold symmetry of the liquid can be detected for fluid densities larger than $\eta \approx 0.60$.

Abbreviations and symbols

α	relative density jump
$\tilde{\alpha}$	density ratio
β	*Boltzmann* constant $\beta = 1/k_BT$
β_m, β_r	elastic constants
γ	surface free energy
γ_0	surface free energy fit parameter
$\epsilon, \epsilon_x, \epsilon_y, \epsilon_z$	strain components
ζ	penetration depth
η	packing fraction
θ	incident angle
κ	compressibility
λ, λ_0	wavelength
Λ	*de Broglie* wavelength
μ	chemical potential
π	transition probability
ρ	number density $\rho = N/V$
$\hat{\rho}_{\vec{k}}$	Fourier transform of number density
σ	particle diameter
Σ	grand potential per area
ϕ	angle of rotation
Φ	stacking order parameter
Ψ	2D bond order parameter
Ω	grand potential

a	mean particle distance
$a_\triangle, a_\Box$	size of unit cell
acc	acceptance rate
A	(surface) area
C_{ij}	bulk elastic constants
d	distance
D	spacial dimension
E	system energy
E_k	kinetic energy
$\vec{e}_x, \vec{e}_y, \vec{e}_z$	Cartesian unit vectors
f	free energy density $f = F/V$
F	*Helmholtz* free energy
g_b, g_f	geometrical factor
h	*Planck* constant $h = 6.6260755 \cdot 10^{-34} Js$
$h_\triangle, h_\Box$	size of unit cell
$H(\vec{r}, \vec{p})$	*Hamilton* operator
I, I_0	wave intensity
k_B	*Boltzmann* constant $k_B = 1.380658 \cdot 10^{-23} J/K$
$\vec{k}$	wave vector $\vec{k} = (k_x, k_y, k_z)$
ℓ	thickness of wetting layer
ℓ_0	correlation length
L, L_x, L_y, L_z	length (in direction x, y, z)
L_n	*Lindemann* parameter
n	refraction index
N	particle number
$\mathcal{N}$	probability density
$\vec{p}$	particle momentum
P	pressure
Q	partition sum
Q_l, Q_{lm}	3D bond order parameter
$\vec{r}$	particle coordinate $\vec{r} = (x, y, z)$
s	strength of wall potential
$S(\vec{k})$	structure factor
T	temperature
$U(\vec{r})$	(particle) potential
V	volume
W_l	3D bond order parameter
$W(z)$	wall potential
x, y, z	spatial coordinates

CS	Carnahan-Starling
CT	cell theory
CTFN	cell theory with fixed neighbors
DFT	density functional theory
fcc	face centered cubic
hcp	hexagonal closed packed
MC	*Monte-Carlo* (simulation)
MD	*Molecular-Dynamics* (simulation)
NVT	*Monte-Carlo* simulation with constant N,V,T
NPT, NP_zT	*Monte-Carlo* simulation with constant N,P,T
Pb	lead
PY	Percus-Yevick
rcp	random closed packed
rcs	random closed stacking
Si	silicon
SPT	scaled-particle theory

Appendix

The calculation of more open wall structures like the (10) orientation in 2D or the (110) orientation in 3D is more complicated. The reason is that the crystal layers near the wall are so open that not only the first layer of the crystal is influenced by the wall but also at least the second layer. To find the minimum of the free energy one needs to minimize the position of both layers.

As an approximation, we do not minimize the volume of the Wigner-Seitz cells of the second layer. We include its full volume into the calculation. This will slightly overestimate the free interfacial energy of the crystal-wall interface.

a) The 2D (10) orientation

For the (10) orientation in 2D we have a free volume of

$$V_{\mathrm{wf}} = \frac{V_{\mathrm{bf}}}{2} + \left(d - \frac{1}{2}\right)\left(\frac{2\sqrt{3}a}{3} + \frac{\sqrt{2}d}{3} - 1\right) \tag{7.1}$$

which gives after minimization of the free energy the distance of the first layer as

$$d = \frac{\sqrt{3}}{2} + \frac{1}{4} - a + \frac{1}{4}\sqrt{25 - 4\sqrt{3} - 16\sqrt{3}a + 28a^2}\,. \tag{7.2}$$

For evaluating the volume change of the system induced by the wall it is necessary to include the volume occupied by the second layer Wigner-Seitz cells into the calculation. The total volume is therefore

$$V = Ng_b a^2 + A(d - \frac{a}{4}) \tag{7.3}$$

which can be combined with Eqn. (4.7) to obtain the surface tension

$$\begin{aligned} \gamma_{CT} \equiv \gamma_{CT}^{(10)} &= k_B T \frac{1}{2\sqrt{3}} \frac{\sigma}{a(a-\sigma)} \Big(2\sqrt{3} + 1 - 5a \\ &+ \sqrt{25 - 4\sqrt{3} - 16\sqrt{3}a - 16a + 28a^2}\Big) \end{aligned} \tag{7.4}$$

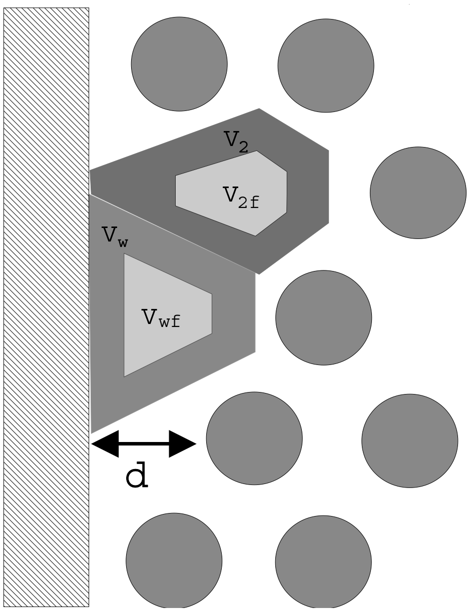

Figure 7.1: Same as in Figure (4.5) but now for (10) orientation. The distance of the first layer of particles to the wall is d. It can be seen that the effect of the second layer is not negligible.

which can be expanded around $a = \sigma$ by the leading term in $\frac{\sigma}{a(a-\sigma)}$ to fit the form of Eqn. (4.20) using a geometric factor of $g_w = \sqrt{3}$.

b) The 3D (110) orientation

In (110) orientation we get a free volume term of

$$\begin{aligned} V_{\mathrm{wf}} &= \frac{V_{\mathrm{bf}}}{2} + \sqrt{2}\left(d - \frac{1}{2}\right)(a-1)^2 - \frac{\sqrt{2}}{24}(a-1)^3 \\ &\quad + \frac{\sqrt{2}}{3}\left(\frac{a}{2} - d\right)^3 . \end{aligned} \tag{7.5}$$

The minimization of the free energy results in a wall distance of the first layer of

$$d = a(c_\alpha + \frac{1}{2}) - c_\alpha \,. \tag{7.6}$$

where $c_\alpha = \sqrt{3}\sin\alpha - \cos\alpha$ and $\alpha = \arctan(\sqrt{231}/5)/3$. The total volume is

$$V = Ng_b a^3 + A(d - \frac{a}{4}) \tag{7.7}$$

which can be combined with Eqn. (4.7) to obtain the surface tension as

$$\gamma_{CT} \equiv \gamma_{CT}^{(110)} = k_B T \frac{\sqrt{2}\sigma}{a^2(a-\sigma)} \left(\frac{a c_\alpha}{\sigma} + \frac{a}{4\sigma} - c_\alpha \right) . \tag{7.8}$$

Again this can be expanded around $a = \sigma$ by the leading term in $\frac{\sigma}{a(a-\sigma)}$ to fit the form of Eqn. (4.20) by a geometric factor of $g_w = \sqrt{2}$.

The expressions for the CTFN can be obtained by the same calculation by assuming the enlarged free volume cells or by inserting the geometric prefactors into Eqn. (4.23).

Bibliography

[1] S. Dietrich, *Phase transitions and Critical Phenomena*, volume 12, pp. 1–128, Academic Press, London, 1988.

[2] R. Evans, *Les Houches Session: Liquids at Interfaces*, volume XLVIII, p. 1ff, Elsevier, Amsterdam, 1990.

[3] M. Bernasconi and E. Tosatti, *Surf. Sci. Reports* **17**, 363 (1993).

[4] Y. Xia, D. Qin, and Y. Yin, *Curr. Op. in Colloid and Interface Science* **6**, 54 (2001).

[5] A. D. Dinsmore, J. C. Crocker, and A. G. Yodh, *Curr. Op. Colloid and Interface Science* **3**, 5 (1998).

[6] R. P. Andres, J. D. Bielefeld, J. I. Henderson, D. B. Janes, V. R. Kolagunta, C. Kubiak, W. J. Mahoney, and R. G. Osifchin, *Science* **273**, 1690 (1996).

[7] J. C. Hulteen and R. P. Duyne, *J. Vac. Sci. Technol. A* **13**, 1553 (1995).

[8] M. Winzer, M. Kleiber, N. Dix, and R. Wiesendanger, *Appl. Phys. A - Solid Surf.* **63**, 617 (1996).

[9] S. C. Kitson, W. L. Barnes, and J. R. Sambles, *Phys. Rev. Lett.* **77**, 2670 (1996).

[10] A. P. Minton, *Biophys. J.* **63**, 1090 (1992).

[11] E. Delamarche, A. Bernard, H. Schmid, B. Michel, and H. Biebuyck, *Science* **276**, 779 (1997).

[12] A. van Blaaderen, R. Ruel, and P. Wiltzius, *Nature* **385**, 321 (1997).

[13] P. Bönsch, D. Wüllner, T. Schrimpf, A. Schlachetzki, and R. Lancmann, *J. Electrochem. Soc.* **145**, 1273 (1998).

[14] D. W. L. Tolfree, *Rep. Prog. Phys.* **61**, 313 (1998).

[15] J. L. Wilbur, A. Kumar, E. Kim, and G. M. Whitesides, *Adv. Mater.* **6**, 600 (1994).

[16] H. W. Deckmann and J. H. Dunsmuir, *Appl. Phys. Lett.* **41**, 377 (1982).

[17] P. Lenz and R. Lipowsky, *Phys. Rev. Letters* **80**, 1920 (1998).

[18] C. Bauer and S. Dietrich, *Phys. Rev. E* **60**, 6919 (1999).

[19] L. J. Frink and A. G. Salingers, *J. Chem. Phys.* **110**, 5969 (1999).

[20] S. Herminghaus, A. Fery, S. Schlagowski, K. Jacobs, R. Seemann, H. Gau, W. Mönch, and T. Pompe, *J. Phys. Cond. Mat.* **12**, A57 (2000).

[21] C. Mio and D. W. M. Marr, *Langmuir* **15**, 8565 (1999).

[22] K. M. Chen, X. Jiang, L. C. Kimerling, and P. T. Hammond, *Langmuir* **16**, 7825 (2000).

[23] H. Reichert, O. Klein, H. Dosch, M. Denk, V. Honkimäki, T. Lippmann, and G. Reiter, *Nature* **408**, 839 (2000).

[24] J. C. Earnshaw and C. J. Hughes, *Phys. Rev. A* **46**, 4494 (1992).

[25] X. Z. Wu, E. B. Sirota, S. K. Sinha, B. M. Ocko, and M. Deutsch, *Phys. Rev. Lett.* **70**, 958 (1993).

[26] X. Z. Wu, E. B. Sirota, S. K. Sinha, B. M. Ocko, and M. Deutsch, *Phys. Rev. Lett.* **75**, 1332 (1995).

[27] Y. Hayami and G. Findenegg, *Langmuir* **13**, 4865 (1997).

[28] N. Maeda and V. V. Yaminsky, *Phys. Rev. Lett.* **84**, 698 (2000).

[29] O. Gang, B. M. Ocko, X. Z. Wu, E. B. Sirota, and M. Deutsch, *Phys. Rev. Lett.* **80**, 1264 (1998).

[30] O. Gang, B. M. Ocko, X. Z. Wu, E. B. Sirota, and M. Deutsch, *Phys. Rev. Lett.* **82**, 588 (1999).

[31] W. G. Hoover and F. H. Ree, *J. Chem. Phys.* **49**, 3609 (1968).

[32] B. J. Alder and T. E. Wainwright, *J. Chem. Phys.* **27**, 1208 (1957).

[33] P. G. Bolhuis, D. Frenkel, S.-C. Mau, and D. A. Huse, *Nature* **388**, 235 (1997).

[34] F. Ree and W. Hoover, *J. Chem. Phys.* **46**, 4181 (1967).

[35] W. W. Wood and J. D. Jacobson, *J. Chem. Phys.* **27**, 1207 (1957).

[36] A. Münster, *Statistical Thermodynamics*, Springer, Berlin, 1974.

[37] T. C. Hales, *arXiv:math.MG/9811078* , 1 (1998).

[38] S.-C. Mau and D. A. Huse, *Phys. Rev. E* **59**, 4396 (1999).

[39] J. Zhu, R. Rogers, W. Meyer, R. H. Ottewill, STS-73 Space Shuttle Crew, W. Z. B. Russel, and P. M. Chaikin, *Nature* **387**, 883 (1997).

[40] S. Torquato, T. M. Truskett, and P. G. Debenedetti, *Phys. Rev. Lett.* **84**, 2064 (2000).

[41] G. D. Scott and D. M. Kilgour, *Br. J. Appl. Phys.* **2**, 863 (1969).

[42] O. Pouliquen, M. Nicolas, and P. D. Weidman, *Phys. Rev. Lett.* **79**, 3640 (1997).

[43] W. S. Jodrey and M. T. E, *Phys. Rev. A* **32**, 2347 (1985).

[44] J. Tobochnik and P. M. Chapin, *J. Chem. Phys.* **88**, 5824 (1988).

[45] P. N. Pusey, *Liquids, Freezing and the Glass Transition*, North Holland, Amsterdam, 1991.

[46] A. van Blaaderen, *Progr. Colloid Polym. Sci.* **104**, 59 (1997).

[47] A. van Blaaderen and P. Wiltzius, *Adv. Mater.* **9**, 833 (1997).

[48] J. A. Barker and D. Henderson, *Rev. Mod. Phys.* **48**, 587 (1976).

[49] J. P. Hansen and I. R. McDonald, *Theory of Simple Liquids*, Academic Press, London, 2nd edition, 1986.

[50] J. Q. Broughton and G. H. Gilmer, *J. Chem. Phys.* **84**, 5095 (1986).

[51] J. Q. Broughton and G. H. Gilmer, *J. Chem. Phys.* **84**, 5105 (1986).

[52] J. Q. Broughton and G. H. Gilmer, *J. Chem. Phys.* **84**, 5119 (1986).

[53] J. Q. Broughton and G. H. Gilmer, *J. Chem. Phys.* **84**, 5741 (1986).

[54] J. Q. Broughton and G. H. Gilmer, *J. Chem. Phys.* **84**, 5749 (1986).

[55] J. Q. Broughton and G. H. Gilmer, *J. Chem. Phys.* **84**, 5759 (1986).

[56] L. Verlet, *Phys. Rev.* **159**, 98 (1967).

[57] J. L. Lebowitz, J. K. Percus, and L. Verlet, *Phys. Rev.* **153**, 250 (1967).

[58] K. Binder, E. Luijten, M. Muller, N. Wilding, and H. Blote, *Physica A* **281**, 112 (2000).

[59] D. Frenkel and B. Smit, *Understanding Molecular Simulation*, Academic, San Diego, 1996.

[60] M. P. Allen and D. J. Tildesley, *Computer Simulation of Liquids*, Clarendon Press, Oxford, 1989.

[61] M. Baus, L. F. Rull, and J. P. Ryckaert, *Observation, Prediction and Simulation of Phase Transitions in Complex Fluids*, Kluwer, Dordrecht, 1995.

[62] H. L. Anderson, *J. Stat. Phys.* **43**, 731 (1986).

[63] W. W. Wood, Molecular Dynamics Simulations of Statistical Mechanics Systems, in *Proceedings of the 97th Int* Enrico Fermi *School of Physics*, p. 2ff, Amsterdam, 1986, North Holland,.

[64] M. Lupkowski and F. van Swol, *J. Chem. Phys.* **93**, 737 (1990).

[65] N. F. Carnahan and K. E. Starling, *J. Chem. Phys.* **51**, 635 (1969).

[66] M. Dijkstra, private communication, 2000.

[67] P. Röcken and P. Tarazona, *J. Chem. Phys.* **105**, 2034 (1996).

[68] T. Kerle, J. Klein, and K. Binder, *Phys. Rev. Lett.* **77**, 1318 (1996).

[69] D. J. Diester, M. Schoen, J. E. Curry, and J. H. Cushman, *J. Chem. Phys.* **100**, 9140 (1994).

[70] M. Müller, K. Binder, and E. Albano, *Physica A* **279**, 188 (2000).

[71] A. Jaster, *Europhys. Letters* **42**, 277 (1998).

[72] H. Weber, D. Marx, and K. Binder, *Phys. Rev. B* **51**, 14636 (1995).

[73] P. J. Steinhardt, D. R. Nelson, and M. Ronchetti, *Phys. Rev. B* **28**, 784 (1983).

[74] J. S. Duijneveldt and D. Frenkel, **96**, 4655 (1992).

[75] P. R. ten Wolde, M. J. Ruiz-Montero, and D. Frenkel, *J. Chem. Phys.* **104**, 9932 (1996).

[76] P. R. ten Wolde, M. J. Ruiz-Montero, and D. Frenkel, *Phys. Rev. Lett.* **75**, 2714 (1995).

[77] L. D. Landau and F. M. Lifshitz, *Quantum Mechanics*, Pergamon, New York, 1965.

[78] F. A. Lindemann, *Z. Phys.* **14**, 609 (1910).

[79] R. Ohnesorge, H. Löwen, and H. Wagner, *Europhys. Letters* **22**, 245 (1993).

[80] P. G. de Gennes, *Rev. Mod. Phys.* **57**, 827 (1985).

[81] H. Löwen, *Phys. Rep.* **237**, 249 (1994).

[82] J. R. Henderson and F. van Swol, *Mol. Phys.* **51**, 991 (1984).

[83] R. Ohnesorge, H. Löwen, and H. Wagner, *Phys. Rev. E* **50**, 4801 (1994).

[84] B. Götzelmann, A. Haase, and S. Dietrich, *Phys. Rev. E* **53**, 3456 (1996).

[85] H. Reiss, H. L. Frisch, E. Helfand, and J. L. Lebowitz, *J. Chem. Phys.* **32**, 119 (1960).

[86] M. P. D. Henderson, *Proc. Roy. Soc. A* **410**, 409 (1987).

[87] J. Miyazaki and J. A. Barker, *J. Chem. Phys.* **64**, 3364 (1976).

[88] P. Attard and G. A. Moule, *Mol. Phys.* **78**, 943 (1993).

[89] D. J. Courtemanche and F. van Swol, *Phys. Rev. Letters* **69**, 2078 (1992).

[90] J. G. Kirkwood, *J. Chem. Phys.* **18**, 380 (1950).

[91] J. G. Kirkwood and F. P. Buff, *J. Chem. Phys.* **17**, 3382 (1949).

[92] W. Wood, *J. Chem. Phys.* **20**, 1334 (1952).

[93] K. J. Runge and G. V. Chester, *Phys. Rev. A* **36**, 4852 (1987).

[94] M. Schmidt and H. Löwen, *Phys. Rev. Letters* **76**, 4552 (1996).

[95] A. C. Mitus, H. Weber, and D. Marx, *Phys. Rev. E* **55**, 6855 (1997).

[96] Y. Rosenfeld, *Mol. Phys.* **94**, 929 (1998).

[97] Y. Rosenfeld, M. Schmidt, H. Löwen, and P. Tarazona, *J. Phys. Cond. Mat.* **8**, L577 (1996).

[98] Y. Rosenfeld, *Phys. Rev. E* **55**, 4245 (1997).

[99] W. E. McMullen and D. W. Oxtoby, *J. Chem. Phys.* **88**, 1967 (1988).

[100] R. L. Davidchack and B. B. Laird, *Phys. Rev. Lett.* **85**, 4751 (2000).

[101] A. Jaster, *Phys. Rev. E* **59**, 2594 (1999).

[102] J. W. M. Frenken and P. Stoltze, *Phys. Rev. Letters* **82**, 3500 (1999).

[103] M. R. Maaroufi, A. Stipp, and T. Palberg, *Progr. Coll. Pol. Sci.* **11**, 83 (1998).

[104] S. Pronk and D. Frenkel, *J. Chem. Phys.* **110**, 4589 (1999).

[105] M. Schmidt and H. Löwen, *Phys. Rev. E* **55**, 7228 (1997).

[106] H. Dominguez, M. P. Allen, and R. Evans, *Mol. Phys.* **96**, 209 (1999).

[107] M. Schoen and S. Dietrich, *Phys. Rev. E* **56**, 499 (1997).

[108] R. Groot, N. M. Faber, and J. van der Eerden, *Mol. Phys.* **62**, 861 (1987).

[109] J. E. Hug, F. van Swol, and C. F. Zukoski, *Langmuir* **11**, 111 (1995).

[110] D. J. Courtemanche, T. A. Pasmore, and F. van Swol, *Mol. Phys.* **80**, 861 (1993).

[111] F. van Swol and J. Henderson, *Phys. Rev. A* **43**, 2932 (1991).

[112] M. Schoen, *J. Chem. Phys.* **105**, 2910 (1996).

[113] P. Smith, R. M. Lynden-Bell, J. C. Earnshaw, and W. Smith, *Mol. Phys.* **96**, 249 (1999).

[114] P. Smith, R. M. Lynden-Bell, and W. Smith, *Mol. Phys.* **98**, 255 (2000).

[115] T. Shimizu and T. Yamamoto, *J. Chem. Phys.* **113**, 3351 (2000).

[116] J. Aizenberg, P. V. Braun, and P. Wiltzius, *Phys. Rev. Lett.* **84**, 2997 (2000).

[117] T. Pfohl, D. Beaglehole, and H. Riegler, *Chem. Phys. Lett.* **260**, 82 (1996).

[118] C. Merkl, T. Pfohl, and H. Riegler, *Phys. Rev. Lett.* **79**, 4625 (1997).

[119] L. Frink and F. van Swol, *J. Chem. Phys.* **108**, 5588 (1998).

[120] D. Henderson, S. Sokolowski, and D. Wasan, *Phys. Rev. E.* **57**, 5539 (1998).

[121] R. R. Netz and D. Andelman, *Phys. Rev. E* **55**, 687 (1997).

[122] J. Galle, H. L. Vörtler, and K.-P. Schneider, *Surface. Sci.* **387**, 78 (1997).

[123] A. Esztermann, Tripelpunktbenetzung, Diploma thesis, University of Düsseldorf, Düsseldorf, 2000.

[124] A. Weinstein and S. A. Safran, *Europhys. Lett.* **42**, 61 (1998).

[125] J. L. Barrat and H. Xu, *J. Phys. Cond. Mat.* **2**, 9445 (1990).

[126] K. Lin, J. C. Crocker, V. Prasad, A. Schofield, D. A. Weitz, T. C. Lubensky, and A. G. Yodhs, *Phys. Rev. Lett.* **85**, 1770 (2000).

[127] A. Kumar and G. M. Whitesides, *Appl. Phys. Lett.* **63**, 2002 (1993).

[128] A. K. Arora and R. Rajagopalan, *Current Op. Colloid Interf. Science* **2**, 391 (1997).

[129] F. Burmeister, C. Schäfle, T. Matthes, M. Bohmisch, J. Boneberg, and P. Leiderer, *Langmuir* **13**, 2983 (1997).

[130] A. van Blaaderen, private communication, 2000.

[131] D. A. Huse, *Phys. Rev. B* **29**, 6985 (1984).

[132] F. T. Gittes and M. Schick, *Phys. Rev. B* **30**, 209 (1984).

[133] L. D. Landau and F. M. Lifshitz, *Elastizitätstheorie*, Akademie-Verlag, Berlin, 1970.

[134] D. Frenkel and A. J. C. Ladd, *Phys. Rev. Lett.* **59**, 1169 (1987).

[135] R. L. Davidchack and B. B. Laird, *J Chem. Phys.* **108**, 9452 (1998).

[136] P. C. Ball and R. Evans, *J. Chem. Phys.* **89**, 4412 (1988).

[137] J. R. Henderson, *Phys. Rev. E* **50**, 4836 (1994).

[138] M. Dijkstra and R. Evans, private communication, 2000.

[139] M. Heni and H. Löwen, *Phys. Rev. Lett.* **85**, 3668 (2000).

[140] M. Heni and H. Löwen, *Phys. Rev. E* **60**, 7057 (1999).

[141] T. Biben, R. Ohnesorge, and H. Löwen, *Europhys. Letters* **28**, 665 (1994).

[142] S. N. Coppersmith, D. S. Fisher, B. I. Halparin, P. A. Lee, and W. F. Brinkman, *Phys. Rev. B* **25**, 349 (1982).

[143] H. Löwen and T. Beier, *Phys. Rev. B* **41**, 4435 (1990).

[144] H. Löwen, *Phys. Rev. Lett.* **64**, 2104 (1990).

[145] W. J. Huisman, J. F. Peters, M. J. Zwanenburg, S. A. de Vries, T. E. Derry, D. Abernathy, and J. F. van der Veen, *Nature* **390**, 379 (1997).

[146] D. R. Nelson and F. Spaepen, *Solid State Phys.* **42**, 1 (1989).

[147] F. Yonezawa, *Solid State Phys.* **45**, 179 (1991).

[148] F. Yonezawa and S. Sakamoto, *J. Non-Cryst. Solids* **95**, 83 (1987).

[149] H. Dosch, Critical phenomenon at surfaces and interfaces, in *Springer tracts in modern physics*, volume 126, Springer, Berlin, 1992.

[150] H. Matsuoka, H. Morikawa, S. Tanimoto, A. Kubota, Y. Naito, and H. Yamaoka, *Coll. Pol. Sci.* **276**, 349 (1998).

[151] S. Dietrich and A. Haase, *Phys. Reports* **260**, 1 (1995).

[152] D. M. North, J. E. Enderby, and P. A. Egelstaff, *J. Phys. C* **1**, 1075 (1968).

[153] J. R. Hook and H. E. Hall, *Solid State Physics*, Wiley, New York, 2nd edition, 1974.

[154] L. Bergmann and L. Schaefer, *Lehrbuch der Experimentalphysik*, de Gruyter, Berlin, 1992.

[155] A. van Blaaderen and P. Wiltzius, *Science* **270**, 1177 (1995).

[156] J. L. Finney, *Proc. Roy. Soc. Lond. A* **319**, 479 (1970).

[157] J. L. Finney, *Proc. Roy. Soc. Lond. A* **319**, 495 (1970).

[158] F. C. Frank, *Proc. Roy. Soc. Lond. A* **215**, 43 (1952).

[159] J. D. Bernal, *Nature* **185**, 68 (1960).

[160] R. Jullien, P. Jund, and D. Caprion, *Phys. Rev. E* **54**, 6035 (1996).

[161] P. J. Steinhardt, D. R. Nelson, and M. Ronchetti, *Phys. Rev. Lett.* **47**, 1297 (1981).

[162] R. Pandit and M. E. Fisher, *Phys. Rev. Lett.* **51**, 1772 (1983).

Acknowledgment

I wish to express my special thanks to Professor Dr. H. Löwen for providing me with the opportunity to perform this work as well as for his excellent support and all the scientific discussions during this time.

Especially, I thank Priv.-Doz. Dr. R. Blossey for acting as the second referee on this work and for the possibility to attend his interesting lectures.

Laura Layland I thank for correcting and improving the English of this work as well as for her support and love while writing this work.

Arben Jusufi I thank for proof reading and checking for errors and other inconsistencies in this work.

In particular I thank Matthias Schmidt, Professor Evans and Martin Watzlawek for fruitful discussions about many physical problems which arose during this work.

I also give my special thanks to the whole department of Theoretical Physics II at the University of Düsseldorf for providing a nice and stimulating environment for doing research. Within them, I especially thank Alexander Schlensog and Cord Kielhorn for their endless fights with the computer systems so that all the simulations could run smoothly

Anja Köhne I thank for her friendship which I could rely upon during the good as well as the difficult times of the past three years.

Last, but not least, I thank my parents for their continuous support.

I gratefully acknowledge the financial support from the *Deutsche Forschungsgemeinschaft* within the project *Benetzung und Strukturbildung an Grenzflächen* LO 418/5.